POLITECNICO DI MILANO

Dipartimento di Scienze e Tecnologie Aerospaziali

Corso di Laurea Magistrale in Ingegneria Aeronautica - Aerodinamica

Relatore:

Dr. Franco Auteri

Studente:

Pietro Scienza 815756

Numerical Investigation of non-Newtonian Biomagnetic Fluid Flows in presence of localised Magnetic Field

Anno Accademico: 2014-2015

CRANFIELD UNIVERSITY

School of Aerospace, Transport and Manufacturing

M.Sc. Thesis

Academic Year: 2014-2015

Pietro Scienza

Numerical Investigation of Non-Newtonian Biomagnetic Fluid Flows in presence of localised Magnetic Field

Supervisor:

Dr. László Könözsy

Except where acknowledged in the customary manner, the material presented in this thesis is, to the best of my knowledge, original and has not been submitted in whole or part for a degree in any university.

_____

Pietro Scienza

Abstract

The present work analyses the performance of the ANSYS FLUENT solver dealing with multi-physic problems where the effect of two different types of magnetic fields, one irrotational with both Lorentz and magnetization forces, and one rotational with the presence of magnetization force only, have been tested and the numerical implementation has been validated replicating and comparing the results of Tzirakis et al. [1]. Magneto and Ferro-Hydrodynamics (MHD-FHD) governing equations source terms have been passed to the FLUENT main code using User-Defined Functions (UDF) properly coded. Results obtained with the UDFs have shown a good agreement with the ones of [1]; additionally, slip boundary condition effects have been tested.

Same 3-D cylindrical tube with a 60% diameter stenosis geometry used by Tzirakis et al. [1] has been considered in order to investigate the effects of non-Newtonian Power-Law blood model and its interaction with the rotational magnetic field: remarkable differences (more than 200% for pressure and velocities magnitudes) have been found between Newtonian and non-Newtonian fluid models at same Reynolds number of 100. Moreover, it has been observed that the rotational magnetic field deflects and slows down the flow after the stenosis throat, enhancing the recirculation region and generating a stagnation point: this behaviour has turned to be interesting in biomedical terms.

A more realistic scenario has been finally analysed considering a real Aorta model reconstructed using MRI images, meshed and consequently studied through the Richardson extrapolation method from the grid convergence point of view.

The impact of non-Newtonian Power-Law model has been proven to influence the flow behaviour especially at low speeds.

The same rotational magnetic field of previous simulations, with a maximum magnitude of 4 Tesla, has been applied at three different locations consecutively and its effects on the blood flow have been investigated, finding out that the field is able to slow down and deflect the flow, changing the pattern: pressure is influenced both far downstream and upstream the magnetic force application point: medical remarks and recommendations have been provided for the magnetic field usage.

Abstract

La presente tesi si prefigge di indagare con gli strumenti della fluidodinamica computazionale, il compotamento di un fluido biologico con le stesse caratteresitiche del sangue in presenza di un campo magnetico. Le equazioni costitutive della magneto e ferroidrodinamica per un flusso omogeneo, viscoso, laminare ed incomprimibile sono quindi considerate ed in aggiunta a ciò, viene studiato il comportameto non-Newtoniano dello stesso, adottando un modello *shear-thinning Power-Law* per la viscosità. Il contenuto innovativo del lavoro svolto consiste nel simualre il flusso con le suddette caratteristiche all'interno di geometrie con un crescente livello di realisticità usufruendo del solutore CFD commerciale ANSYS-FLUENT. Questo è opportunamente adattato implementando addizionali coodici (User-Defiend Function), in modo da risolvere le equazioni della magneto e ferro-idrodinamica e in questo modo poter studiare gli effetti delle forze magnetiche. La validazione è stata condotta replicando i risultati numerici ottenuti da Tzirakis et al. per i quali soddisfacienti confronti sono stati ottenuti per tutti i casi studio considerati.

Lo stesso canale cilindrico tri-dimensionale con stenosi, presentato da Tzirakis et al. e utilizzato per validare l'implementazione numerica, viene di seguito considerato: le proprietà termodinamiche dei vasi sanguigni umani, così come del sangue stesso, insieme al comportameto non-Newtoniano di quest'ultimo, vengono introdotti per aumetare il livello di realisticità. Considerevoli differenze vengono evidenziate confrontando i risultati ottenuti per il modello Newtoniano e quello non-Newtoniano a parità di numero di Reynolds (100). Inoltre si evince che il campo magnetico rotazionale da 4 Tesla, applicato esternamente, ha l'effetto di rallentare vistosamente il flusso, deflettere il getto in uscita dalla gola della stenosi e modificandone le zone di ricircolo.

Infine si è studiato il flusso sanguigno all'interno di un segmento aortico. L'effetto del modello non-Newtoniano di viscosità risulta essere non trascurabile, in particolar modo in condizioni di basse velocità, ed inoltre, lo stesso campo magnetico rotazionale di 4 Tesla prima considerato, applicato in tre diverse posizioni lungo il vaso proncipale e attivato sequenzialmente, è risultato essere in grado di perturbare il flusso rallentandolo e deviandolo. Il campo di pressione è fortemente influenzato e le perturbazioni si estendono anche nei capillari secondari, seppur con minor intensità.

Lo studio condotto indica dunque, come sia opportuna un'analisi a diversi livelli

di realisticità e come si possano usare gli strumenti della fluidodinamica numerica per investigare complessi problemi di multi-fisica anche per applicazioni biomediche.

Sinossi

Il testo presente si articola in quattro principali sezioni. In primo luogo vengono introdotte le tematiche trattate riguardanti fluidi non-Newtoniani, magneto e ferro-idrodinamica e microfluidica, e le lacune presenti nella letteratura, attraverso uno studio comparativo di pubblicazioni precedenti. Diversi studi condotti nel recente passato sono presentati e confrontati, con particolare riguardo all'implementazione numerica e all'apporto scientifico; la revisione bibliografica si è focalizzata nel cercare lavori in cui più tematiche vengono affrontate contemporaneamente. Ciò che emerge da questa seppur non definitiva ricerca e comparazione è la pressochè completa assenza di studi in cui tutti e tre gli argomenti vengono analizzati congiuntamente attraverso la fluidodinamica numerica. Infine, sono minimi i lavori in cui vengono impiegati solutori commerciali.

Da queste carenze nella letteratura, e dalla volontà di fornire un contributo nello studio dell'emodinamica, si articola la presente tesi, che prosegue con una dissertazione matematica delle equazioni di governo e dei modelli adottati, descritti prima analiticamente e in seguito in termini numerici. L'attenzione si concentra sulle equazioni costitutive della magneto e ferro-idrodinamica, partendo dall'unione tra equazioni di Navier-Stokes, per fluidi incomprimibili, viscosi ed omogenei, ed equazioni dell'elettromagnetismo di Maxwell e mettendo in evidenza come il loro accoppiamento porti all'introduzione della forza di Lorentz (magneto-idrodinamica) e della forza di magnetizzazione (ferro-idrodinamica) nelle equazioni di conservazione della quantità di moto. I campi magnetici considerati ed implementati, vengono a questo punto introdotti, facendo riferimento alle equazioni costitutive descritte nel lavoro di Tzirakis et al. [1]: il flusso di tipo Hartmann, il campo magnetico localizzato irrotazionale generato da un filo di lunghezza infinita conduttore di corrente ed il campo magnetico rotazionale simile a quello generato dalla Terra sono dettagliati, espicitandone le componenti Cartesiane nelle direzioni dello spazio e le loro derivate prime necessarie per la discretizzazione numerica. Le equazioni costitutive non-Newtoniane della viscosità vengono specificate presentando il sopracitato modello *shear-thinning Power-Law* che andrà ad approssimare il comportamento del sangue.

Passando dunque alla parte numerica, merita una digressione l'ambiente di calcolo utilizzato, il solutore a volumi finiti ANSYS-FLUENT, ed in particolar modo gli strumenti che permettono di ampliarne le capacità: le User-Defined Functions (UDF). Queste

subroutine scritte in una particolare versione del linguaggio C che comunica con il codice sorgente di FLUENT, permettono di intervenire su più fronti attraverso specifiche macros, inserendo, ad esempio, nuove condizioni al contorno, modelli di turbolenza o termini sorgenti addizionali per le equazioni di governo. È proprio quest'ultima opzione quella scelta per l'implementazine del campo magnetico e delle forze esterne. In aggiunta, si è inserita anche la condizione a parete di slip del tipo Maxwell del prim'ordine, che però ha fornito risultati poco attendibili.

Ampio spazio viene fornito al processo di costruzione delle mesh: per tutte le geometrie in esame, canale bidimensionale, stenosi e ramo d'Aorta, è stato utilizzato il software ANSYS ICEM-CFD. Per il primo caso studio, il flusso di tipo Hartmann, si è adottata una semplice griglia di 14651 elementi quadrilateri, mentre per quanto riguarda il condotto cilindrico con stenosi, la scelta è ricaduta, dopo opportuno studio di convergenza, su una griglia costituita da 438252 elementi. La peculiarità di questa mesh, che ne ha determinato la scelta, è la crescita graduale della distanza tra gli elementi, i quali si trovano più ravvicinati a parete permettendo di catturare efficaciemente i gradienti di velocità. Lo studio di convergenza della mesh è svolto confrontandosi con i risultati ottenuti da Tzirakis et al. [1]. Infine, un approccio diverso è stato scelto nel caso dell'Aorta. Per questa geometria, ricostruita da immagini ottenute attraverso Risonanza Magnetica, viene considerato un nucleo di elementi tetraedri circondati da tre strati di elementi prismatici che crescono dalle pareti, per un numero finale di 714829 elementi totali. Anche questa scelta viene motivata da un preliminare studio di convergneza, condotto servendosi del metodo di estrapolazione di Richardson, in assenza di risultati numerici o sperimentali da comparare.

In riferimento al set-up del solutore, per tutte le simulazioni si è scelto uno schema di tipo SIMPLE per l'accoppiamento di velocità e pressione, mentre discretizzazioni spaziali ai minimi quadrati per i gradienti, second'ordine e Upwind per pressione e termini convettivi. In maniera più specifica, condizioni al contorno in ingresso e in uscita sono state personalizzate per ogni caso studio, imponendo un profilo di velocità costante per il canale bidimensionale, mentre uno completamente sviluppato per la stenosi e l'Aorta, dove per il primo si è imposto un regime di Re = 100, metre per la seconda una velocità media di 0.11 m/s.

La presentazione dei risultati e la discussione finale si articola con un impianto che prevede il susseguirsi di risultati ottenuti da simulazioni sempre più vicine ad uno scenario ideale. Uno studio preliminare, volto a verificare la coretta comunicazione tra il codice centrale del solutore e le UDF, considera il caso molto semplice del flusso Hartmann: i risultati ottenuti figurano molto accurati se confrontati con quelli per un flusso di Couette, analitici e quelli forniti da Tzirakis et al. [1]. Si procede dunque aumentando il livello di complessità, considerando il flusso di sangue, qui Newtonaino, all'interno di un

canale tridimensionale cilindrico che presenta una stenosi; in questo caso viene validata l'implementazione dei due diversi tipi di campo magnetico, irrotazionale e rotazionale. Gli effetti osservati vengono confrontati nuovamente con quelli ottenuti da Tzirakis et al. [1]: nel primo caso, irrotazionale, si ha un ottimo accordo tra i risultati per profili di velocità e pressione lungo l'asse di simmetria, sia in termini qualitativi che in termini quantitativi; nel secondo caso invece, si hanno delle discrepanze, imputate alla diversa numerica, per quanto riguarda le perturbazioni del flusso ad opera del campo magnetico, le quali risultano più accentuate rispetto a quanto osservato da Tzirakis et al. [1]. Nonostante queste lievi discrepaze, l'implementazione può essere considerata corretta, così come la fisica osservata; interessante inoltre risulta la differenza tra gli effetti dei due diversi campi magnetici: nel caso rotazionale il getto generato dalla stenosi è fortemente deflesso e vengono a crearsi importanti zone di ricircolo. In coda a queste simulazioni è stato testato anche l'effetto della condizione di scorrimento a parete; i risultati però non hanno permesso di arrivare a conclusioni certe o significative.

Pur mantenedo la stessa geometria tridimensionale provvista di stenosi e il medesimo campo magnetico rotazionale, si incrementa ora il livello di realisticità introducendo sia il modello non-Newtoniano *shear-thinning Power-Law* per il sangue, che caratteristiche termodinamiche realistiche per il condotto e per il fluido. Mantenendo lo stesso regime (Re = 100) emergono sostanziali discrepanze rispetto al suddetto caso Newtoniano: il flusso risulta decisamente più veloce ed il getto meno deflesso, il che comporta una riduzione delle zone di ricircolo ed il sorgere di un punto di ristagno a valle della stenosi dove il flusso è pressochè fermo. Questa differenza tra i due modelli di viscosità, che si traduce in uno scarto di circa il 133% in termini di valori massimi dei profili di velocità e pressione, è imputabile alla diversa formulazione del numero di Reynolds, il quale a parità di valore, fornisce una velocità all'ingresso maggiore nel caso non-Newtoniano. Da questo confronto emerge poi, come sia maggiore l'intensità degli sforzi a parete esercitati dal fluido biologico non-Newtoniano, soprattutto laddove esso viene deflesso contro le pareti stesse. Infine, si è potuto notare come la simmetria del flusso sia completamente distrutta dall'azione del campo magnetico e le perturbazioni assumano un carattere fortemente tridimensionale.

Lo scenario finale, dove viene raggiunto il più alto livello di realisticità, coinvolge un ramo aortico in cui scorre sangue modellato come fluido non-Newtoniano con lo stesso modello *shear-thinning Power-Law* precedentemente introdotto. A ciò si aggiunge l'applicazione del campo magnetico rotazionale già esaminato. Quest'ultimo viene attivato sequenzialmente in tre diverse posizioni lungo il vaso principale in modo da valutare la risposta del fluido in funzione della posizione del campo stesso. Una prima simulazione, in assenza di campo magnetico, viene svolta per confermare la validità e la correttezza del modello non-Newtoniano utilizzato: dal confronto con i risultati ottenuti per il caso

Newtoniano si evinncono apprezabili differenze in particolare quando il flusso è lento, il che avvalora la scelta operata per il modello di viscosità. Confermato dunque il comportamento non-Newtoniano, si analizza la risposta del flusso sanguigno al campo magnetico rotazionale. Il flusso sanguigno viene perturbato e rallentato e in aggiunta, da uno studio dei profili di velocità e pressione lungo in ramo principale e alle uscite dei capillari secondari, si osserva come la perturbazione si propaghi sia a monte che a valle della zona di applicazione del campo, così come lungo i vasi laterali, anche se con minore intensità. Inoltre, l' effetto del campo varia a seconda della sua posizione.

Da questo lavoro di tesi dunque, si è potuto concludere come il modello di viscosità abbia un ruolo significativo nella corretta simulazione di flussi sangugni in condizioni realistiche e come sia importante sviluppare un' analisi numerica su diversi livelli di apporssimazione della realtà. Infine, è stato possibile, anche con un solutore commercialie, studiare una fisica complessa come la magneto/ferro-idrodinamica di fluidi non-Newtoniani, fornendo risultati significativi in ambito biomedico e confermando l'utilità degli strumenti numerici anche in questo campo particolarmente delicato.

Acknowledgments

I would like to acknowledge my supervisors, Dr Franco Auteri and Dr. László Könözsy for giving me the opportunity to deal with this challenging and fascinating topic, and for sharing with me a part of the immense knowledge they have.
I also want to thank my parents for having supported me during this entire year, in any aspects of my life; and Politecnico di Milano for giving me the possibility to take part to the Erasmus program.
My gratitude goes also to the “CFD for Champions” guys I shared fun, food and knowledge along this entire year with, because “sharing is caring”, and to the “ big Italian family” : we faced every day together with the Italian smile on the face.
But most of all, I would sincerely thank my girlfriend Gioia: you gave me all the strength and love that I needed and, with your eyes, a motivation to carry on in every moment.

Pietro Scienza

Contents

List of Figures

List of Tables

Elenco dei simboli

χ Magnetic susceptibility (S/m)

δ Tangential accomodation coeffiicient

λ_M Mean free path (m)

$\mathbf{f_L}$ Lorentz force (N)

$\mathbf{f_M}$ Magnetization force (N)

μ_0 Magnetic permeability of vacuum (H/m)

ρ density (kg/m^3)

σ Electrical conductivuty (S/m)

σ_c Collisional cross-section (m^2)

$\underset{=}{\dot{\gamma}}$ Shear rate tensor $(1/s)$

$\underset{=}{\tau}$ Viscous stress tensor (Pa)

B Magnetic Field density (T)

C_p Specific Heat (J/KgK)

D Tube diameter (m)

H Magnetic Field strength (A/m)

J Current intensity (A/m^2)

k Thermal conductivity (W/mK)

k_0 Power-Law viscoisty coefficient (Pas^n)

Kn Knudsen number

L Tube length (m)

n_m number density of molecules (m^-3)

p Pressure (Pa)

u x-velocity component (m/s)

u_c Fluid velocity at cell adjacent to the wall (m/s)

u_{slip} Slip velocity (m/s)

u_w Fluid velocity at wall (m/s)

v y-velocity component (m/s)

w z-velocity component (m/s)

Chapter 1

Introduction and Objectives

1.1 Background and Motivation

The interest in multi-physical problems has been growing significantly since three decades: the steep progress in many technology and engineering fields, such as biomedical, compound and materials and precision engineering, has required a greater level of physics understanding.
For such modern applications, figuring out properly the effects of magnetic fields and the behaviour of both the Newtonian and the non-Newtonian fluids, even in narrow ducts, acquired a great importance: miniaturized applications for example, such as MEMS [5], need a high accuracy in the flow behaviour prediction and a fully understanding of the electromagnetic effects, thus, several experiments and tests started to be performed along with numerical and theoretical evaluations.
More recently, with the developement of biomedical engineering, of MRI diagnostic methods and of cancer treatments that do not need any surgical invasive practices, the understanding of the blood behaviour and its reactions to external disturbances acquired a fundamental importance, then, due to the difficulties in performing *in vivo* experiments, the numerical analysis and the CFD studies have become more and more popular as tools of prediction and analysis [6, 7, 8]. Although their reliability and accuracy is improving, the numerical fluid dynamics simulations on these multi-physics problems have still important uncertainties and often, due to limited computational resources, they suffer from strong simplifications, which entail non negligible errors.
Nevertheless, numerical simulations can have a positive impact in helping the diagnosis process and give an approximate but useful idea about the blood flow behaviour and about the treatment of possible diseases.

1.2 Problem Statement

As introduced in Section 1.1, the necessity to test, validate and evaluate the performances of CFD tools applied to biomedical problems, has a primary importance. Even though several in-house codes are available for different types of problems and aspects of this complex multi-physics problems, an investigation of the commercial software capabilities has been recognised to have a great interest.
Starting from these few key points the aims of the present thesis are:

- Investigate the novel field of Magneto- and Ferro-Hydrodynamics coupled with the non-Newtonian fluid rheology;
- Prove the ANSYS FLUENT capability to manage multi-physics problems through the UDF implementation;
- Test the CFD trustworthiness in complex problems of engineering and biomedical interest.

More precisely, the main objectives include the successful UDF implementation and its validation, and to achieve meaningful results for different geometries at increasing levels of reality.

1.3 Structure of the M.Sc. Thesis

The present thesis is organized as follow: Chapter 2 outlines and analyses the literature available about the three main topics: non-Newtonian fluid dynamics, MHD/FHD (Magneto/Ferro-Hydro-Dynamics) and microfluidic applications; analytical, experimental and numerical research state-of-the-art has been studied finding out the knowledge gaps and the possible further improvements; Chapter 3 deals with the Navier-Stokes and MHD/FHD governing equations, as well as their source terms discretization and implementation within the FLUENT UDFs. Grid generation processes and solver set-ups have been also explained in detail for all the different cases.
Results are presented and discussed in Chapter 4: the first part provides results for the UDFs validation with [1], while the second depicts results achieved for more complex cases, including a real Aorta model; all of them have been discussed and analysed in terms of physical meaning and reliability.
Finally, Chapter 5 summarises what has been found and draws the conclusions of this thesis, including recommendations for further improvements.

Chapter 2

Literature Review

Due to the complexity and multi-physical character of the present work, the literature review chapter has been divided into three sections: Section 2.1 deals with researches on non-Newtonian-fluid behaviour and rheology; Section 2.2 is focused on Magneto-hydro-dynamics (MHD) and Ferro-hydro-dynamics (FHD) works, highlighting the possible cross relations with the previous section. Finally, Section 2.3 gives an overview about the recent studies in microfluidics theory and applications with more detail devoted to both non-Newtonian fluids and MHD.

2.1 Non-Newtonian Fluids

According to the literature, the study of biofluids and biomagnetic fluids should not overlook the investigation of their viscosity model, which could significantly affects the flow physic. Common fluids, such as liquid water at normal conditions, show a linear shear stress-shear rate relation: these fluids are known as Newtonian fluids. On the other hand, when the plot of shear stress against shear rate is no longer linear, fluids are called non-Newtonian [2]. Consequently, while for Newtonian fluids a unique viscosity can be defined, considering non-Newtonian fluids, viscosity has no meaning unless it is related to a particular shear rate. Thus, the concept of apparent viscosity must be introduced:

$$\mu_a = \frac{\tau}{\dot{\gamma}}. \tag{2.1}$$

Based on the apparent viscosity, non-Newtonian fluids can be divided into two main categories: time-independent and time-dependent.

In the first category, the apparent viscosity is only related to the shear stress rate at any particular time without any dependence on how long the shear rate has been applied; it implies that time-independent non-Newtonian fluids have no memory of the shear past history. These non-Newtonian fluids are usually subdivided into three types: shear-thinning

or pseudo elastic where the apparent viscosity decreases with the shear rate increase; examples are polymer solutions, blood or detergents. The second type is the visco-plastic, such as chocolate mixture, soap or toothpaste and finally there is the shear-thickening or dilatant where the apparent viscosity increases if the shear rate increases; one common example is the wet sand.

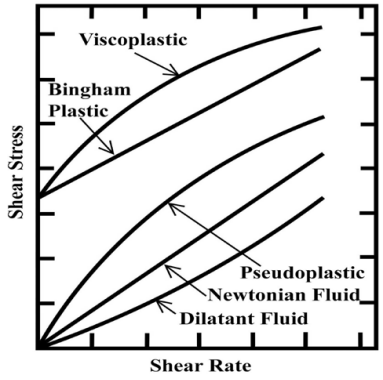

Figure 2.1: Time-independent non-Newtonian fluids: shear stress vs. shear rate [2].

Time-dependent is the second category of non-Newtonian fluids: the apparent viscosity is now dependent on how long the shear has been applied. Fluids belonging to this category can be divided into two types: thixotropic fluids and rheopectic fluids: the first, such as paints, shows a reversible decreasing behaviour of shear stress and apparent viscosity with time for a constant shear rate; the latter (bentonite clay) exhibit an inverse behaviour with an increase of shear stress and apparent viscosity along with time at constant shear rate.

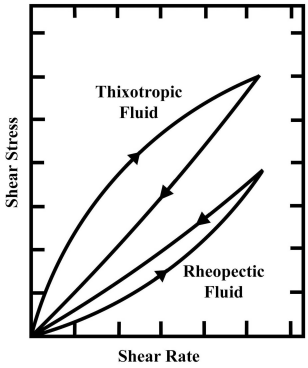

Figure 2.2: Time-dependent non-Newtonian fluids: shear stress vs. shear rate [2].

Because of the highly variable behaviour of non-Newtonian fluids, and the great number of non-Newtonian models, several researchers started to investigate, mathematically and

experimentally, at the first stage, and numerically later on, their rheological and flow properties, in order to refine the fluid approximations. Madlener et al.[9], for example, studied, mathematically and experimentally, the behaviour of the non-Newtonian gelled fluids and propellants with the Herschel-Bulkely-Extended (HBE) model, discovering a good agreement between experiments and results obtained with the HBE mathematical model, for a wide range of fluids considered. They also pointed out that the Power-Law (PL) model is not suitable for Kerosene-gel fluids while the HBE performs better. In a similar way, Fetecau [10] studied analytically a non-Newtonian fluid of Oldroyd-B type, considering an unsteady unidirectional flow with no-slip boundary conditions. Limiting cases of the Oldroyd-B model solutions have been found for Poiseulle flow and axial-annular Couette flow.
Pinho et al.[11] investigated theoretically viscoelastic fluids in pipe flows, considering a mixture of solvent and polymer additive. Except for the relevant analyses on the heat transfer in the non-Newtonian fluid dynamics, observing an asymmetric behaviour of the temperature in the pipe even if the velocity profile is completely symmetric, they proposed an interesting dissertation about different definitions of Reynolds number for PL fluids in pipe flows, which is of crucial importance if non-Newtonian fluids are considered. Therefore, those considerations regarding the Reynolds number for non-Newtonian fluids are taken into account also during the development of this thesis.

Due to the increasing importance of non-Newtonian fluids for industrial and bio-medical applications, some researchers started to investigate the fluids behaviour also numerically. Kumar et al. [12] performed a CFD study on a Power-Law fluid flow around an heated semi-circular cylinder in a 2D channel investigating the behaviour of several fluids with different power-law coefficients (n) in the laminar regimes. Differently form the majority of the studies in this field, they used the commercial software ANSYS FLUENT to perform the numerical analysis and to analyse the behaviour of the non-Newtonian fluid, observing two recirculation regions behind the semi-cylinder, an increase of drag coefficients with n for a fixed Re and an inverse dependence from n for the Nusselt number.
The study of non-Newtonian fluids must involve the blood, which is also the fluid investigated in the present thesis. As it is mentioned in the following sections, the blood viscosity has not got a unique approximation: some researchers consider it as a Newtonian fluid [13], [14], [15], [16], [17], [1], others, [18], [19], [20], [21], prefer to consider non-Newtonian models, identifying blood as a shear-thinning non-Newtonian fluid for slow flows. Ishikawa et al. [22] for example, studied numerically the blood flow through a 2D periodic and axisymmetic stenosed tube considering a bi-viscosity model for blood, that has been found to be more suitable for numerical simulation than the popular Bingham one; blood was also considered homogeneous and incompressible. First of all, a steady flow was investigated: the recirculation generated in correspondence of the sten-

osis is weakened by the plasticity of the blood, expressed through the Hedstörm number, which increases with the apparent viscosity; hence, the non-Newtonian property of blood stabilises the flow. This effect, however, is weaker for high Reynolds numbers.
Secondly, the more realistic pulsatile flow has been investigated: again, blood plasticity showed the capability to stabilise the flow reducing the recirculation strength, shifting its centre upstream and thus reducing the size: as well as for steady flow, the non-Newtonian effect becomes weak for high Re and high Strouhal numbers also. The study of blood rheology and the improvement of our capability in predicting the blood behaviour, could allow a deeper understanding of certain types of disease.

2.2 MHD/FHD

The core of the present work is to properly model and study the interaction between blood and the magnetic field, thus, a review of literature related to Magneto-hydro-dynamics (MHD) and Ferro-hydro-dynamics (FHD) is needed.
A MHD flow occurs, for instance when the Navier-Stokes governing equations are coupled with Maxwell ones and both electric conductivity and magnetization appear in the momentum and energy equations source terms, magnetic and electric fields are applied, perpendicularly to each other, across the height and width of a channel, a tube or even a micro-channel [23]; in this configuration the fluid is subject to the Lorentz force, then.
On the other hand, FHD or BFD (Biomagnetic-fluid-dynamics) flows are generated only by the influence of a magnetic field on the fluid which is not electrically conducting, thus the Lorentz force is not present and the electric field does not influence the fluid behaviour.

Several authors investigated the physics behind the MHD/FHD with particular interest in how the magnetic field can be used to control the flow, especially in biomedical applications.
First studies on magnetic effects have been related to melted metals: in 1996, Hadid et al. [24], for example, analysed the convection behaviour of a Newtonian liquid metal flow in a horizontal cavity in Birdgman configuration under the action of a constant vertical magnetic field, considering the MHD equations. Both buoyancy and thermocapillary forces have been taken into account in order to study the Hartmann layer and the Hartmann number impact on the flow. Analytical and numerical results showed a good agreement; the Hartmann number has been found to deeply influence the flow behaviour decreasing the velocity.
Verma et al. (2003) [18] investigated analytically the main features of Neuringer & Rosenswig model and Shilomis model for non-Newtonian ferrofluids subject to a magnetic field, considering the 2D Reynolds equations at low Reynolds numbers. They noted that when the magnetic field is acting, the fluid viscosity increases. Furthermore, the derived

equations have been used to solve the squeeze film bearing problem where it was found out that the viscoelastic parameters reduce the load capacity even in presence of magnetic field. Attia et al. (2006) [19] studied numerically the unsteady MHD flow of a non-Newtonian fluid of Bingham type in an infinitely long circular pipe. They considered a constant magnetic field perpendicular to the flow direction combined with the Hall current. For two-phase fluid composed of a liquid medium with variable viscosity and a constant-viscosity particle phase, an inverse relation between the magnetic field and the velocity is present, whereas, when the Hall coefficient increases, velocity, mass rate and skin friction coefficients increase as well.
Similarly, Misra et al. (2008) [20] solved the MHD equations of a visco-elastic fluid flow, approximated with the non-linear Walter's liquid B model, subject to a constant magnetic field of 8T perpendicular to the 2D stretching wall channel. They demonstrated that the reversal flow can be eliminated and the wall temperature controlled by applying a strong magnetic field; precisely, the temperature increases when the magnetic field strength increases as well.
More recently, Akbar et al. (2015) [25] evaluated numerically the behaviour of a compressible Eyring-Powell type (shear thinning) non-Newtonian fluid on a 2D stretching sheet subject to a constant magnetic field. They investigated the effects of the viscosity-model parameters γ and β and the Hartmann number, discovering that the growth of γ causes an increase in velocity and boundary layer thickness, whereas for an increase of β leads to increase only of the boundary layer while the velocity and the shear stress decrese. On the other hand, when the Hartmann number increases, both velocity and boundary layer thickness decrease, while if it decreases along with the γ parameter, the shear stress increases.

The aforementioned findings about the interaction between the magnetic field and the fluid, especially in terms of flow velocity perturbations, made biomedical investigations to strongly grow in relation to hemodynamics and blood flows. Indeed, due to its composition, blood is a biomagnetic fluid, and iron oxides in haemoglobin molecules make the blood sensitive to magnetic perturbation and induce the orientation of erythrocytes with the plane parallel to the magnetic field. Moreover, even the oxygen concentration affects the magnetic behaviour of the fluid: blood becomes diamagnetic if oxygenated and paramagnetic if de-oxygenated.
Therefore, a large number of studies, both theoretical and numerical, have been carried out to investigate the blood behaviour under the action of magnetic field, with particular interest to the flow in rectangular ducts and stenosed tubes. Tzirtzilakis et al. (2004) [13] proposed a numerical study on blood flow within a 3D rectangular duct where a 8T magnetic field generated by an infinite electrically conducing wire on the lower wall is applied. The biologic fluid was treated as biomagnetic electrically non-conducting fluid,

thus a BFD/FHD model has been considered. Magnetization has been assumed linearly dependent on the magnetic field intensity and the magnetic field saturated completely the biofluid.
As results, they discovered that the magnetic field increases and generates two recirculation regions, slowing down the flow. The strong magnetic field also affects the wall stresses, particularly near the area where it is located. Finally a secondary flow has been found to arise and strengthen due to the magnetic field intensity increase.
Similarly, Loukopoulos and Tzirtzilakis (2004) [14] analysed a laminar (Re = 250), viscous incompressible flow of a Newtonian biomagnetic fluid in a 2D channel under the action of spatially varying magnetic field, considering the FHD model with the magnetization linearly dependent on the temperature and the magnetic field intensity. Realistic blood parameters, different temperatures at walls and fully developed velocity profile at the inlet have been considered as boundary conditions. Here a recirculation region develops in proximity of the magnetic field and extends when the magnetic field intensity increases. The flow separates in proximity of the magnetic source, then reattaches downstream; the velocity recovers the fully developed profile at the outlet, while temperature perturbations are observed also in the outlet profile, and the inlet-boundary distribution is not recovered. It also increases on the lower plate where the magnetic-field source is located.
Again, Tzirtzilakis and Loukopoulos (2005) [15] carried out both an analytical and a numerical study on a blood flow within a 2D planar channel under the action of an external, locally constant magnetic field of 8 Tesla, generated from two finite disks. The Lorentz force and the electrical conductivity were also considered due to the fact that their effect prevails where the magnetic field is uniform and the magnetization is zero. The blood was assumed Newtonian with realistic properties, and constant electrical conductivity.
The most evident effect is the formation of two recirculation regions where the magnetic field begins and ends. Two other secondary eddies are generated downstream close to the second recirculation region, on both lower and upper plate and, due to this rotation, the fluid is pushed on the upper wall within the region of constant magnetic field. The flow slows down after the first recirculation region until the velocity goes back to the fully developed profile downstream, in the absence of magnetic field. Temperature increases dramatically closer to the lower plate in proximity of the magnetic field source and still increases but more slowely, downstream. Furthermore, in contrast with the velocity field, the temperature shows a perturbed profile even at the outlet. They finally observed a variable trend of the wall shear inside the the magnetized region.

A complex and remarkable numerical investigation has been conducted by Tzirakis et al. (2014) [1] who studied the effect of three different magnetic fields on the blood flow considered as Newtonian, incompressible, homogeneous, isothermal and both magnetizable

and electrically conducting in four different geometries. First, a constant magnetic field was applied to a plane Couette flow for the validation process and to the Hartmann flow; then, a variable-in-space field generated by an external wire was used again in the plane Couette; finally the two aforementioned fields and a three-component rotational one were applied to the flow through a stenosed tube. Results revealed that the irrotational magnetic field does not affect the velocity field, and the Lorentz force is negligible for very strong fields. On the other hand, the rotational field brakes the flow symmetry inducing separations and altering the total pressure. Their work has been chosen as a benchmark for the present thesis due to its in-depth analysis of magnetic effects and its investigation of blood flow behaviour in different magnetic conditions.

Numerous scientists tried to study also realistic biomedical applications from a numerical point of view, investigating the blood behaviour in presence of the magnetic field and drug particles. Numerical tools have been tested on tumour treatment and drug delivery problems. Rinaldi et al. [3] reviewed the major recent advances in ferromagnetic fluids rheology and FHD, focusing on the theoretical formulations and effects of magnetization. Biomedical applications such as drug delivery, hyperthermia and MRI (Magnetic Resonance Imaging) are analysed, as well as the magnetic susceptibility control. Magnetoviscosity was also investigated considering microfluidics applications: in a planar Couette flow with an applied magnetic field, the magnetoviscosity was found to increase the effective viscosity in DC magnetic fields, while the effective viscosity decreases, even to zero or negative values, in AC magnetic fields.

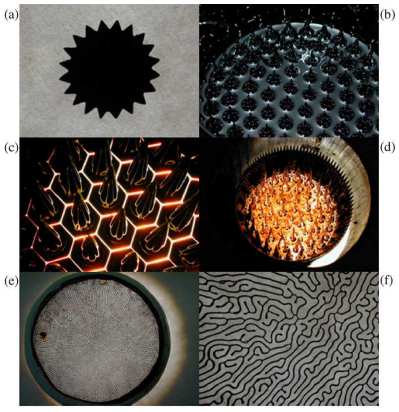

Figure 2.3: The ferrofluids instabilities in a DC magnetic field [3]

More recently, related to biomedical applications and tumour treatment, Kenjeres and Choen Stuart (2010) [4], published a work where they tried to optimize drug treatments in arteries using a magnetic field, through numerical simulations, studying the magnetic nanoparticle capturing process with a magnetic field generated by an electrically conducting wire located in four different positions.

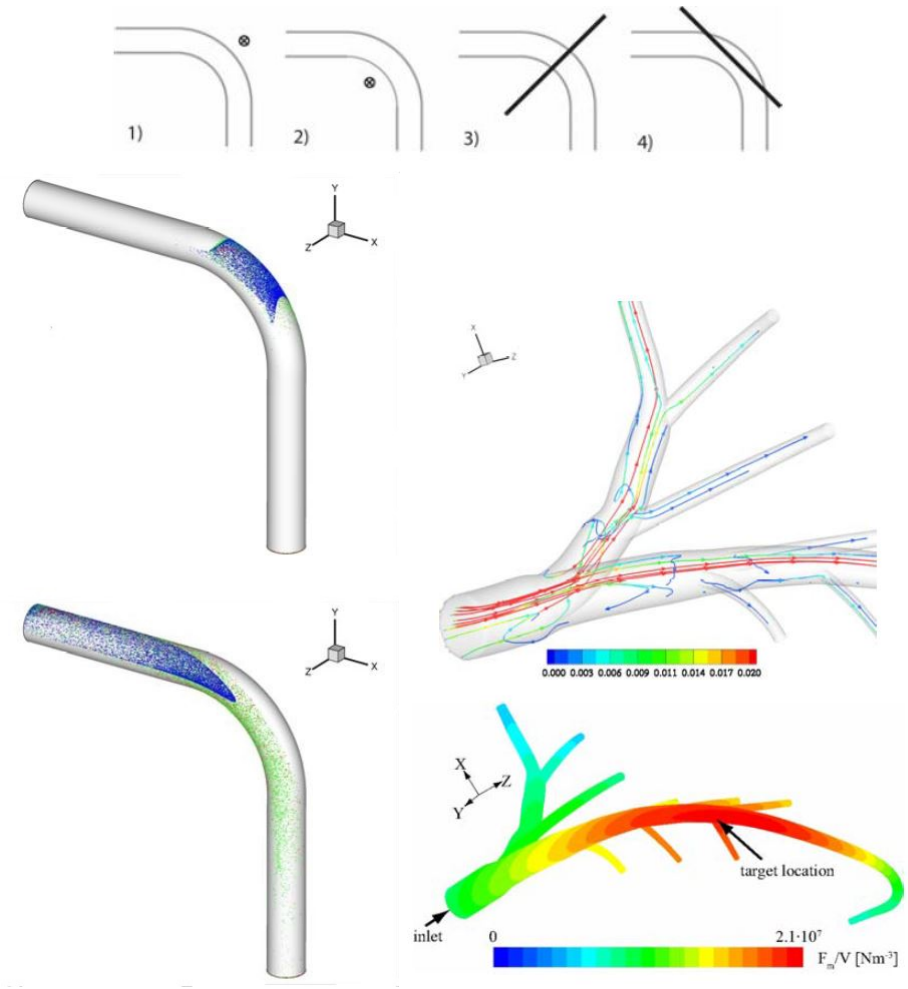

Figure 2.4: Results obtained by Kenjeres et al. [4] for the nanoparticle capturing.

Shit et al. [17] for example, modelled mathematically the laminar blood flow in a 2D axisymmetric tapered and overlapping stenosed artery subjects to an externally applied magnetic field, considering the fluid as incompressible Newtonian but porous with dilute erythrocytes approximated as spheres, suspended in plasma. Thus, the viscosity could be assumed variable and dependent on the hematocrit.. They discovered that the axial velocity significantly decreases at centre line as the magnetic field strengthens, while, on the contrary, it increases close to walls to keep the volumetric flow rate constant. Differently, the pressure gradient increases with the magnetic field. The Lorentz force has been found to slow down the flow, thus the required pressure gradient increases. They also observed that the flow in the core region is slowed down increasing the hematorcit, which has been found to have a linear relationship with blood pressure.
Again, Cherry et al. (2013) [21] proposed a numerical analysis in order to optimize the cluster concentration, size and shape of magnetic nanoparticles suspended in the blood-

stream controlled by two superposed magnetic fields, used for drug targeting. The simulation was focused on the response of the particles rather than that of the fluid for which, by the way, a non-Newtonian shear-dependent viscosity model with standard blood characteristics in a 3D straight and rounded tube was considered. The flow was assumed steady and fully developed before the particle injection, while it became unsteady. In order to obtain a short term particle trapping, low concentration, low volume and high aspect ratio of the particles cluster are required, while for long term trapping, which failed to last more than 10 seconds, high concentration, high volume and low cluster aspect ratio is needed.

2.3 Microfluidics

The study of hemodynamics and the simulations of realistic blood flow should not overlook where the biofluid actually flows. Indeed, arteries, veins and capillaries change in shape and dimensions, reaching very small diameters, for whom the continuum approximation could be not completely valid. A micro-scale analysis may be required, then.

In recent years with the great advance in precision-manufacturing techniques and the design of miniaturized devices for a wide range of applications, the interest in micro and nano-scale physics has grown steadily. Hence, the fluid behaviour in micro and nano tubes and channels rapidly acquired strong interest and it started to be studied also using Computational Fluid Dynamics tools.
Microfluidics have a large range of industrial applications: MEMS devices and Lab-On-A-Chip projects are the most advanced ones; biomedical engineers and researchers are also investigating such flows for physics understanding or for medical tools design. Moreover, they tried to couple micro-flows with non-Newtonian fluids or magnetic fields.

Considering micro-scales, the Navier-Stokes equations and the continuum approach are still valid but the no-slip boundary condition at walls is no longer valid and rarefaction effects are considered due to the molecules collisions. This regime is usually called slip flow and it is defined by the Knudsen number:

$$Kn = \frac{\lambda}{L} \tag{2.2}$$

which should be $10^{-3} < Kn < 10^{-1}$.
The majority of microfluidic applications belong to this regime and standard numerical tools are still usable adjusting the slip conditions for temperature and velocity, which are not always straightforward to be defined [26].

One of the earliest computational simulations of microfluidics related to biological MEMS devices is the one conducted by Giridharan et al. [5] in 1999 where they used the finite volume commercial solver CFD-ACE+ to solve the full Navier-Stokes equations for a power-law non-Newtonian fluid with properties similar to the blood ones, testing two power-law models. Results reveal that the typical Re number is below 100 for microchannels, then no turbulent mixing arises and the mixing process is due entirely to diffusion, which is very slow. Mandal (2005) [27] numerically analysed the unsteady blood flow within a 2D tapered vessel of finite length assuming a non-Newtonian behaviour obeying a shear-thinning power-law model, modelling the tube as elastic and thin, with slip boundary conditions at wall induced by the wall motion. They concluded that the presence of stenosis, its tapering and the steepness, affect drastically the axial velocity which develop a flat profile, differently from the non tapered and non stenosed case. Additionally, the moving walls influence the radial velocity. Ponalagusamy (2007) [28] conducted a theoretical study about the Newtonian two-layered blood flow, where a core of red cells is surrounded by a plasma peripheral layer, within a mild stenosed artery with slip velocity at walls: he observed that the slip condition is needed to properly simulate the blood flow and a dependence from peripheral layer thickness and the core viscosity have been discovered. He was finally able to obtain analytical expressions for peripheral layer thickness, core viscosity, slip velocity, shear stresses and resistance to the flow.

A novel study has been carried out by Fang et al. (2011) [29] who investigated mathematically the behaviour of a non-Newtonian fluid subject to a vertically applied, constant magnetic field on a stretching sheet with slip condition at the wall. The main finding was that from the cubic equation, only one real root resulted for every combination of magnetic field, slip velocity and mass suction parameters. They also discovered that for an increase of magnetic field, the wall slip velocity and the wall drag force also increase, while the fluid velocity decreases. Differently, the wall shear stresses increase with the magnetic field.
Another theoretical investigation has been done by Verma et al. (2011) [30]. They considered the pulsatile blood flow, modelled as the flow of Newtonian fluid, through a stenosed catheterized artery for whom the presence of the catheter made the no-slip assumption at the boundary incorrect, thus the slip velocity had to be considered. From analytical developments and experimental results, they found that axial velocity increases with time and slip velocity while it decreases with the stenosis height; the shear stress decreases with the increase of slip velocity. Finally, the effective viscosity was found to increase with the catheter radius and stenosis height, while it decreases with an increase in slip velocity.

2.4 Literature Review concluding remarks

From the above cited works, some conclusions, can be drown regarding both physical and numerical aspects. The strong interaction between fluid flows, with particular regards for biofluids, and the magnetic field clearly emerges: magnetizable fluids are always slowed down by the action of the magnetic field, which is, with few exceptions, considered constant. The rise of recirculation regions is also a stressed consequence of the perturbed and slowed down flow, which ends to an increase of the wall shear stresses. Where considered, also the non-Newtonian rheology of fluids, especially of blood, has a remarkable impact on the flow, even if perturbed by a magnetic field; however, when blood is modelled and studied, the Newtonian model is often preferred. This choice should be further discussed and clarified or questioned with comparisons between different viscosity models. Moreover, the spatial scale of the problem should be clear and not taken with carelessness: flow in capillaries and in stenosed tubes may need an analysis on micro scale, considering the slip condition, or the continuum hypothesis may require a confirmation, which is, by the way, rarely performed when biological fluids and magnetic effects are studied together. Finally, there is an inclination in consider not very realistic geometries, preferring simple channels, even bi-dimensional or straight tubes with a stenosis at most.

From a numerical point of view, most of the aforementioned authors implemented their own codes to discretise and solve the governing equations. For the MHD/FHD problems, someone adopted the vorticity-streamfunction formulation discretised with finite differences and the SOR method [22], [14], others preferred the ADI method [24], or the pseudo-transient pressure-linked equation method (PLEM) [13], again with finite difference schemes; in even other cases the Line by line implicit method (L.L.I.M) and the centred finite differences are implemented [15]. However, despite of two aforementioned works, [12, 4], nobody attempt to use a finite volume solver. In those two works, related respectively to the non-Newtonian fluid investigation and the drug treatment study in realistic biomedical scenarios, the software ANSYS FLUENT is used, achieving also low residuals and interesting results.
In conclusions, this thesis tries to fill some of those gaps in the literature and contribute constructively to it, justifying the correctness of choosing a non-Newtonian Power-Law model for blood, even when a magnetic field is present, investigating the blood flow in realistic domains and trying to obtain meaningful and reliable results, also valid for real scenarios, using the commercial CFD software ANSYS FLUENT.

Chapter 3

Governing Equations and Computational Methods

The present chapter deals with the governing equations for the Magneto and Ferro-hydrodynamics (MHD-FHD) and their numerical implementation. Section 3.1 presents and briefly explains the coupling between Navier-Stokes and Maxwell equations to finally obtain the Magneto/Ferro-Hydrodynamics (MHD/FHD) equations. Three different types of the magnetic field considered are later on proposed and non-Newtonian governing equations are also included.
Section 3.2 describes the numerical implementation of MHD/FHD terms, introducing first of all the FLUENT User-Defined-Function environment and explaining the code structure. At a later stage, a brief description of the slip boundary conditions discretization for micro-fluids is provided.
The grid generation strategies is described in Section 3.3, highlighting the meshing procedures for the three different geomentires: a simple 2-D channel, a 3-D circular duct with a stenosis and a 3-D model of a real Aorta.
Finally, Section 3.4 points out different changeovers of FLUENT solver for the simulations performed.

3.1 Magneto/Ferro-Hydrodynamics (MHD/FHD) Governing Equations

MHD governing equations are derived from the coupling between the Navier-Stokes equations and the Maxwell equations for electromagnetism.
Assuming an incompressible and homogeneous flow, the Navier-Stokes continuity and momentum equations for a Newtonian fluid are:

$$\frac{\partial \rho}{\partial t} + \rho \left(\nabla \cdot \mathbf{u}\right) = 0, \tag{3.1}$$

$$\rho \frac{\partial \mathbf{u}}{\partial t} + \rho \left(\mathbf{u} \cdot \nabla\right) \mathbf{u} = \rho \mathbf{g} - \nabla p + \mu \nabla^2 \mathbf{u} + \mathbf{f}. \tag{3.2}$$

Introducing now the Maxwell equation:

$$\frac{\partial \mathbf{B}}{\partial t} = -\nabla \times \mathbf{E}, \tag{3.3}$$

the Low-frequency Maxwell equation:

$$\nabla \times \mathbf{B} = \mu_0 \mathbf{J}, \tag{3.4}$$

and the generalized Ohm's law for moving fluids:

$$\mathbf{J}\eta = \left(\mathbf{E} + \mathbf{u} \times \mathbf{B}\right), \tag{3.5}$$

the set of MHD equations can be obtained.
In the MHD, the magnetic field acts through the Lorentz force $\mathbf{f_L}$,which appears in the momentum equation:

$$\rho \frac{\partial \mathbf{u}}{\partial t} + \rho \left(\mathbf{u} \cdot \nabla\right) \mathbf{u} = \rho \mathbf{g} - \nabla p + \mu \nabla^2 \mathbf{u} + \mathbf{f_L}. \tag{3.6}$$

$$\mathbf{f_L} = \mathbf{J} \times \mathbf{B}, \tag{3.7}$$

The Lorentz force expresses the action of the magnetic field on a moving charge; therefore, if the fluid is electrically sensitive, the magnetic field generates a Lorentz force on it.

The current intensity **J** is derived from the Ohm's law (3.5):

$$\mathbf{J} = \sigma\left(\mathbf{E}+\mathbf{u}\times\mathbf{B}\right), \tag{3.8}$$

where **B**, the magnetic flux density, satisfies the divergence-free constrain:

$$\nabla\cdot\mathbf{B} = 0, \tag{3.9}$$

in absence of the electric field, **E**, the current intensity **J** is simplified as follow:

$$\mathbf{J} = \sigma\left(\mathbf{u}\times\mathbf{B}\right), \tag{3.10}$$

and the Lorentz force becomes:

$$\mathbf{f_L} = \text{œ}\left(\mathbf{u}\times\mathbf{B}\right)\times\mathbf{B}. \tag{3.11}$$

Differently, if the fluid is directly sensitive to a magnetic field, even without the presence of an electric current, its behaviour is governed by Ferro-Hydrodynamics equations [31, 32] and it is called magnetizable: then, ferrofluids are described by the magnetic state equation, or magnetization equation $\mathbf{M} = \mathbf{M}(\mathbf{H}, T)$, which is usually dependent on temperature density and magnetic field intensity **H**, often through complex relations [1]. However, for some materials, such as fluids like blood, which are weak magnetic conductor, simplified expressions can be used without losing accuracy and reliability:

$$\mathbf{M} = \chi\mathbf{H}. \tag{3.12}$$

Equation (3.12) introduces a dependence to the (volume) magnetic susceptibility χ, which expresses the material reactivity to an externally applied magnetic field: blood has a very weak magnetic character and either paramagnetic or diamagnetic behaviour can be assumed, depending on the oxygenation. For oxygenated blood, $\chi_{ox} = -6.6\cdot10^{-7}$ denotes

a diamagnetic character, whereas in de-oxygenated case blood behaves as paramagnetic fluid with $\chi_{deox} = 3.5 \cdot 10^{-6}$.

The magnetization arises as magnetization force in the RHS of the Navier-Stokes momentum equations defining the FHD momentum equations as:

$$\rho \frac{\partial \mathbf{u}}{\partial t} + \rho \left(\mathbf{u} \cdot \nabla\right) \mathbf{u} = \rho \mathbf{g} - \nabla p + \mu \nabla^2 \mathbf{u} + \mathbf{f_M}, \tag{3.13}$$

$$\mathbf{f_M} = \mu_0 \left(\mathbf{M} \cdot \nabla\right) \mathbf{H}. \tag{3.14}$$

Finally, if the fluid is both electrically and magnetically sensitive, then, both the MHD and the FHD effects arise and the final MHD/FHD momentum equations become:

$$\rho \frac{\partial \mathbf{u}}{\partial t} + \rho \left(\mathbf{u} \cdot \nabla\right) \mathbf{u} = \rho \mathbf{g} - \nabla p + \mu \nabla^2 \mathbf{u} + \text{œ} \left(\mathbf{u} \times \mathbf{B}\right) \times \mathbf{B} + \bar{}_{\mathbf{0}} \left(\mathbf{M} \cdot \nabla\right) \mathbf{H}. \tag{3.15}$$

Furthermore, a relation between the magnetic field intensity $\mathbf{H}$ and the magnetic field density $\mathbf{B}$ can be formulated through the vacuum magnetic permeability μ_0 and the magnetic susceptibility:

$$\mathbf{H} = \frac{1}{\mu_0} \frac{1}{(1+\chi)} \mathbf{B}, \tag{3.16}$$

Thus, back to the magnetization (3.12), the correlation to the magnetic field density can be made clear through the following expression:

$$\mathbf{M} = \chi \mathbf{H} = \frac{1}{\mu_0} \frac{\chi}{1+\chi} \mathbf{B}, \tag{3.17}$$

Finally, substituting (3.17) into (3.14) and successively in (3.15), it is possible to obtain an expression for the FHD momentum source terms that is only function of **B**:

$$\rho \frac{\partial \mathbf{u}}{\partial t} + \rho \left(\mathbf{u} \cdot \nabla\right) \mathbf{u} = \rho \mathbf{g} - \nabla p + \mu \nabla^2 \mathbf{u} + \mathbf{œ} \left(\mathbf{u} \times \mathbf{B}\right) \times \mathbf{B} + \mathbf{ff} \left(\mathbf{B} \cdot \nabla\right) \mathbf{B}, \tag{3.18}$$

where:

$$\alpha = \frac{1}{\mu_0} \frac{\chi}{(1+\chi)^2}. \tag{3.19}$$

Considering a general three-dimensional Cartesian domain, the two MHD-FHD source terms, $\mathbf{f_L}$ and $\mathbf{f_M}$ can be decomposed along each direction as the other momentum equations terms.
For the Lorentz force:

$$\mathbf{J} = \sigma \left(\mathbf{u} \times \mathbf{B}\right) = \begin{vmatrix} \mathbf{i} & \mathbf{j} & \mathbf{k} \\ u & v & w \\ B_x & B_y & B_z \end{vmatrix} = J_x \mathbf{i} + J_y \mathbf{j} + J_z \mathbf{k}, \tag{3.20}$$

where:

$$J_x = \sigma \left(v B_z - w B_y\right), \tag{3.21}$$

$$J_y = \sigma \left(w B_x - u B_z\right), \tag{3.22}$$

$$J_x = \sigma\left(uB_y - vB_x\right), \tag{3.23}$$

then:

$$\mathbf{f_L} = \mathbf{J}\times\mathbf{B} = \begin{vmatrix} \mathbf{i} & \mathbf{j} & \mathbf{k} \\ J_x & J_y & J_z \\ B_x & B_y & B_z \end{vmatrix} = \left(J_yB_z - J_zB_y\right)\mathbf{i} + \left(J_zB_x - J_xB_z\right)\mathbf{j} + \left(J_xB_y - J_yB_x\right)\mathbf{k}. \tag{3.24}$$

Finally, the three components can be expressed as follows:

$$f_{Lx} = \sigma\left[-u\left(B_y^2 + B_z^2\right) + vB_xB_y + wB_xB_z\right], \tag{3.25}$$

$$f_{Ly} = \sigma\left[uB_xB_y - v\left(B_x^2 + B_z^2\right) + wB_yB_z\right], \tag{3.26}$$

$$f_{Lz} = \sigma\left[uB_xB_z + vB_yB_z - w\left(B_x^2 + B_y^2\right)\right]. \tag{3.27}$$

With a 2-D magnetic field density $\mathbf{B} = \mathbf{B}\left(x,y\right) = \left(B_x, B_y\right)$ the previous expressions can be easily simplified to:

$$f_{Lx} = \sigma\left[-uB_y^2 + vB_xB_y\right], \tag{3.28}$$

$$f_{Ly} = \sigma\left[uB_xB_y - vB_x^2\right], \tag{3.29}$$

$$f_{Lz} = \sigma\left[-w\left(B_x^2 + B_y^2\right)\right]. \tag{3.30}$$

Considering now the magnetization force, it can be noticed from (3.14) how similar to the velocity convective term its formulation is; thus the three components can be directly expanded as:

$$f_{Mx} = \alpha \left[B_x \frac{\partial B_x}{\partial x} + B_y \frac{\partial B_x}{\partial y} + B_z \frac{\partial B_x}{\partial z} \right], \tag{3.31}$$

$$f_{My} = \alpha \left[B_x \frac{\partial B_y}{\partial x} + B_y \frac{\partial B_y}{\partial y} + B_z \frac{\partial B_y}{\partial z} \right], \tag{3.32}$$

$$f_{Mz} = \alpha \left[B_x \frac{\partial B_z}{\partial x} + B_y \frac{\partial B_z}{\partial y} + B_z \frac{\partial B_z}{\partial z} \right]. \tag{3.33}$$

If the 2-D case is considered, the magnetization force components assume the following simplified form:

$$f_{Mx} = \alpha \left[B_x \frac{\partial B_x}{\partial x} + B_y \frac{\partial B_x}{\partial y} \right], \tag{3.34}$$

$$f_{My} = \alpha \left[B_x \frac{\partial B_y}{\partial x} + B_y \frac{\partial B_y}{\partial y} \right], \tag{3.35}$$

$$f_{Mz} = 0. \tag{3.36}$$

Finally the fully 3-D MHD/FHD momentum equations can be written in all the three components as follows:

$$\frac{\partial u}{\partial t}+u\frac{\partial u}{\partial x}+v\frac{\partial u}{\partial y}+w\frac{\partial u}{\partial z}= \\ -\frac{1}{\rho}\frac{\partial p}{\partial x}+\mu\left(\frac{\partial^2 u}{\partial x^2}+\frac{\partial^2 u}{\partial y^2}+\frac{\partial^2 u}{\partial z^2}\right)+\frac{1}{\rho}\left(f_{Lx}+f_{Mx}\right), \quad (3.37)$$

$$\frac{\partial v}{\partial t}+u\frac{\partial v}{\partial x}+v\frac{\partial v}{\partial y}+w\frac{\partial v}{\partial z}= \\ -\frac{1}{\rho}\frac{\partial p}{\partial y}+\mu\left(\frac{\partial^2 v}{\partial x^2}+\frac{\partial^2 v}{\partial y^2}+\frac{\partial^2 v}{\partial z^2}\right)+\frac{1}{\rho}\left(f_{Ly}+f_{My}\right), \quad (3.38)$$

$$\frac{\partial w}{\partial t}+u\frac{\partial w}{\partial x}+v\frac{\partial w}{\partial y}+w\frac{\partial w}{\partial z}= \\ -\frac{1}{\rho}\frac{\partial p}{\partial z}+\mu\left(\frac{\partial^2 w}{\partial x^2}+\frac{\partial^2 w}{\partial y^2}+\frac{\partial^2 w}{\partial z^2}\right)+\frac{1}{\rho}\left(f_{Lz}+f_{Mz}\right). \quad (3.39)$$

The three different types of magnetic fields considered in the present work, derived from [1], are now described.

3.1.1 The Hartmann Flow

The Hartmann flow, the first case considered, is basically a plane Couette flow apt to a constant magnetic field $\mathbf{B} = B_0\mathbf{j}$ normal to the plates; then, only the Lorentz force component f_{Lx}survives in the MHD momentum equations:

$$f_{Lx} = -u\sigma B_0^2. \quad (3.40)$$

Because the magnetic field is constant and parallel to the y-axis, the flow is affected along the x-direction only, which represents the main advantage of the Hartmann flow in computational terms: since it belongs to one-dimensional flows family, it is possible to derive an analytical solution (3.41) for the velocity profile, and easily check the numerical implementation and the solver set-up [1].

$$u(y) = \frac{1}{\sigma B_0^2}\left(\frac{dp}{dx}\right)\left[1 - \frac{\cosh\left(\frac{Hy}{h}\right)}{\cosh(H)}\right], \tag{3.41}$$

where:

$$H \equiv hB_0\sqrt{\frac{\sigma}{\mu}}.$$

is the Hartmann number.

3.1.2 The Irrotational Magnetic Field

An irrotational magnetic field, described by the Equation (3.42), is the second case studied.

$$\mathbf{B} = \mathbf{B}(x,y) = K\left(\frac{y-y_i}{(x-x_i)^2+(y-y_i)^2}\right)\mathbf{i} - K\left(\frac{x-x_i}{(x-x_i)^2+(y-y_i)^2}\right)\mathbf{j}, \tag{3.42}$$

The Cartesian components are:

$$B_x = K\left(\frac{y-y_i}{(x-x_i)^2+(y-y_i)^2}\right), \tag{3.43}$$

$$B_y = K\left(\frac{x-x_i}{(x-x_i)^2+(y-y_i)^2}\right), \tag{3.44}$$

Then, spatial derivatives become:

$$\frac{\partial B_x}{\partial x} = -2K\left(\frac{(x-x_i)(y-y_i)}{\left((x-x_i)^2+(y-y_i)^2\right)^2}\right), \tag{3.45}$$

$$\frac{\partial B_x}{\partial y} = \frac{K}{(x-x_i)^2+(y-y_i)^2} - 2K\left(\frac{(x-x_i)(y-y_i)}{\left((x-x_i)^2+(y-y_i)^2\right)^2}\right), \tag{3.46}$$

$$\frac{\partial B_y}{\partial x} = -\frac{K}{(x-x_i)^2+(y-y_i)^2} + 2K\left(\frac{(x-x_i)^2}{\left((x-x_i)^2+(y-y_i)^2\right)^2}\right), \tag{3.47}$$

$$\frac{\partial B_y}{\partial y} = 2K\left(\frac{(x-x_i)(y-y_i)}{\left((x-x_i)^2+(y-y_i)^2\right)^2}\right). \tag{3.48}$$

This field is generated by an electrically conducting straight and infinite wire; x_i and y_i are the wire location coordinates while the parameter $K = \mu_0 I/2\pi$, depending on the electric current I, defines point-wisely the field intensity.
For this case both magnetization and Lorentz forces are present, therefore, the fully MHD-FHD model is considered.

3.1.3 The Rotational Magnetic Field

The rotational magnetic field is the third and final case considered. Its formulation represents the field generated by an ideal dipole, similar to the magnetic field produced by the Earth, which also satisfies the Gauss's law:

$$\mathbf{B} = \mathbf{B}(x,y,z) = -C\left(\frac{2(x-x_i)^2 - r^2}{r^6}\right)\mathbf{i} - C\left(\frac{2(x-x_i)(y-y_i)}{r^6}\right)\mathbf{j} - C\left(\frac{2(x-x_i)(z-z_i)}{r^6}\right)\mathbf{k}, \quad (3.49)$$

Its components are:

$$B_x = -C\left(\frac{2(x-x_i)^2 - r^2}{r^6}\right), \quad (3.50)$$

$$B_y = -C\left(\frac{2(x-x_i)(y-y_i)}{r^6}\right), \quad (3.51)$$

$$B_z = -C\left(\frac{2(x-x_i)(z-z_i)}{r^6}\right), \quad (3.52)$$

The spatial derivatives can be defined as follow:

$$\frac{\partial B_x}{\partial x} = 6C\frac{(x-x_i)\left((x-x_i)^2 - (y-y_i)^2 - (z-z_i)^2\right)}{r^8} - 2C\frac{(x-x_i)}{r^6}, \quad (3.53)$$

$$\frac{\partial B_y}{\partial x} = 12C\frac{(x-x_i)^2(y-y_i)}{r^8} - 2C\frac{(x-x_i)}{r^6}, \quad (3.54)$$

$$\frac{\partial B_z}{\partial x} = 12C\frac{(x-x_i)^2(z-z_i)}{r^8} - 2C\frac{(x-x_i)}{r^6}, \quad (3.55)$$

$$\frac{\partial B_x}{\partial y} = 6C\frac{(y-y_i)\left((x-x_i)^2-(y-y_i)^2-(z-z_i)^2\right)}{r^8} - 2C\frac{(y-y_i)}{r^6}, \tag{3.56}$$

$$\frac{\partial B_y}{\partial y} = 12C\frac{(x-x_i)(y-y_i)^2}{r^8} - 2C\frac{(x-x_i)}{r^6}, \tag{3.57}$$

$$\frac{\partial B_z}{\partial y} = 12C\frac{(x-x_i)(y-y_i)(z-z_i)}{r^8}, \tag{3.58}$$

$$\frac{\partial B_x}{\partial z} = 6C\frac{(z-z_i)\left((x-x_i)^2-(y-y_i)^2-(z-z_i)^2\right)}{r^8} - 2C\frac{(z-z_i)}{r^6}, \tag{3.59}$$

$$\frac{\partial B_y}{\partial z} = 12C\frac{(x-x_i)(y-y_i)(z-z_i)}{r^8}, \tag{3.60}$$

$$\frac{\partial B_z}{\partial z} = 12C\frac{(x-x_i)(z-z_i)^2}{r^8} - 2C\frac{(x-x_i)}{r^6}. \tag{3.61}$$

where $r = \sqrt{(x-x_i)^2+(y-y_i)^2+(z-z_i)^2}$ is the dipole radius. The magnetic field magnitude is determined by the constant C and the coordinates x_i, y_i and z_i where the magnetic field is located.
This magnetic field is supposed to influence the flow in a rotational way, which can have a remarkable impact on the fluid behaviour and can provide interesting results even in biological terms. Only the magnetization force is acting, thus the flow obeys to the FHD model.

3.1.4 The non-Newtonian Constitutive Model for Blood

As described in [22, 12, 33], blood shows a non-Newtonian shear-thinning behaviour, particularly when the flow is characterized by low Reynolds numbers and the viscous

terms become dominant, therefore the non-linear relation between the shear strain rate and the shear stress has to be taken into account in order to properly model the fluid.
Several non-Newtonian constitutive models have been derived in order to characterize the blood bio-rheology: Power-Law [34], Quemada [35] and Casson [36] are the most popular and the ones that fit more the blood viscous behaviour. Other models, such as viscoelastic Oldroyd-B model [10], have been tested, but with less accurate results for blood.
For the non-Newtonian fluids in general, the dynamic viscosity coefficient is a function of the shear rate $\underset{=}{\dot{\gamma}}$, which represents the main difference from Newtonian fluids:

$$\mu = \mu\left(\left|\underset{=}{\dot{\gamma}}\right|\right), \tag{3.62}$$

thus, the interdependence between the shear rate tensor and the viscous stress is modified as follows:

$$\underset{=}{\tau} = \mu\left(\left|\underset{=}{\dot{\gamma}}\right|\right)\left|\underset{=}{\dot{\gamma}}\right|, \tag{3.63}$$

where:

$$\underset{=}{\dot{\gamma}} = 2\underset{=}{S} = \mathbf{u}\otimes\nabla + \nabla\otimes\mathbf{u}, \tag{3.64}$$

$$\left|\underset{=}{\dot{\gamma}}\right| = \sqrt{2tr\left(\underset{=}{S}^2\right)}. \tag{3.65}$$

Form Equation 3.63 it can be easily deduced that the viscous terms of the Navier-Stokes momentum equations are largely modified due to the non-constancy of the viscosity (see Chapter A for more detailed mathematical treatment of Navier-Stokes equations viscous terms).
Between the aforementioned fluid models, the Power Law Model has been chosen due to its simplicity and suitability in describing slow shear-thinning fluids [12], such as blood,

without increasing excessively the computational cost but still achieving a good blood behaviour approximation. As the name suggests, the shear stress is a function of a n-power of the shear strain rate:

$$\tau = k_0 \dot{\gamma}^n, \tag{3.66}$$

then, the viscous stress tensor becomes:

$$\underline{\underline{\tau}} = k_0 \left| \underline{\underline{\dot{\gamma}}} \right|^{n-1} \left| \underline{\underline{\dot{\gamma}}} \right|, \tag{3.67}$$

where the parameters $k_0 = 14.67 \cdot 10^{-7} Pa \cdot s^n$ and $n = 0.7755$ are peculiar for blood.
According to the viscous model, a new Reynolds number should be defined and must be taken into account during the simulation set-up as discussed in 2:

$$Re_{P-L} = \frac{\rho h^n}{k_0 U_\infty^{n-2}}. \tag{3.68}$$

3.2 The Numerics

The present section briefly discusses the numerical implementation of the two magnetic forces that act on the fluid. Due to the usage of the commercial solver ANSYS FLUENT, to include a User-Defined Function is the only way to modify the governing equations; thus, an overview on how the UDFs work is provided.
The Lorentz and the magnetization forces can be treated as source terms in the Navier-Stokes momentum equations, which allows to model the magnetic field action by simply adding two additional terms and without solving any other equation: this approximation turned to be sufficiently accurate and reliable in terms of fluid flow physics.

3.2.1 The ANSYS FLUENT UDFs Environment

The User-Defined Functions (UDFs) are C language subroutines, or even long C codes, that enhance the capabilities of the FLUENT built-in standard solver.

Through loading the UDF within the solver environment, a large amount of features can be modified and tuned: boundary conditions, additional source terms, customized models (e.g. multiphase) or scalar transport equations can be added and modified.
As previously touched on, the UDFs are programmed in a C language slightly modified version, according to the ANSYS FLUENT requirements. Precisely, the communications of new features between the UDF and the main solver code occur through specific macros called DEFINE macros, that allow to access additional solver data and to establish a clear link with the built-in solver structure Figure 3.1 on page 28. One source code could include several UDFs, that can also communicate with each other.

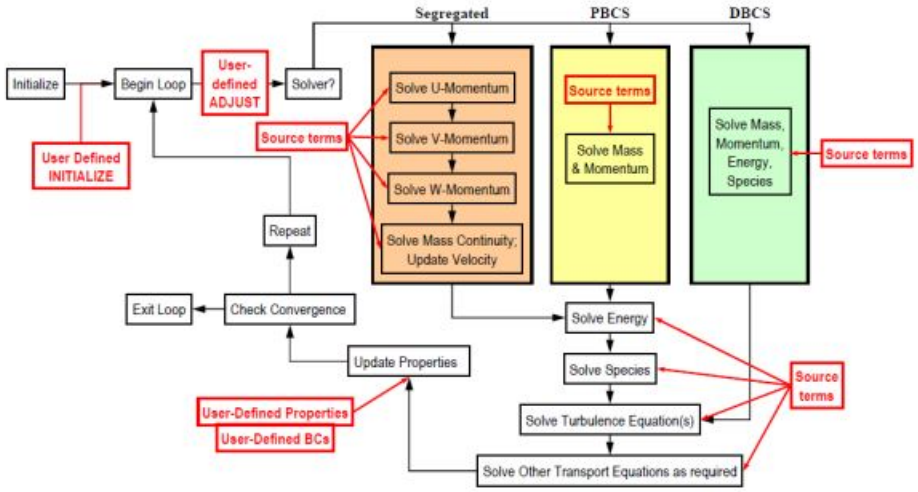

Figure 3.1: The UDF-main-solver interactions.

All the DEFINE macros should have the following declaration:

```
DEFINE_MACRONAME(udf_name, passed-in variables)
```

`udf_name` is the function identifier and can be visible through the FLUENT user interface, whereas `passed-in variables` are all the inputs needed by the UDF to compute the operations: each variable has a precise identifier within the FLUENT environment and must be recalled through it. With the exception of the DEFINE macros and the specific variables, the source code structure obeys to the standard C programming rules, including the library calling procedures, the variables declarations and the looping frameworks.

In some cases it might be needed to store some variables for a later usage or to allow another UDF to use them without a re-definition; it is possible, then, to create and store these new variables through the User-Defined Memory (UDM) macros, which allow to assign a memory location to these variables (`F_UDMI` to store face variable or `C_UDMI` to store cell variables) and make them accessible by FLUENT.
Finally, the UDFs implemented for the present work are:

- The User-Defined INITIALIZE: allows to include the magnetic field within the solver and to initialize it as the other variables;
- The User-Defined SOURCE TERMS for the momentum equations, which include the effect of magnetization and Lorentz forces;
- The User-Defined PROFILE for the wall slip boundary condition.

Four source scripts have been coded totally: one for the Hartmann flow, a second for the irrotational magnetic field, a third for the rotational one and the last one where the rotational magnetic field has been applied to the Aorta.
For a more detailed and exhaustive explanation and description of the UDF structure and macros types, one should refer to the ANSYS-FLUENT UDF manual [37].

3.2.2 The MHD/FHD Terms Implementation

As it has been introduced in Section 3.1, the fluid sensitivity to the magnetic field arises through the presence of the magnetization and the Lorentz forces, which are treated as source terms in the momentum equations.
The flow field variables initialization is the first step for all the CFD simulations, thus, due to its presence, even the magnetic field should be initialized. Each component of the field is stored within a User-Defined Memory and the initialization process, using the macro `DEFINE_INIT(udf_name, domain)`, involves all the cells in the domain, through a loop. The new variables are stored at the cells centre.

Because of the relative simplicity and linearity of the equations (3.42) and (3.49), a proper discretization has not been required, even because the global variable `xc[ND_ND]` provides the spatial coordinates in all the three directions for the FLUENT environment:

```
x = xc[0]

y = xc[1]

z = xc[2]
```

thus, the magnetic field terms implementation turned out to be straight forward.
Once the magnetic field and its components, either 2-D irrotational or 3-D rotational, have been defined and stored, the next step is to define the actual source terms for the momentum equations: `DEFINE_SOURCE(udf_name, c, t, dS, eqn)` is the macro used to declare the source terms; equations (3.25) to (3.36) are implemented within this macro. Should be point out that each momentum equation is split into the three spatial directions thus, three `DEFINE_SOURCE` UDFs are required. The `c,t,dS` and `eqn` variables are passed to the UDF by the solver and define the cell identifier index, the pointer (cell thread), the source term derivative with respect to the transport equation dependent variable and the equation number, respectively.
The magnetic field components are recalled through the previously mentioned UDMs within the initialization part, however, the definition of the source terms does not need a loop over the cells which is already performed by FLUENT. "Generation rate/volume" must be the form of all the source terms unit; thus, considering the case of momentum equations, the source terms unit ought to be N/m^3.

3.2.3 The Slip Boundary Condition Implementation

According to what has been explained in Section 2.3, the presence of micro-scale domains requires to investigate the impact of a possible non-slip hypothesis break-down.
In order to evaluate the possible differences between slip and non-slip boundary conditions, the UDFs allow to impose a slip velocity profile at wall boundaries through the macro `DEFINE_PROFILE(udf_name, t, position)`.
In the present thesis the Maxwell 1^{st} order approximation for the wall slip velocity has been considered:

$$u_{slip} = u_s - u_w = \frac{2-\delta}{\delta}\lambda_M \left.\frac{\partial u_s}{\partial n}\right|_w, \tag{3.69}$$

where λ_M is the particle mean free path, and δ is the tangential accommodation coefficient, which has been set to 1.
The discretization of the equation (3.69) has been carried out through an implicit Upwind scheme:

$$u^i_{slip} = \frac{2-\delta}{\delta}\lambda_M \left.\frac{\partial u^i_s}{\partial n}\right|_w, \tag{3.70}$$

$$\frac{\partial u_s^i}{\partial n} = \frac{-u_{slip}^i + u_c^i}{\triangle y/2}, \tag{3.71}$$

where u_c^i is the velocity of the wall face adjacent to the cell.
Gathering together all the coefficients in $\beta = \frac{2-\delta}{\delta}\frac{\lambda_M}{\triangle y/2}$, the final expression of the discretized slip velocity becomes:

$$u_{slip}^i = \frac{\beta}{\beta+1} u_c^i. \tag{3.72}$$

The choice of an implicit formulation has been justified by the lower complexity if compared to the explicit one, caused by the absence of previous iteration values, that are not easy to recover within the UDF. Additionally, the explicit formulation revealed to be unstable without an appropriate under-relaxation factor. Due to the complexity of the blood composition, the water number density of molecules and the collisional cross-section values have been considered, and through their values, $n_m = 33.4 \cdot 10^{27}\, m^{-3}$ and $\sigma_c = 10^{-19}\, m^2$ respectively, the mean free path is defined: $\lambda_M = 1/n_m\sigma_c$. Even though this approximation does not take into account the real blood parameters, it has been considered to be accurate enough for a first order solution.

3.3 The Grid Generation

The grid generation procedures that have been followed to obtain the different meshes, are described in the sections below.
Three different geometries have been considered: a simple two dimensional channel for the Hartmann Flow, a three dimensional cylindrical duct with a stenosis and finally, a three dimensional Aorta segment based on real dimensions and proportions; for each, several meshes have been generated using the ANSYS ICEM-CFD meshing tool.

3.3.1 The 2-D Channel for the Hartmann Flow

The 2-D channel model used to study the Hartmann Flow has been based on the Tzirakis et al. one [1]:

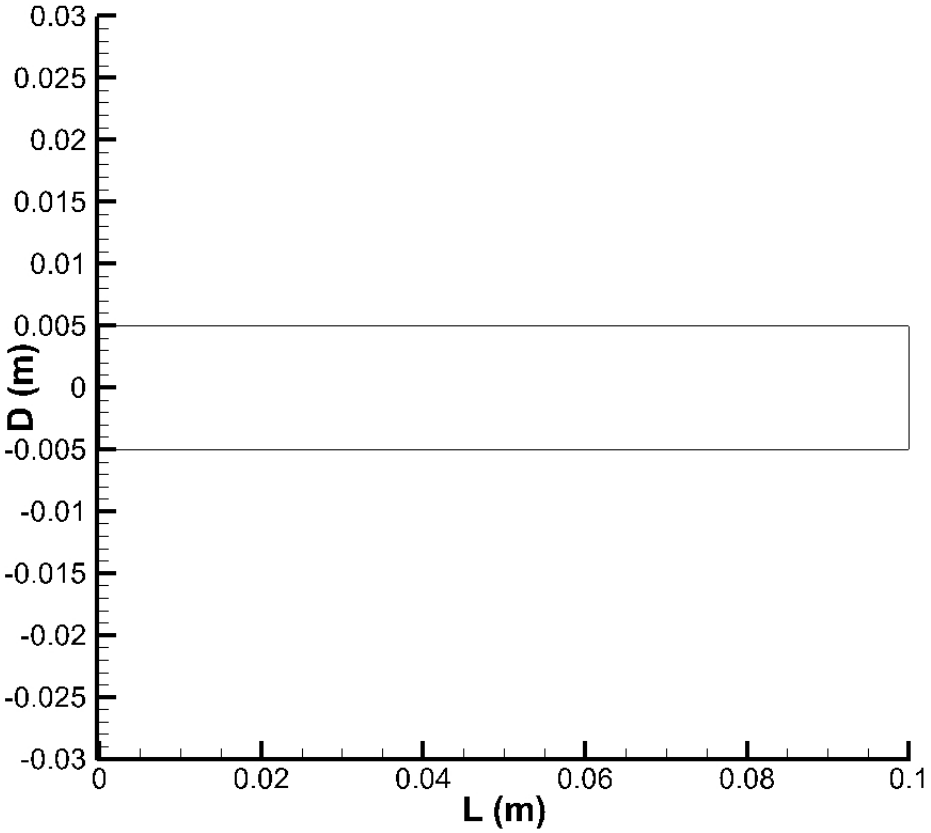

Figure 3.2: The 2-D channel geometry.

For this simple preliminary analysis, differently from [1] where a mesh of 2000 quadrilateral elements was used, a grid of approximately 14000 elements has been found to be more effective, providing high accuracy and agreement with the Tzirakis et al. results and keeping a low computational cost.

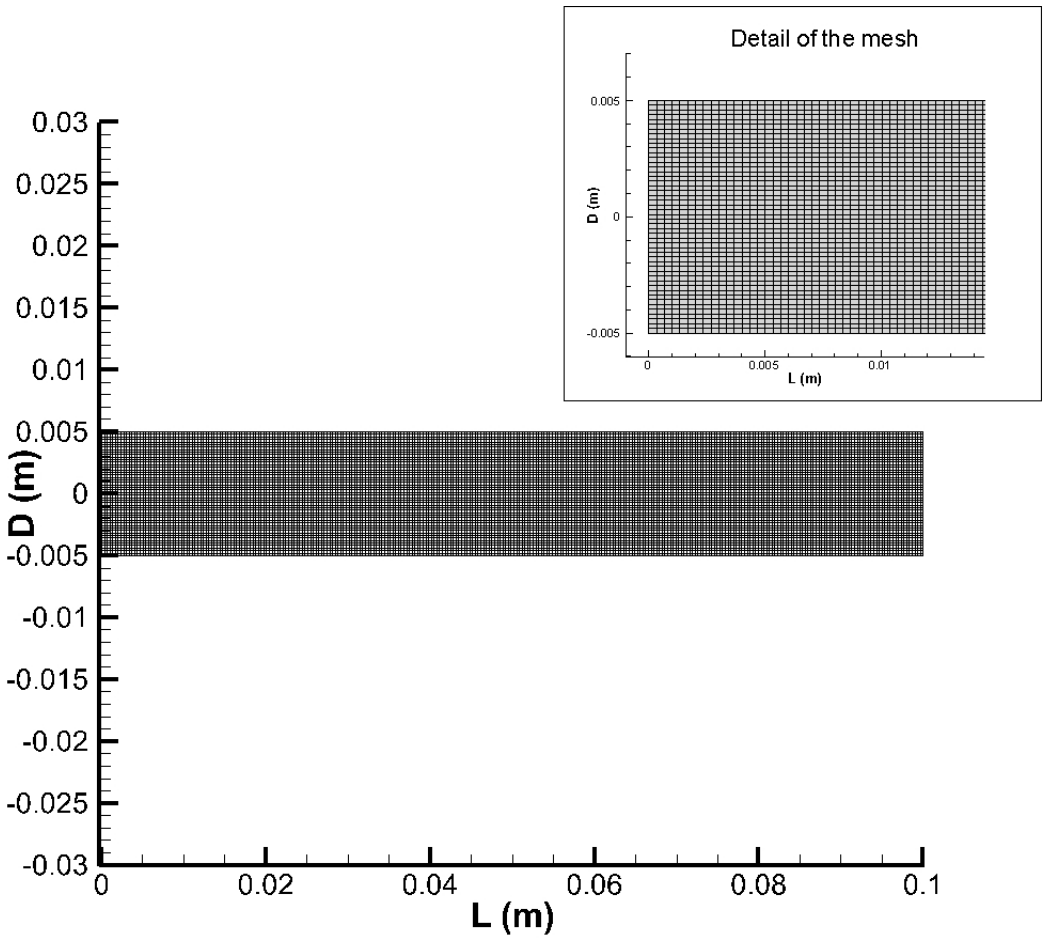

Figure 3.3: The 2-D channel mesh and detail of the inlet.

A single block has been generated for the interior (fluid) part and subsequently meshed with quadrilateral elements; final minimum orthogonal quality of 1.0, in a range between 0 (low) and 1 (high quality), has been achieved along with maximum aspect ratio of 1.91981, which denotes a slight elements elongation as can be found in Table 3.1 on page 33, where the main geometry and grid parameters are summarised.

		Height D (m)	**Length L (m)**
		0.01	10D = 0.1
Number of Elements	14651		
Number of Nodes	15000	50	300

Table 3.1: Geometrical and meshing parameters of the 2-D channel domain.

3.3.2 The 3-D Cylindrical Duct with the Stenosis

A three dimensional cylindrical duct has been the second domain considered. According to [1], this tube exhibits an axisymmetric stenosis located three diameters away from the inlet and ten upstream the outlet in order to let the flow to fully develop before the throat and to stabilise it before the outlet. The stenosis reduces the cross-sectional area of 84% and the diameter of 60%, which is set to 0.01 m; the length is 13D = 0.13 m.
The geometry has been generated based on the two curves used and provided in [1]:

$$F_1(x) = A \sec h\left[B(x - x_0)\right] - \frac{D}{2}, \tag{3.73}$$

$$F_2(x) = \frac{D}{2} - A \sec h\left[B(x - x_0)\right]. \tag{3.74}$$

where D is the tube diameter, the constants A and B define the construction and the extension of the stenosis, whereas x_0 determines the minimum location of the throat. From equations (3.73) and (3.74) it can be noticed that if A = B = 0, any stenosis is generated and the tube becomes a simple straight cylinder; however, parameters used by Tzirakis et al. and adopted for the present work have been set to: A = 0.3D, B = 6/D and x_0= 3D.

The geometry generation has been performed following three main steps:

1. The two curves $F_1(x)$ and $F_2(x)$ have been created using the MATLAB software; a ".dat" file has been exported with all the coordinates that define the two curves;

2. The curves points have been imported in ICEM-CFD and a 2-D surface profile of the actual geometry has been generated;

3. Finally, revolving the surface for 180, the three dimensional cylinder geometry with the stenosis has been extracted (Figure 3.4 on page 35).

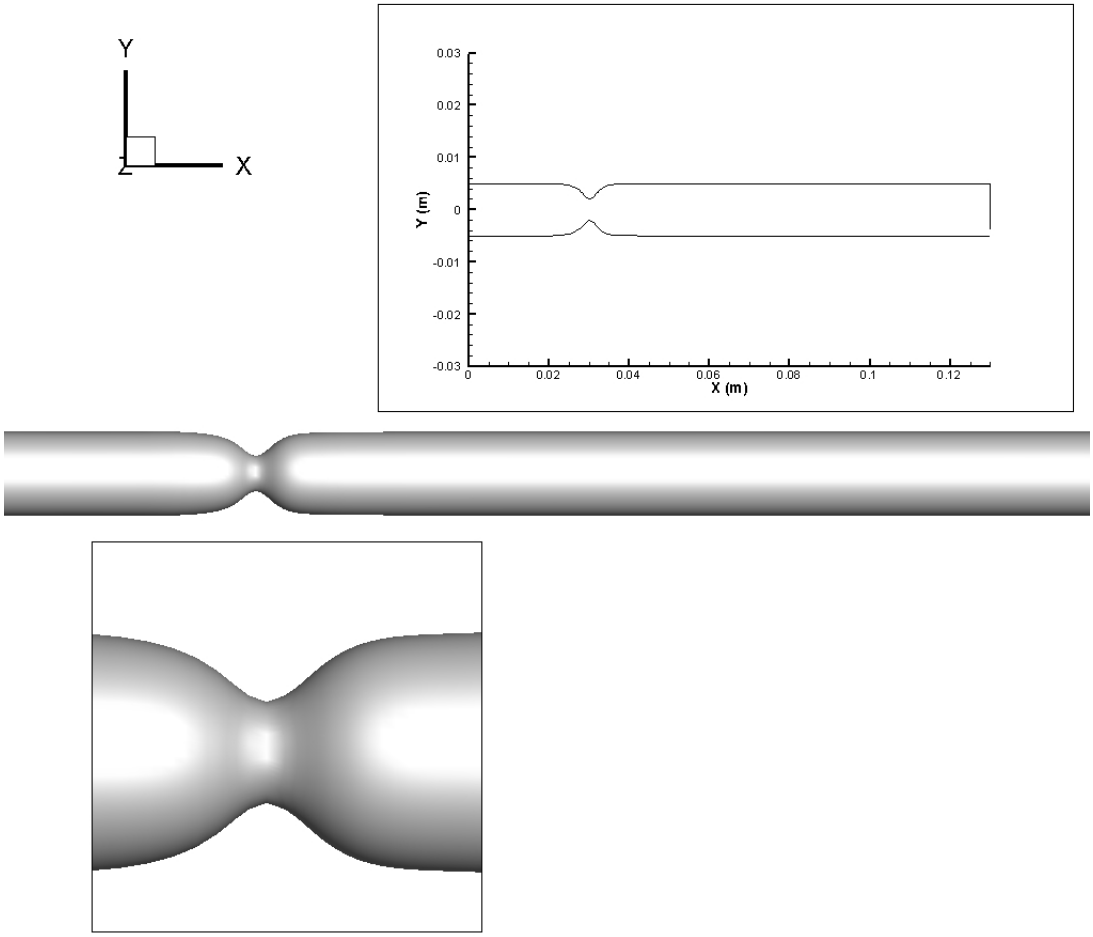

Figure 3.4: The 3-D Cylindrical tube with 60% diameter stenosis geometry.

The meshing process was much more complex than the previous 2-D geometry for the Hartmann flow; three different approaches have been tested in order to get the grid convergence and accurate results.
According to [1], a number of hexaedral elements between 120000 and 180000 are enough to obtain sufficiently accurate results, thus the first mesh has been generated with approximately 170000 elements (Figure 3.5 on page 36).

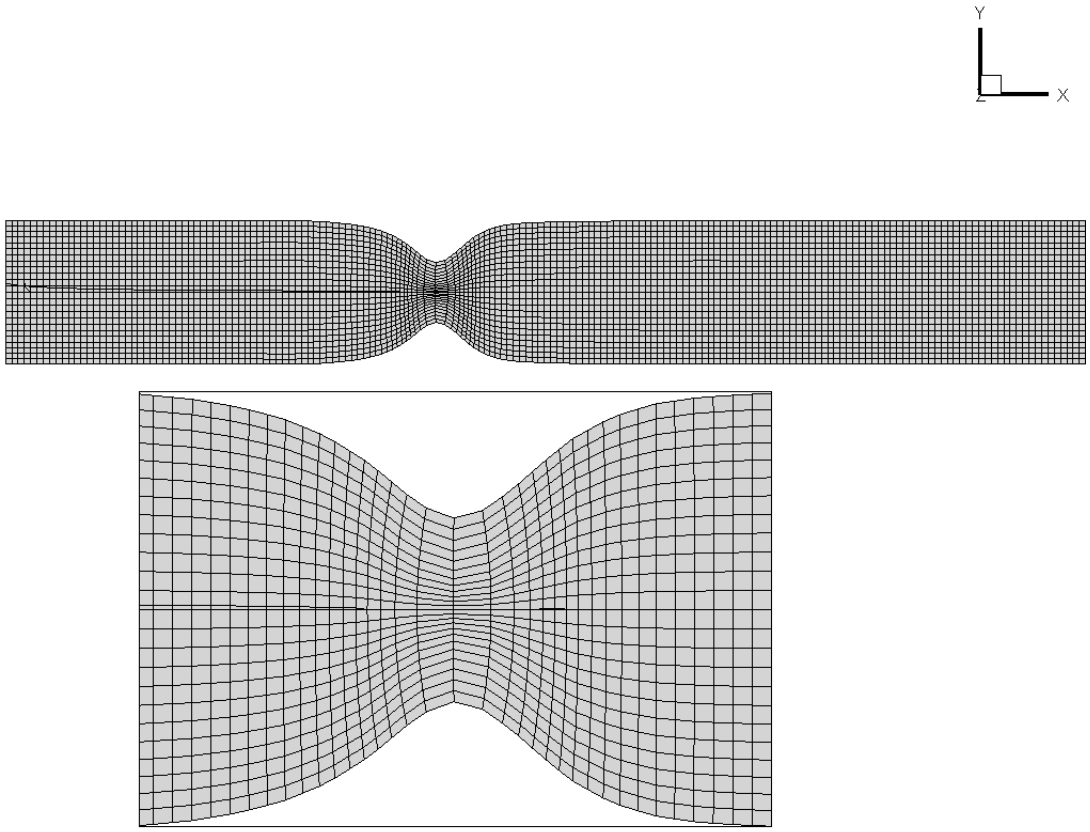

Figure 3.5: The initial coarse mesh.

A unique block has been generated for the fluid interior, and then, a structured hexaedral mesh has been constructed; no growing ratio for the boundary layer has been set and the element spacing has been retained constant, which ended up with moderately elongated elements. A spline tool has been used to fit the block sides to the curved shapes of the cylinder in order to obtain a lower skewness for the elements.

Number of elements	Number of nodes	Element Stretch (% of elements)		Aspect Ratio (Fluent) (% of elements)		Quality (% of elements)	
		Max	Min	Max	Min	Max	Min
172224	187500	0.997843 (14.8%)	0.0841107 (0.020%)	24.1825 (0.010%)	1.41625 (72.953%)	1 (42.6608%)	0.062264 (0.560%)

Table 3.2: Simple coarse grid parameters.

As it possible to notice from Table 3.2 on page 36, the percentage of stretched elements is not completely negligible, the aspect ratio range of the majority of elements, computed with the FLUENT parameter, is acceptable as well as the quality criterion, however, as Figure 3.5 on page 36 shows, this initial mesh appears to be quite coarse, especially around the throat zone.
Therefore, the second mesh has been generated with a cluster structure: the stenosis zone has been refined one diameter both upstream and downstream the throat. This refinement is motivated by the attempt to more accurately map the throat zone, where slopes become steeper and to capture more flow features, even because the magnetic field reaches its maximum intensity of 4 Tesla around that location (Figure 3.6 on page 37).

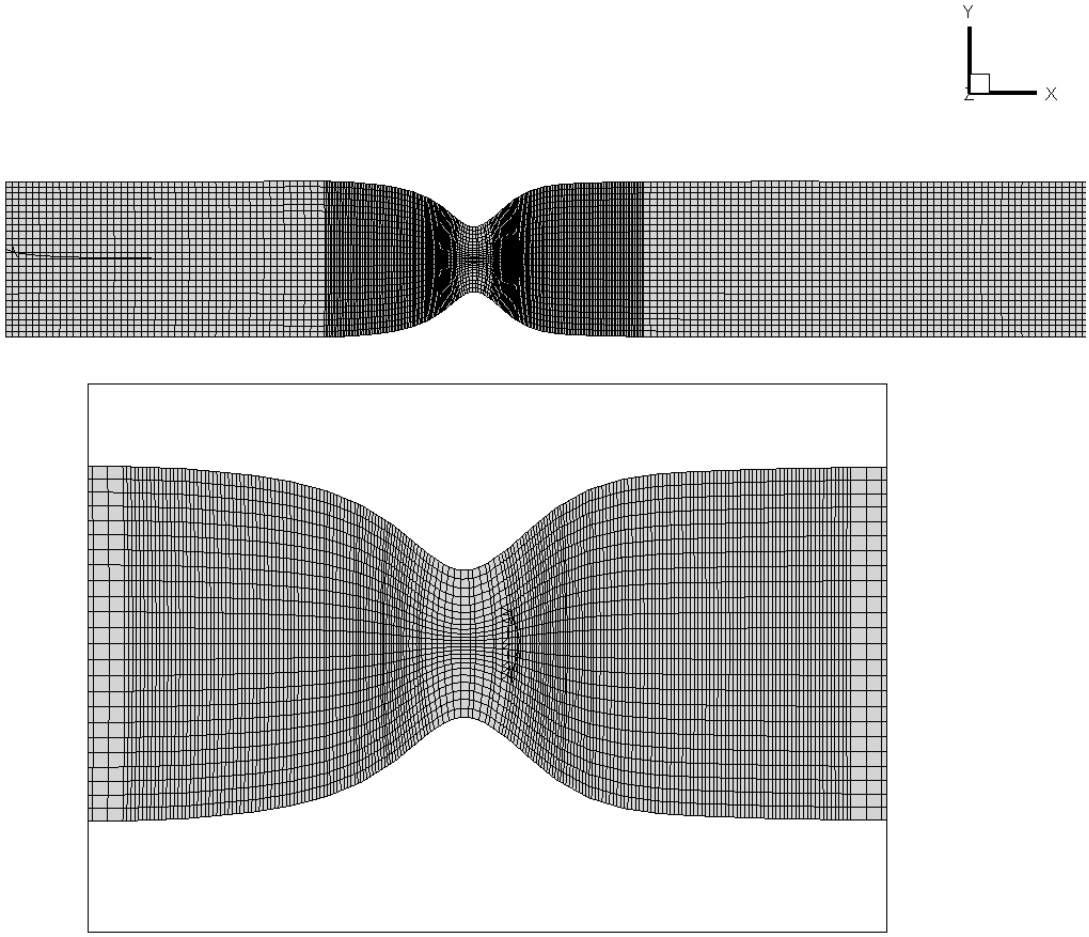

Figure 3.6: The clustered mesh.

Similarly to the initial simple mesh, also this second one has been generated without a proper boundary layer close to the wall, but as Table 3.3 on page 38 shows, the strategy

adopted provided better values for element stretch and aspect ratio.

Number of elements	Number of nodes	Element Stretch (% of elements)		Aspect Ratio (Fluent) (% of elements)		Quality (% of elements)	
		Max	Min	Max	Min	Max	Min
259776	282500	0.997843 (9.371%)	0.101157 (0.542%)	20.4564 (0.007%)	1.41625 (32.638%)	1 (41.611%)	0.0550659 (0.508%)

Table 3.3: The clustered mesh parameters.

The final finer mesh has been generated due to the poor performances of the previous two. The unsatisfactory accuracy in terms of y and z-velocity components and the unstable behaviour when the rotational magnetic field is applied, have been identified as the main problems of the two other meshes: these inadequate results have been caused by the inability of the meshes to capture the strong velocity gradients that arise close to the walls.
As the previous two grids, this final one has been generated with hexaedral elements, however the interior block has been split creating an O-grid. This allows to set a variable element spacing which gradually increases from the walls to the interior. The first element has been located $5 \cdot 10^{-5}$m away from the wall and a growing ratio of 1.2 has been set. The choice of that first element distance has been based on [1] and has allowed to obtain a smooth and refined zone around the stenosis throat as can be observed from details (a) and (b) in Figure 3.7 on page 39.

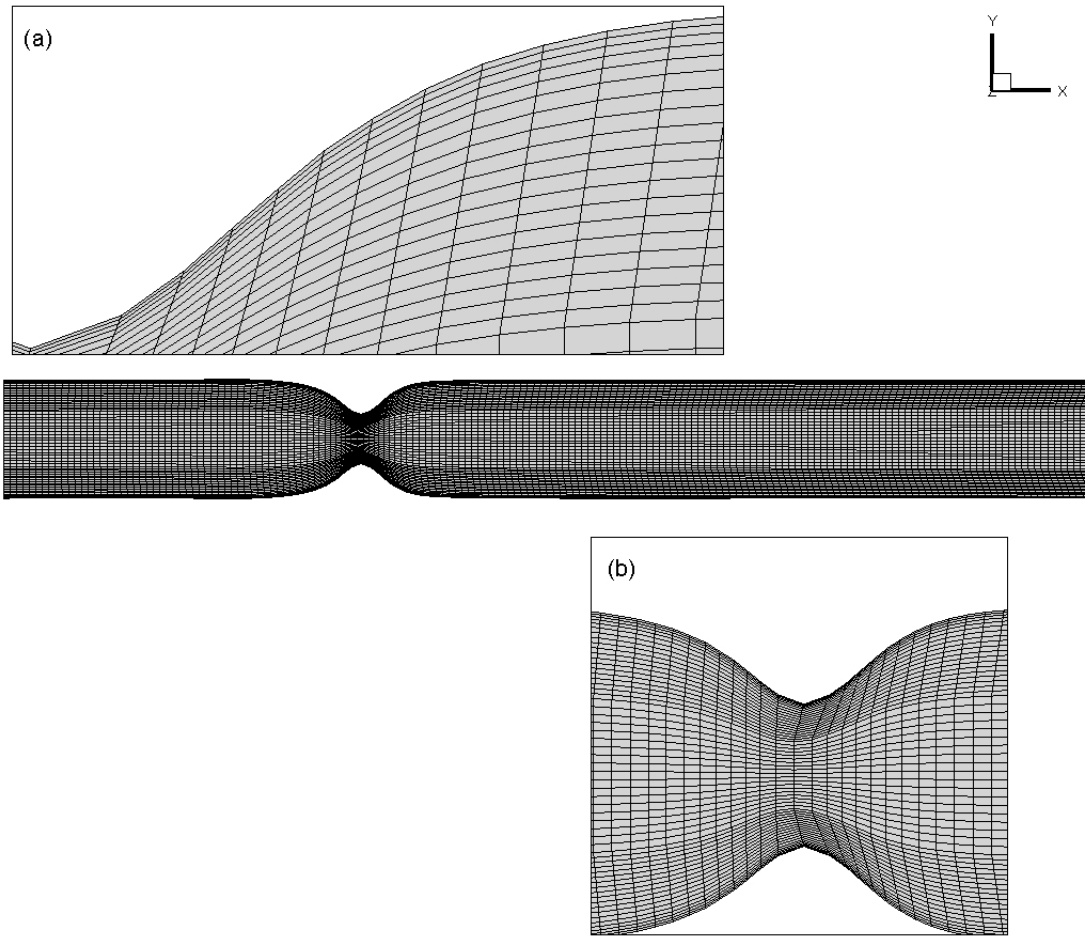

Figure 3.7: The final fine mesh. Detail of the boundary layer (a) and the stenosis zone (b).

Table 3.4 on page 39 provides the key mesh parameters: despite a considerable increase of elements number, especially if compared with the initial mesh, this meshing strategy has provided more accurate and reliable results in terms of flow physics and has produced a grid with higher quality and aspect ratio. It has also reduced the maximum element stretch. With this final mesh the grid convergence has been achieved.

Number of elements	Number of nodes	Element Stretch (% of elements)		Aspect Ratio (Fluent) (% of elements)		Quality (% of elements)	
		Max	Min	Max	Min	Max	Min
438252	448716	0.998191 (0.037%)	0.0632685 (0.090%)	35.8719 (0.004%)	1.41592 (3.272%)	1 (43.896%)	0.0622604 (0.001%)

Table 3.4: The fine mesh parameters.

Should be mentioned that the numbers of elements and nodes have been obtained by

FLUENT, while all the other grid statistics (stretch, aspect ratio and quality) have been provided by ICEM-CFD.

3.3.3 The Real 3-D Aorta Model

In order to perform analyses on a real high-fidelity domain and obtain realistic results for the blood flow, a three dimensional model for a real segment of Aorta with a length of 0.266 m has been considered.
The CAD (STL) file has been taken from ANSYS ICEM-CFD models database: this geometry has been reconstructed from a sequence of overlapped MRI images recreating an high-fidelity model.

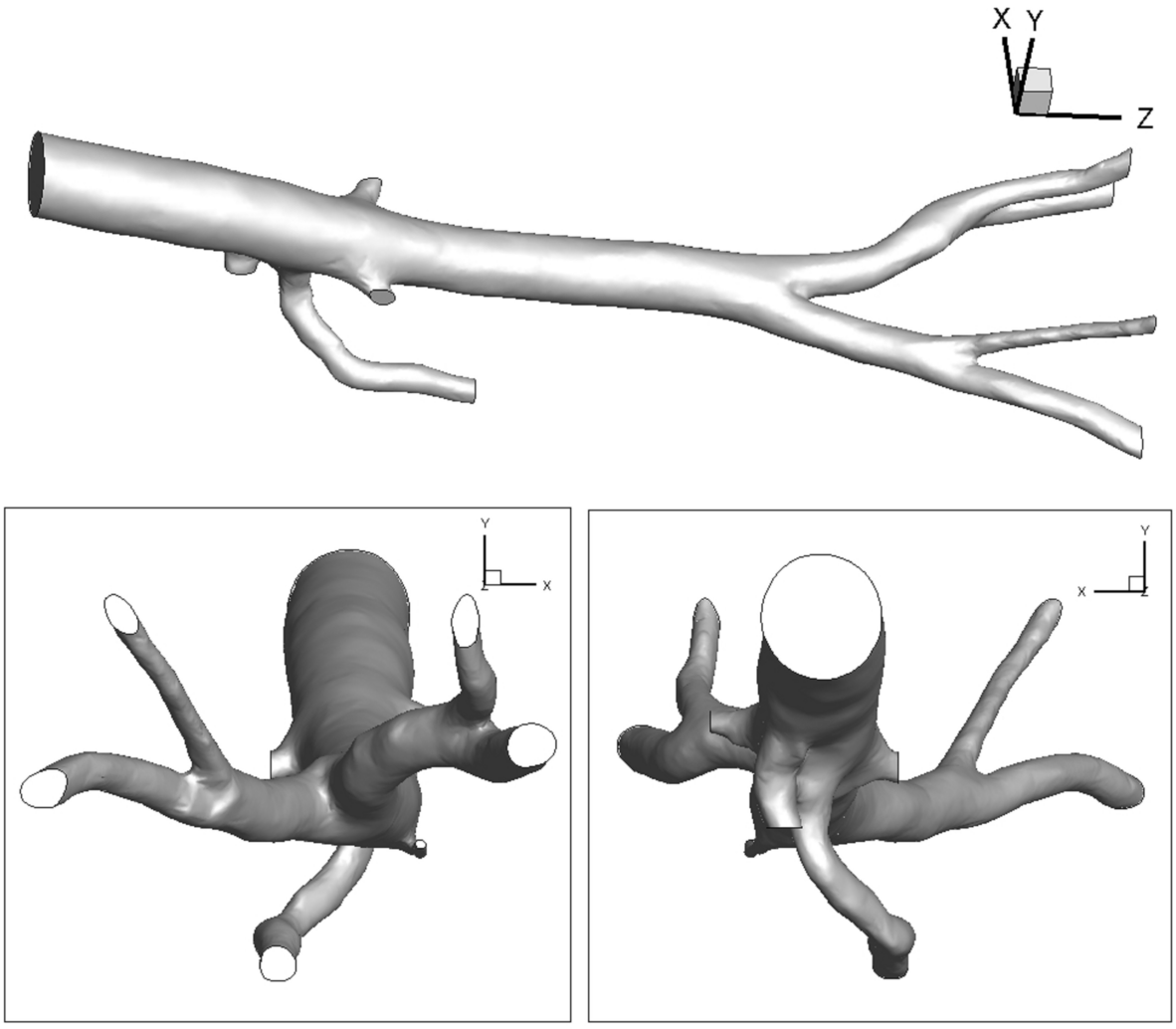

Figure 3.8: The Aorta 3-D geometry.

Three different meshes has been generated in order to assess the grid convergence, but, differently from the stenosis case, the same meshing strategy has been used for all the Aorta grids only increasing the number of elements. Moreover, for the Aorta a core of tetrahedral elements with a three-layers of quads close to the wall, in order to create a boundary layer, have been used. The meshing procedure can be summarised in the following steps:

1. After having extracted and generated the surfaces from the geometry, a first Octree mesh has been produced with three prism layers growing from the walls; the smallest element dimension has been based on the smallest diameter (approximately

0.015 m) of the geometry (outlet 4 Figure 3.9 on page 42), while the layers growing ratio has been set to 1.2;

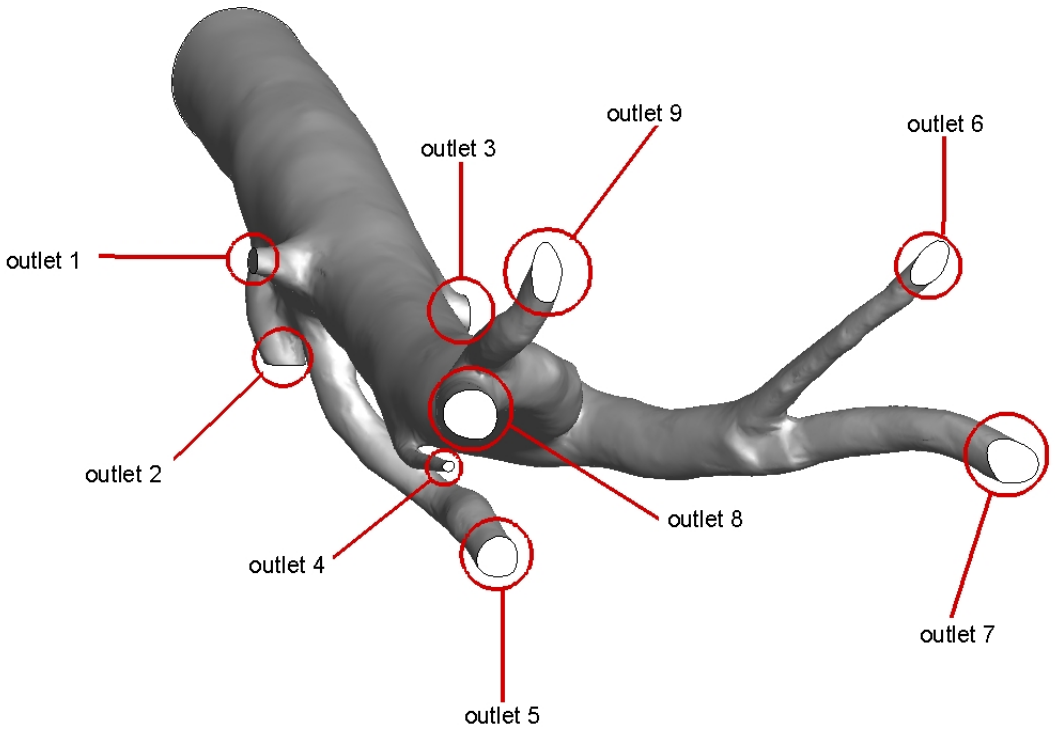

Figure 3.9: Map of the Aorta model outlets.

2. A number of 25 smoothing iterations, based on the quality criterion, have been performed;

3. Consequently, a Delaunay meshing procedure has been applied on the smoothed mesh in order to refine the capillaries narrow zones;

4. At last, a final smoothing sequence has been run in order to obtain the definitive grid (Figure 3.10 on page 43).

The final grid parameters are detailed in Table 3.5 on page 44.

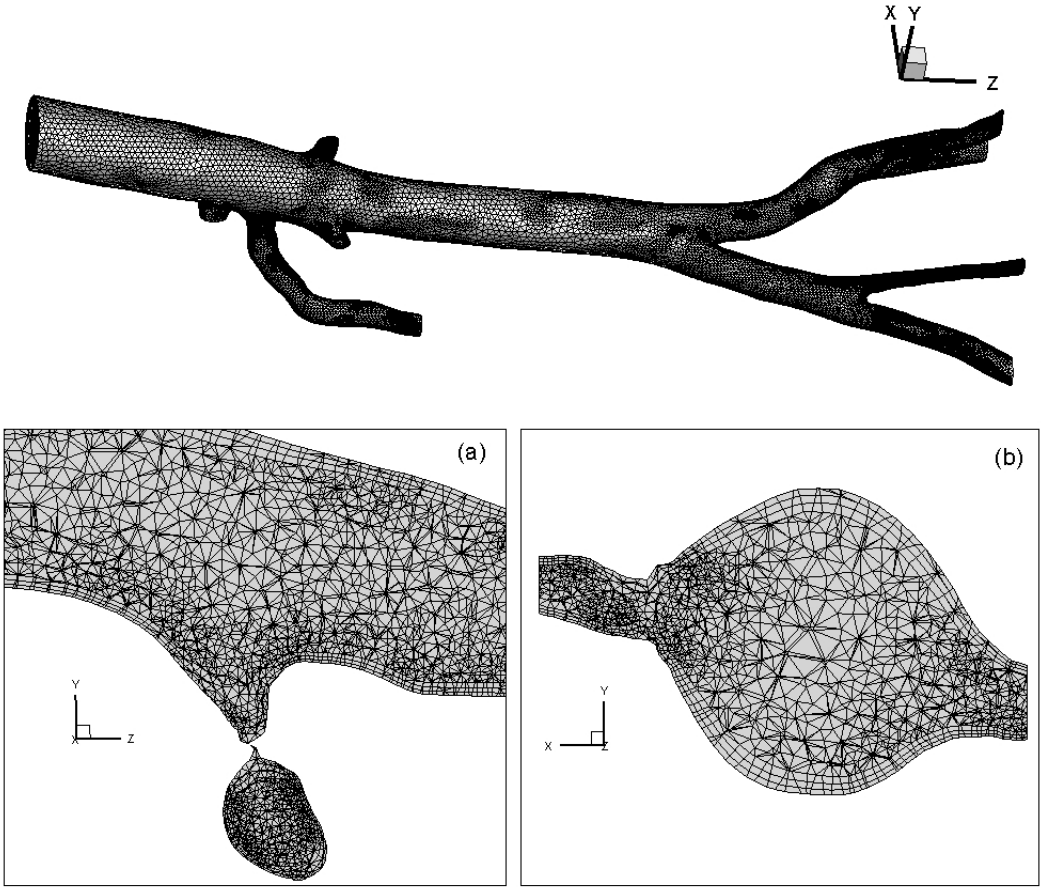

Figure 3.10: The Aorta final (medium) mesh. zy-plane detail (a); xy-plane detail (b).

	Number of elements	Number of nodes	Element stretch (elements %)		Aspect Ratio (Fluent) (elements %)		Quality (elements %)	
			Max	Min	Max	Min	Max	Min
Coarse mesh	516734	179779	0.99961	0.06334	71.3379	1.4356	0.99994	0.01341
			(2.496%)	(0.0%)	(0.0%)	(40.34%)	(1.484%)	(0.006%)
			(13.823% within 0.84966 and 0.8997)		(45.868% within 3.5669 and 7.134)		(23.628% within 0.85 and 0.9)	
Medium mesh	714829	212604	0.999605	0.126011	38.0346	1.5921	0.99945	0.04652
			(1.964%)	(0.002%)	(0.0%)	(0.006%)	(2.449%)	(0.0%)
			(12.963% within 0.7497 and 0.79967)		(59.451% within 3.804 and 5.705)		(23.816% within 0.85 and 0.9)	
Fine mesh	964887	306866	0.999679	0.090014	55.0655	1.4767	0.99963	0.0108
			(2.084%)	(0.0%)	(0.0%)	(9.105%)	(6.556%)	(0.004%)
			(11.638% within 0.69978 and 0.749759)		(80.194% within 2.7533 and 5.5066)		(19.646% within 0.85 and 0.9)	

Table 3.5: Mesh key parameters for the three grids generated.

As it possible to notice from Table 3.5 on page 44, the three meshes have similar values for element stretch: predictably, the stretch slightly decreases with the mesh refinement. By the way, greater differences can be detected for the aspect ratio where medium and fine meshes show low values which is a positive feature, especially in the latter case, however, in terms of quality, higher values can be found for the coarse and medium meshes with respect to the finest one.
The grid convergence study, presented later on, has determined the best mesh for the purpose, taking into account both the accuracy and the computational time.
As it has been stated for the 3-D stenosis, all the informations regarding the number of elements and nodes, have been obtained form FLUENT, while the parameters that describes the different quality aspects have been provided by ICEM-CFD.

3.4 The Solver Set-Up

In this sections the main solver set-ups for the different simulations are discussed and motivated, taking into account the numerics, the UDFs settings, the material properties and the boundary conditions.
All the simulations have been run using the ANSYS FLUENT software in double precision mode; no parallel computations have been performed due to the unpredictable behaviour of the UDFs with parallelisation.

Before specifying all the different parameters and settings that have been defined, should be mentioned that all simulations have been run for laminar viscous regime: no turbulence has been taken into account.

First of all, the UDF source code has been loaded, compiled and all the terms have been assigned to their own location; UDMs have been enabled as well as the source terms for the momentum equations. Secondly, material properties and boundary conditions have been imposed for each different case.

$\mu_0\ (H/m)$	χ_{deox}	$K\ (T \cdot m)$	$C\ \left(T \cdot m^4\right)$
$1.256637 \cdot 10^{-6}$	$3.5 \cdot 10^{-6}$	0.01024	$1.72 \cdot 10^{-10}$

Table 3.6: Magnetic field parameters.

Table 3.6 on page 45 points out the magnetic parameters that have been used within the UDFs, where, according to [1], constants K and C have been chosen in order to obtain a value of 4 T for both irrotational and rotational magnetic fields magnitude. Those parameters are common for magnetic fields.

3.4.1 The Hartmann Flow simulations Set-Up

The Hartmann flow has been studied first, considering a Newtonian fluid with density and viscosity of blood $\rho = 1050\,kg/m^3$ and $\mu = 0.0035\,Pa \cdot s$ respectively, and retaining the FLUENT default material (aluminium) for the walls.
Boundary conditions are provided in Table 3.7 on page 45:

	Type	**Value**
Inlet	velocity inlet	0.1 m/s (velocity magnitude)
Outlet	outflow	1 (flow rate weighting)
Walls	wall	stationary wall

Table 3.7: Boundary conditions for the 2-D channel.

The choice of the inlet velocity has been based on [1], as well as the magnetic field, which has been taken as $B_0 = 25\sqrt{7}\,T$, obtained from an Hartmann number of 5: should be remarked that this value of magnetic field is considerably high and unsuitable for biomedical applications.

In terms of numerics, steady pressure-based solver has been set-up as Table 3.8 on page 46 shows:

Pressure-Velocity Coupling	**Spatial Discretisation**			**Convergence Criteria**
	Gradient	**Pressure**	**Momentum**	
SIMPLE	Least Squares Cell Based	2^{nd}Order	2^{nd}Order Upwind	$1 \cdot 10^{-4}$ (all residuals)

Table 3.8: Solution methods and convergence criteria for the Hartmann flow simulation.

Despite the simplicity of the flow, 2^{nd} order methods have been used in order to get high accuracy.

3.4.2 The 3-D Stenosis simulations Set-Up

Four different simulations have been run for the 3-D cylindrical stenosed tube: the two validation cases, with Newtonian blood flow and same material properties of the Hartmann case under the action of irrotational and rotational magnetic fields, a third simulation where the rotational magnetic field and slip boundary conditions have been considered and a final simulation for the non-Newtonian blood subject only to the rotational field. Should be mentioned that wall material properties have been changed in order to mimic a real human vessel for the non-Newtonian case.

3.4.2.1 The Validation Cases

Regarding the simulations performed for the two 3-D validation cases, same boundary conditions have been applied:

	Type	**Value**
Inlet	velocity inlet	fully developed profile
Outlet	pressure outlet	0 (Pa gauge pressure)
Walls	wall	stationary wall

Table 3.9: Boundary conditions for the 3-D Newtonian blood flow within the stenosed tube.

According to the Tzirakis et al. [1] work, a fully developed velocity profile has been imposed at the inlet, as it possible to notice from Table 3.9 on page 46. The inlet profile has been obtained by extracting the outlet values of a simulation run for a 20D long tube

without the stenosis: the cylinder has been chosen with the same diameter and the fluid with the same conditions than the stenosed one, with the regime of Re = 100.

Considering the numerical settings, Table 3.10 on page 47 illustrates the choices for these validation test cases:

Pressure-Velocity Coupling	**Spatial Discretisation**			**Convergence Criteria**
	Gradient	**Pressure**	**Momentum**	
SIMPLE	Least Squares Cell Based	2^{nd}Order	2^{nd}Order Upwind	$1 \cdot 10^{-9}$ (all residuals)

Table 3.10: Solution methods and convergence criteria for the 3-D stenosis validation cases.

The 2^{nd} order has been found to give sufficiently accurate results without increasing dramatically the computational time. Despite the solution method settings have been retained identical to the Hartmann flow case, the convergence criteria have been considerably increased up to 10^{-9} due to the necessity to reach a stable and developed solution for y and z-velocity components.

3.4.2.2 The non-Newtonian Rotational Case

For the non-Newtonian blood flow subject to the rotational magnetic field in the three-dimensional stenosis, both boundary conditions and material properties have been changed: the blood has no longer been considered Newtonian, additionally, in order to mimic a realistic blood flow, the energy equation has been enabled; material properties for walls have been also changed in order to replicate a human vessel.

Density (Kg/m^3)	C_p**(Specific Heat)** $(J/Kg \cdot K)$	**k (Thermal Conductivity)** $(W/m \cdot K)$	**Viscosity** $(Pa \cdot s^n)$	
			k_0 **(P-L viscosity coefficient)**	n **(P-L exponent)**
1050	3617	0.52	$14.67 \cdot 10^{-3}$	0.7755

Table 3.11: The non-Newtonian blood properties.

Density (Kg/m^3)	C_p**(Specific Heat)** $(J/Kg \cdot K)$	**k (Thermal Conductivity)** $(W/m \cdot K)$
1059.9	3306	0.46

Table 3.12: Human vessel tissue material properties.

As it possible to notice from Table 3.11 on page 47, and as previously mentioned in 3.1.4, a Power-Law model has been considered in order to characterize the non-Newtonian behaviour of blood: along with viscosity coefficient and P-L exponent a maximum and minimum values of viscosity have been set to, 0.00453 $Kg/m \cdot s$ and 0.0021 $Kg/m \cdot s$ respectively, in order to bound the variation between realistic values.

	Type	**Value**	
Inlet	velocity inlet	**Momentum**	**Thermal**
		fully developed profile	310.15 K
Outlet	pressure outlet	0 (Pa gauge pressure)	310.15 K
Walls	wall	stationary wall	310.15 K

Table 3.13: Boundary conditions for the non-Newtonian 3-D stenosis simulation.

Table 3.13 on page 48 details the boundary conditions applied: as it can be observed a constant value of 310.15 K (37 C°) for the temperature has been set at every boundaries: this assumption is motivated by the fact that blood and vessels are presumed in thermal equilibrium and the temperature variations are usually negligible.
Similarly to the validation cases, a fully developed profile has been imposed at the inlet: the same geometry has been used to let the flow develop, however the inlet velocity has been derived form the non-Newtonian Reynolds number ((3.68)). A value of 100 has been considered for the Re, but, due to its different formulation, the velocity derived has been found to be greater than the Newtonian case.

Pressure-Velocity Coupling	**Spatial Discretisation**				**Convergence Criteria**
	Gradient	**Pressure**	**Momentum**	**Energy**	
Coupled	Least Squares Cell Based	2^{nd} Order	2^{nd} Order Upwind	2^{nd} Order Upwind	$1 \cdot 10^{-9}$ (cont & vel residuals) $1 \cdot 10^{-6}$ (energy residuals)

Table 3.14: Solution methods and convergence criteria for the non-Newtonian 3-D stenosis simulation.

Differently to what has been set-up for the previous cases, as it possible to notice from Table 3.14 on page 48, a pressure-velocity coupling has been adopted for the non-Newtonian simulation: this solution method proved to enhance the stability of the solution and provided more accurate results. Moreover, a pseudo-transient procedure has been adopted in order to avoid the reversed flow at the outlet.

3.4.2.3 The Newtonian 3-D Stenosis with the Rotational Magnetic Field and the Slip Boundary Condition

The Newtonian rotational case with the slip boundary condition is the last case considered for the stenosed tube. Boundary conditions have been retained the same presented in (3.9) with the exception of the slip condition at walls: a moving wall condition with a slip velocity profile implemented in the UDF, has been imposed. Regarding the solution method, all the settings used for the other two validation simulations have been retained.

3.4.3 The Aorta Simulations Set-Up

The last analyses have been performed on the real Aorta 3-D model, for which two initial simulations have been run with both Newtonian and non-Newtonian blood properties, but without the rotational magnetic field, whereas the final simulations have been performed considering the non-Newtonian blood only, subject to the rotational magnetic field. The fluid parameters have been considered the same as highlight in 3.4.2.1 for Newtonian case and in Table 3.11 on page 47 for the non-Newtonian case; for both cases a realistic human tissue has been modelled for the wall boundaries (Table 3.12 on page 47).
Same boundary conditions as the 3-D non-Newtonian stenosis case have been imposed, with the only exception of the inlet velocity: in order to enhance the similarity to a real blood flow, a velocity magnitude of 0.11 m/s has been considered It is found to be approximately the average blood velocity within the Aorta artery.

Pressure-Velocity Coupling	**Spatial Discretisation**				**Convergence Criteria**
	Gradient	**Pressure**	**Momentum**	**Energy**	
Coupled	Least Squares Cell Based	2^{nd} Order	2^{nd} Order Upwind	2^{nd} Order Upwind	$1 \cdot 10^{-5}$ (cont & vel residuals) $1 \cdot 10^{-6}$ (energy residuals)

Table 3.15: Solution methods and convergence criteria for the Aorta simulations.

As it possible to notice from Table 3.15 on page 49, the only difference with the non-Newtonian stenosis case regards the convergence criteria for continuity and velocity: in the Aorta case a limit of 10^{-5} has been set due to the high computational time required by the simulations. Pressure-based steady solver has been used as well.
Finally, should be remark that all the values for material properties of blood and vessel tissue have been provided by the on-line database [38] for all the cases.

Chapter 4

Results and Discussions

4.1 Results Overview

In the present chapter the final results are presented and discussed analysing and performing several comparisons between velocity, pressure and wall shear stresses fields. As previously mentioned, the final objectives of the present work are two: to prove and investigate the capabilities of a commercial software in model and to solve a multi-physic problem, studying from a more physical point of view the impact of the magnetic field on the blood flow in realistic scenarios. Moreover, all the simulations performed have followed a prescribed and systematic path in order to built a robust and coherent results structure: the sections and sub sections below are organized following this path. First of all, the validity and the reliability of the User-Defiend Functions are assessed, organizing the validation process in two steps, where some numerical results of Tzirakis et al. work [1] are replicated and compared with those obtained with the FLUENT:

1. A first preliminary simulation of the 2-D Hartmann flow is performed in order to check the effective interaction between UDFs and FLUENT solver, (results are presented in 4.2.1);

2. The actual validation of the UDFs is assessed through the comparisons of pressure and velocity profiles between Tzriakis et al. and FLUENT results for a three-dimensional Newtonian blood flow in the cylindrical stenosed tube. Both irrotational and rotational magnetic fields are considered.

After having achieved the UDFs validity, and before to move to more realistic cases, the effects of slip boundary conditions are investigated considering the rotational magnetic field case only.
Thereafter (Section 4.3), the blood physics is enhanced considering its non-Newtonian rheology; material properties of blood vessel tissue for wall boundaries are introduced

and the flow behaviour is studied still considering the stenosed tube, switching on and off the rotational magnetic field. Results are compared with the previous ones obtained for Newtonian fluid. This intermediate step for the non-Newtonian flow within the stenosed straight tube, is preparatory for the study on the fully real model of Aorta, for whom, again simulations followed a prescribed path where the fluid physics is enhanced step by step: Newtonian blood is considered first and then compared with the non-Newtonian Power-Law results. At this stage the magnetic field is absent.
Finally (Section 4.4), considering the only non-Newtonian model, the rotational magnetic field is switched on at three different locations sequentially along the cross-section in order to investigate the flow behaviour when perturbed by the field: these very final results are analysed also from biomedical point of view, trying to assess their reliability and truthfulness.

4.2 The UDFs Validation

The present section explains and provides results obtained for the validation of the UDFs: pressure and velocity fields are considered with both profiles at different sections and contours at xy plane.
Should be mentioned that all the results taken from [1] and used for the validation, are numerical: unfortunately, no experimental results are available in the literature for this kind of problem.

4.2.1 The Hartmann Flow

The two-dimensional Hartmann flow is the first preliminary case considered for the UDFs validation because the flow physics is simple, the domain small and it ended to be quick and cheap in computational terms, as it is explained in 3.1.1.
Considering the mesh and the parameters illustrated in 3.1.1, 3.3.1 and 3.4.1, the simulation for this case took just 145 iterations.

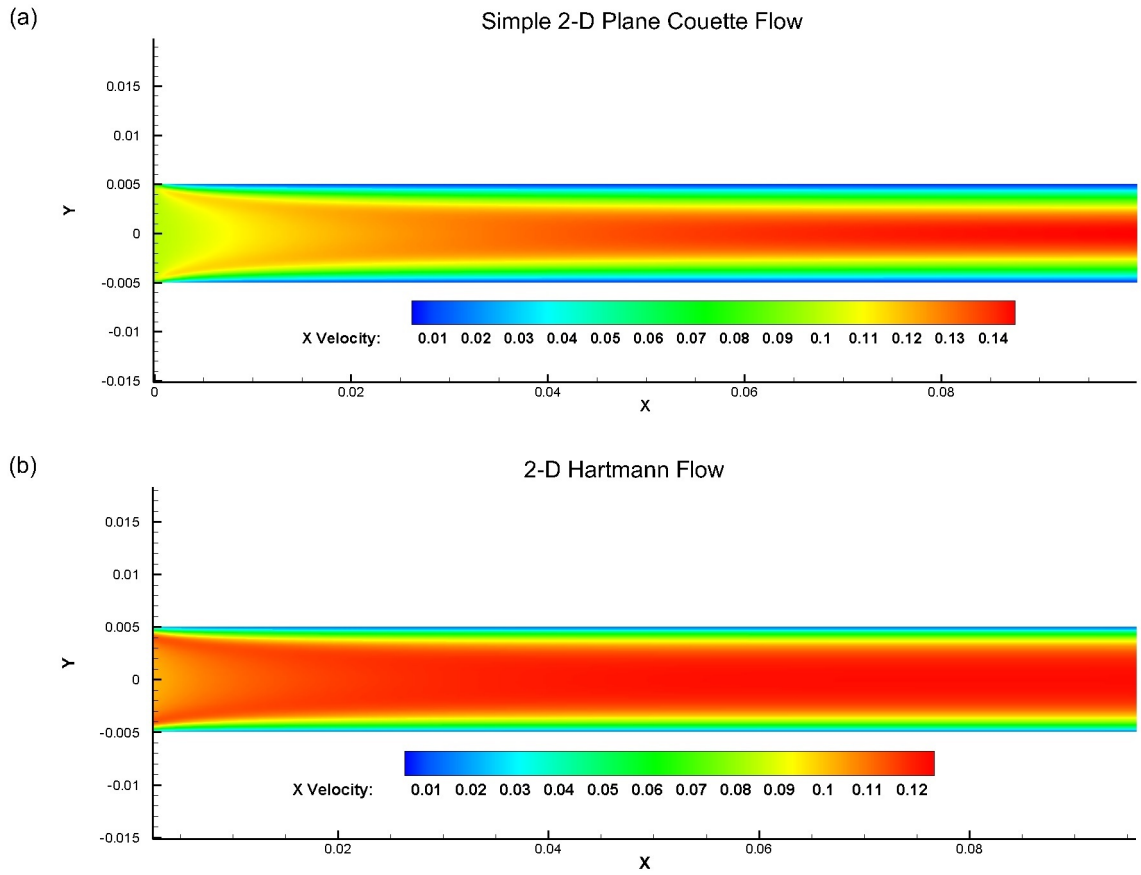

Figure 4.1: Comparison between the Plane Couette Flow and the Hartmann Flow for of x-velocity component in cross-sectional area.

From Figure 4.1 on page 52 above, the effect of the magnetic force (3.40) can be appreciated: the flow is slowed down under the action of the constant field. Additionally, comparing the Hartmann flow and the Couette flow, it can be inferred that the first develops quicker and with a flatter velocity profile at the outlet with respect to the second Figure 4.2 on page 53. This behaviour is caused by the magnetic field, which prevents and slows down the blood flow.

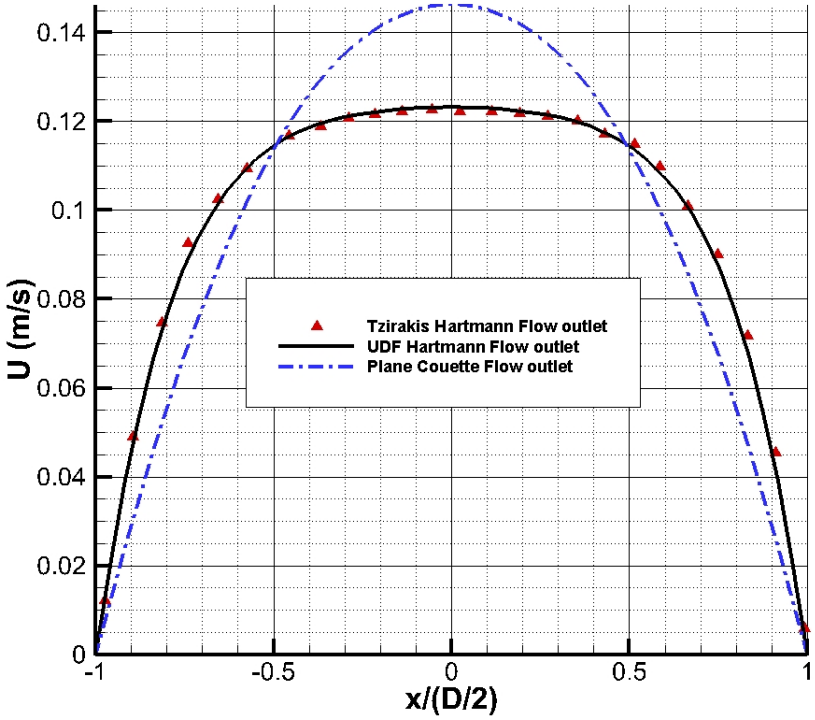

Figure 4.2: Comparison between the Plane Couette Flow, the Tzirakis et al. Hartmann Flow and the UDF Hartmann Flow for x-velocity profile at the outlet.

The agreement between Tzirakis e al. result and the one obtained using the UDF and the FLUENT is considerably high: this indicates that for a simple case, the UDF works correctly and the source term are properly treated by the FLUENT.
Should be remarked that, as all the other Tzirakis et al. comparative results, also the Hartmann flow outlet profile has been extracted from [1] through a digitalization procedure.

4.2.2 The Newtonian Blood Flow through a 3-D stenosed duct under the action of localised magnetic fields

After the preliminary validation of the UDF with the simple Hartmann case, the problem complexity is now enhanced, including the effect of both the magnetization and the Lorentz forces for the irrotational magnetic field (3.42), and the magnetization force for the rotational one (3.49). The present section provides, at a first stage, the grid convergence study performed for the 3-D cylindrical tube with the stenosis and secondly, results

for the final UDFs validation and the actual UDFs performances, comparing velocity and pressure profiles with the ones provided in [1] for both irrotational and rotational magnetic fields. Additional results are presented in terms of contours and stream traces and, in conclusion, 4.2.2.4 describes the main findings obtained form the comparison between the flow with and without wall slip boundary conditions in the same three-dimensional stenosed tube and in presence of the rotational magnetic field.

4.2.2.1 The Grid Convergence Study for the 3-D Stensoed Tube

To assess the grid convergence is a required practice in all the CFD analyses before performing any simulation. As introduced in 3.3.2, three meshes have been generated for the cylindrical stenosed tube. In order to evaluate the grid performances, an initial simulation has been run for each mesh considering Newtonian fluid without any magnetic field acting on it; results obtained, have been compared with the ones provided by [1] in terms of pressure and velocity components profiles along the symmetry axis.

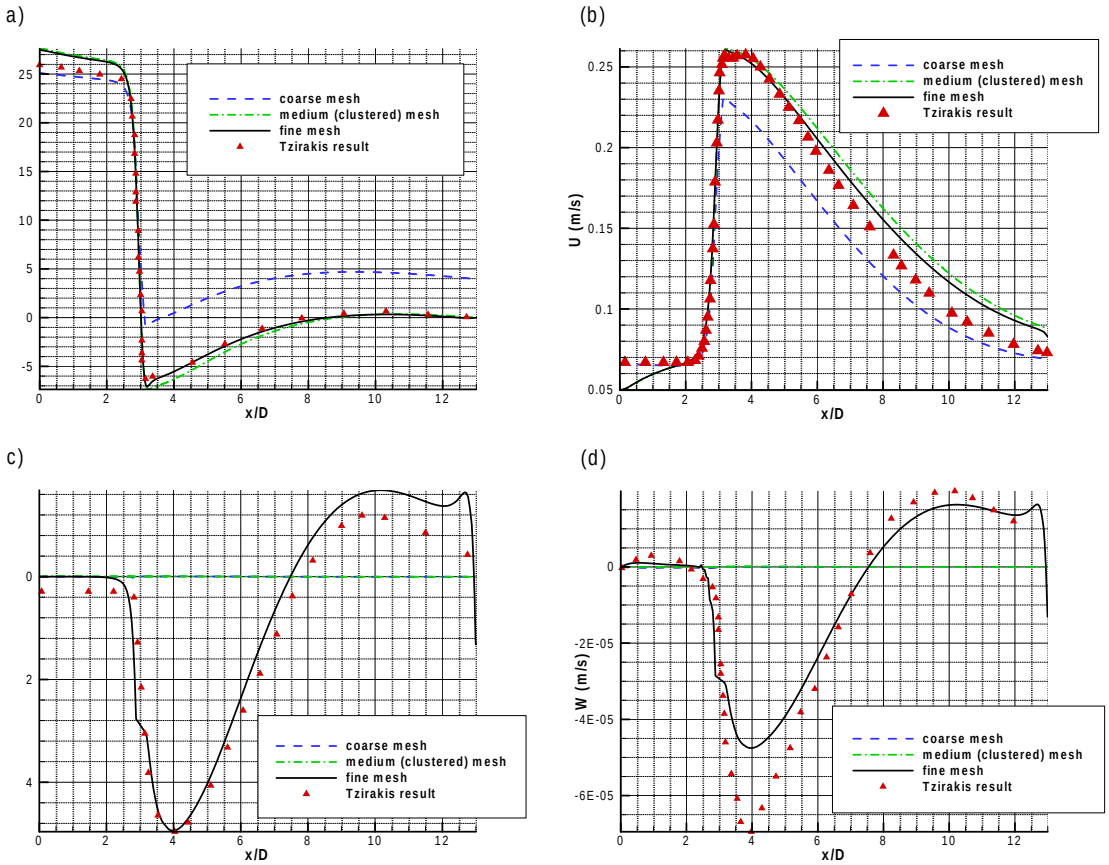

Figure 4.3: Comparison between the different grids in terms of pressure profiles (a); x-velocity component (b); y-velocity component (c); z-velocity component (d).

As it possible to notice from Figure 4.3 on page 55 (a-b), the medium mesh with a refined zone around the stenosis throat, and the fine one, where the boundary layer is modelled, preform satisfactorily in terms of pressure (a) and x-velocity (b), while the coarse mesh over-predicts the pressure field after the throat and under-shoots significantly the x-velocity maximum peak.
If only the pressure and the velocity fields are considered, then the medium and the fine meshes are equally satisfying, however, considering also the other velocity components, results highlight a huge performance gap, as Figure 4.3 on page 55 (c) and (d) show.
Both the coarse and the medium grid completely miss the y- and z-velocity profiles along the symmetry axis, showing a discrepancy of almost two orders of magnitude from the resutls obtained by Tzirakis et al. On the other hand, results provided by the fine mesh can be considered highly satisfactory, with a z-velocity maximum deviation of $2 \cdot 10^{-5}$m/s from Tzirakis et al. profile. The y-velocity accuracy is even better: the two profiles match almost completely. Therefore, through this comparisons, the higher accuracy and reli-

ability of the fine mesh and the importance of a properly modelled boundary layer are proven, especially when strong velocity gradients are involved and the orders of magnitude are small. In consequence of these findings, the fine mesh is used for all the other simulations that involved this kind of geometry.

4.2.2.2 The Irrotational Magnetic Field ([1] Case 2)

After having identified the adequate mesh, the UDF validation process is initiated, considering firstly the irrotational magnetic field. The magnetic field, then, is located at $x_i = 3.0D$ and $y_i = -0.5D$ in order to obtain $|B(x_0, y_0)| = 4T$ where $x_0 = 2.83D$ and $y_0 = -0.31D$. The magnetic field magnitude has the following general expression:

$$|B(x,y)| = \frac{K}{\sqrt{(x-x_i)^2 + (y-y_i)^2}} \tag{4.1}$$

The field structure is passed to the solver through the UDF and initialized, while the UDM stores its data, as Figure 4.4 on page 56 shows:

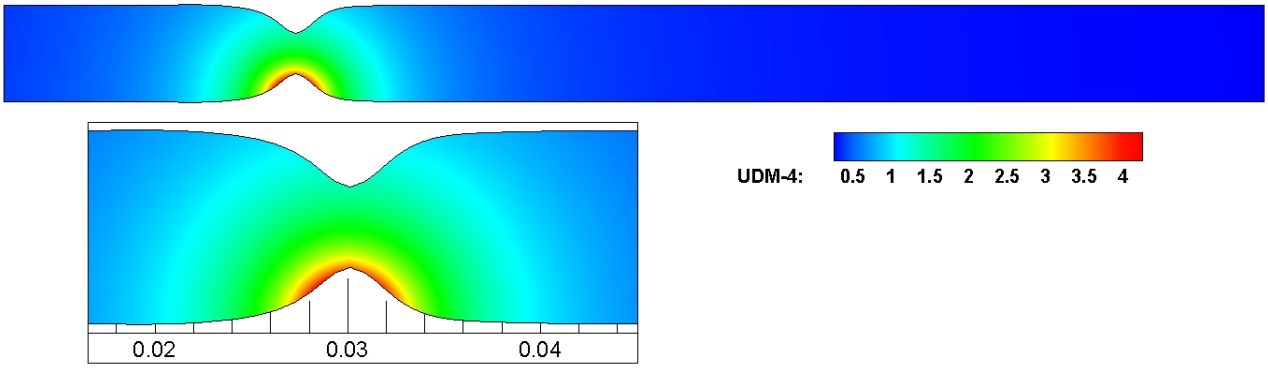

Figure 4.4: The irrotational magnetic field contours; z = 0 tube cross-section.

According to [1], in this irrotational case, the flow obeys to the MHD-FHD model, where both the Lorentz and the magnetization forces are present, therefore, in order to be consistent with the Tzirakis et al. work, two scenarios are considered:

1. $F_L = 0$ and $F_M > 0$: then, only the FHD equations are solved;

2. $F_L > 0$ and $F_M > 0$: the fully MHD-FHD model is considered.

All the results for the two sub-cases are compared against each other, the Tzriakis et al. ones and the others obtained for a magnetic-field-free flow, in terms of velocity and pressure profiles along the symmetry axis. Contours have been extracted z = 0 cross section. According to what Tzirakis et al. [1] have found, the irrotational magnetic field is supposed not to alter the velocity fields but only the pressure one (Figure 4.5 on page 57).

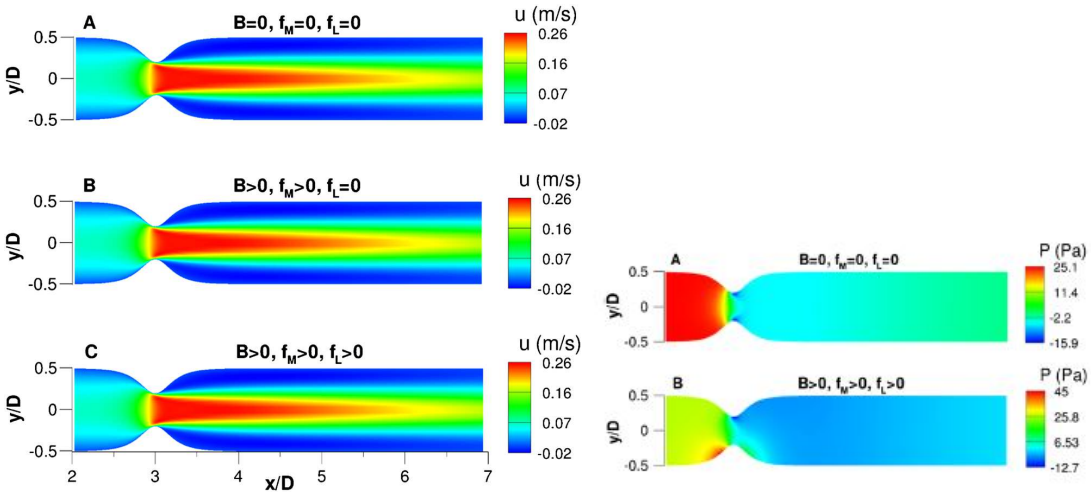

Figure 4.5: Stream-wise velocity and pressure results obtained by Tzirakis et al. [1] simulations for the irrotational magnetic field case. The contours are displayed one diameter upstream to four downstream the throat.

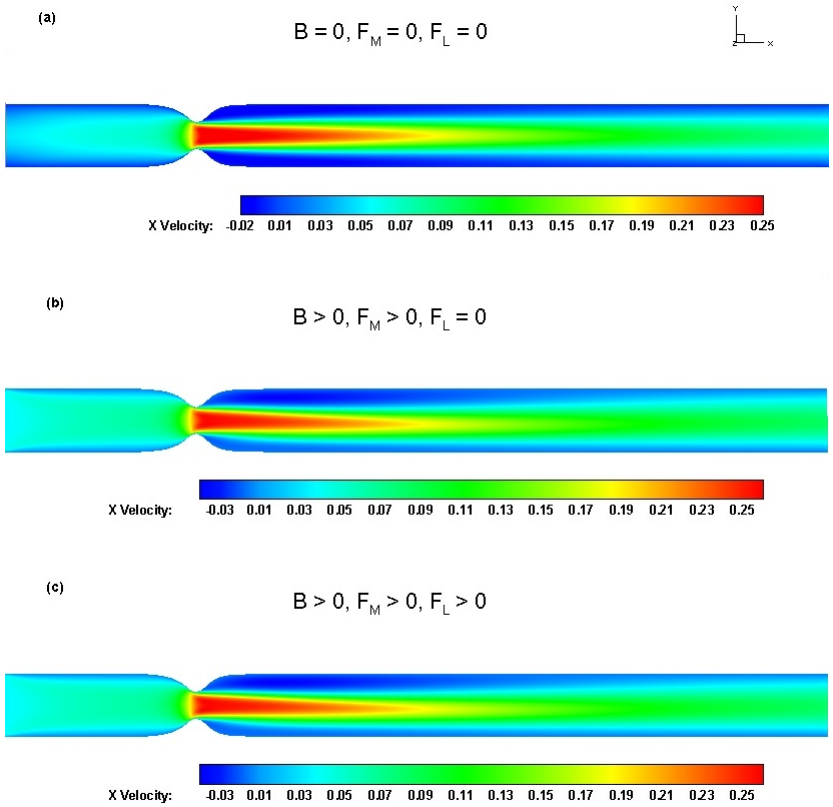

Figure 4.6: Stream-wise velocity field at z = 0. no forces (a), magnetization force only (b), both forces (c). Results provided by the UDF.

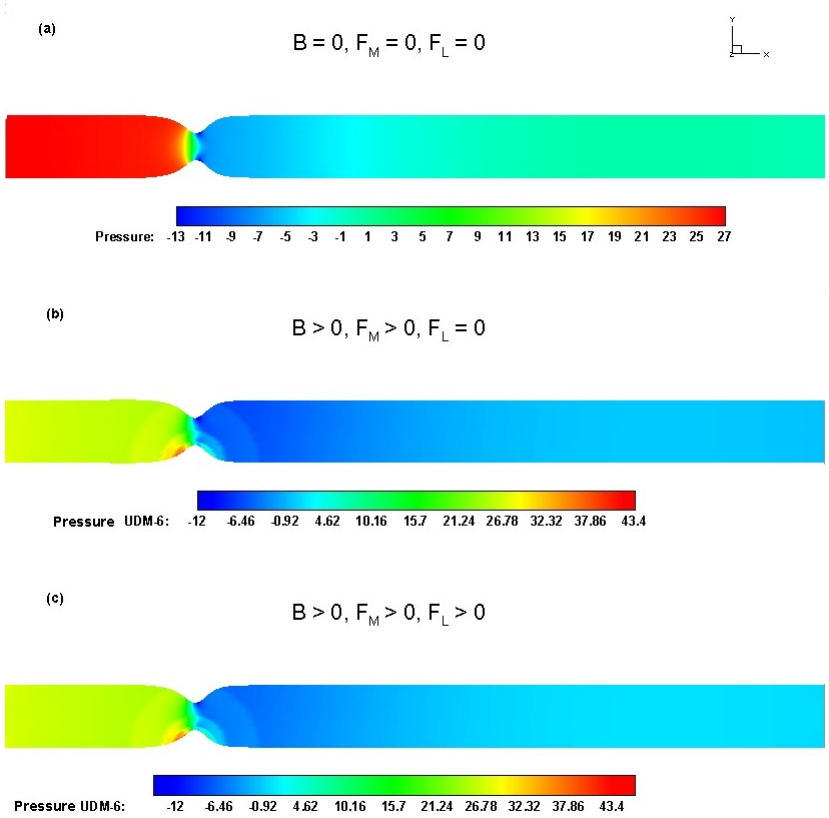

Figure 4.7: Pressure field at z = 0; no forces (a), magnetization force only (b), both forces (c). Results provided by the UDF.

As it is possible to notice comparing Figure 4.5 on page 57 with Figure 4.6 on page 58Figure 4.7 on page 59, the agreement between Tzirakis et al. results and ones obtained through the UDF implementation can be considered satisfactory both in terms of velocity and pressure contours. Indeed, looking closely to Figure 4.6 on page 58, only a small difference from Figure 4.5 on page 57 can be identified: when magnetization and Lorentz forces are present, (b-c), the flow appears to be slightly perturbed and deflected if compared with Tzirakis et al. results. This deviation could be ascribed to the different numerics used: while in [1] a high order finite element formulation has been implemented, a finite volume formulation is solved by FLUENT; this discrepancy turns to give a more diffusive behaviour for the FE formulation.
Despite this small distortion, it is clearly visible how the irrotational magnetic field implemented does not affect the velocity magnitude, as Tzirakis et al. have suggested; on the other hand, the presence of magnetic field largely influences the pressure field, which reaches higher values around the stenosis, where the field is located, if compared with the case where the field is absent: the maximum difference is around 72%.

From a physical point of view, the flow behaves as expected: the stenosis acts like a converging-diverging nozzle, where the flow accelerates, thus, as showed by Figure 4.5 on page 57, Figure 4.6 on page 58 and Figure 4.7 on page 59, the speed grows and the pressure decreases; later on, the sudden expansion, in the diverging zone, generates a recirculation region, clearly appreciable from Figure 4.8 on page 60.

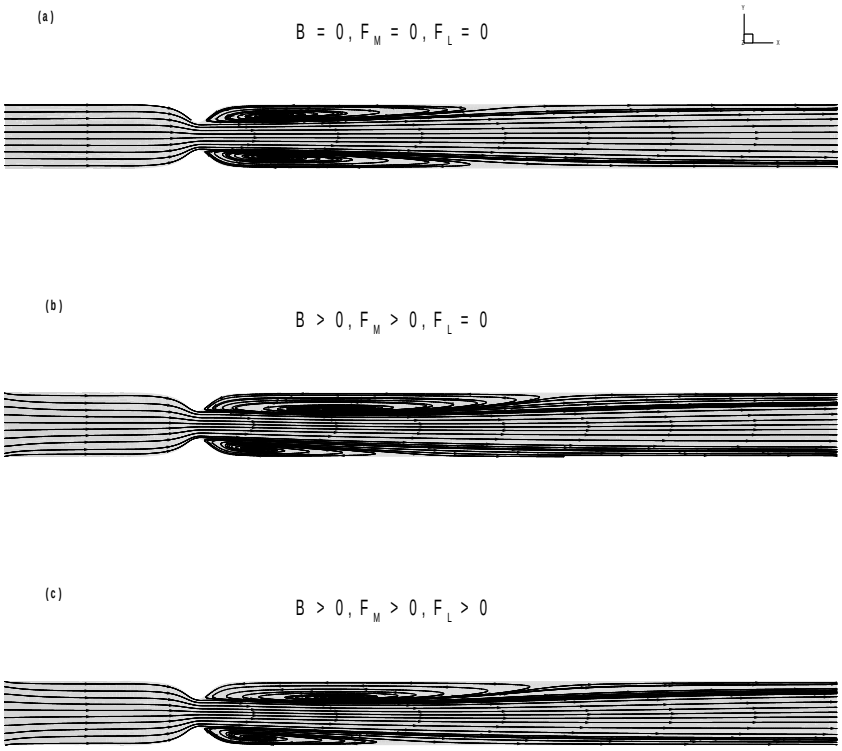

Figure 4.8: Stream-traces at z = 0 for the irrotational magnetic field obtained with the UDF; no forces (a), magnetization force only (b), both forces (c).

In terms of velocity and pressure profiles, a good agreement between the results obtained by the UDF and the ones provided by [1] is found: Figure 4.9 on page 61, confirms the satisfactory accuracy of UDF results, where all the trends are efficaciously replicated with an almost perfect match for x-velocity component (a) and pressure (d); only a slight discrepancy can be found at the inlet. The y- and z-components (b-c) capture the correct tendency, however, results for the z-component (c) miss the minimum in terms of magnitude.
As it can be noticed form Figure 4.9 on page 61 (d), pressure peaks obtained by FLU-

ENT UDF are sharper than the ones found in [1]; nevertheless, the tendency is completely caught. This difference could again be ascribed to the diffusive behaviour of finite-element method used by Tzirakis et. al.

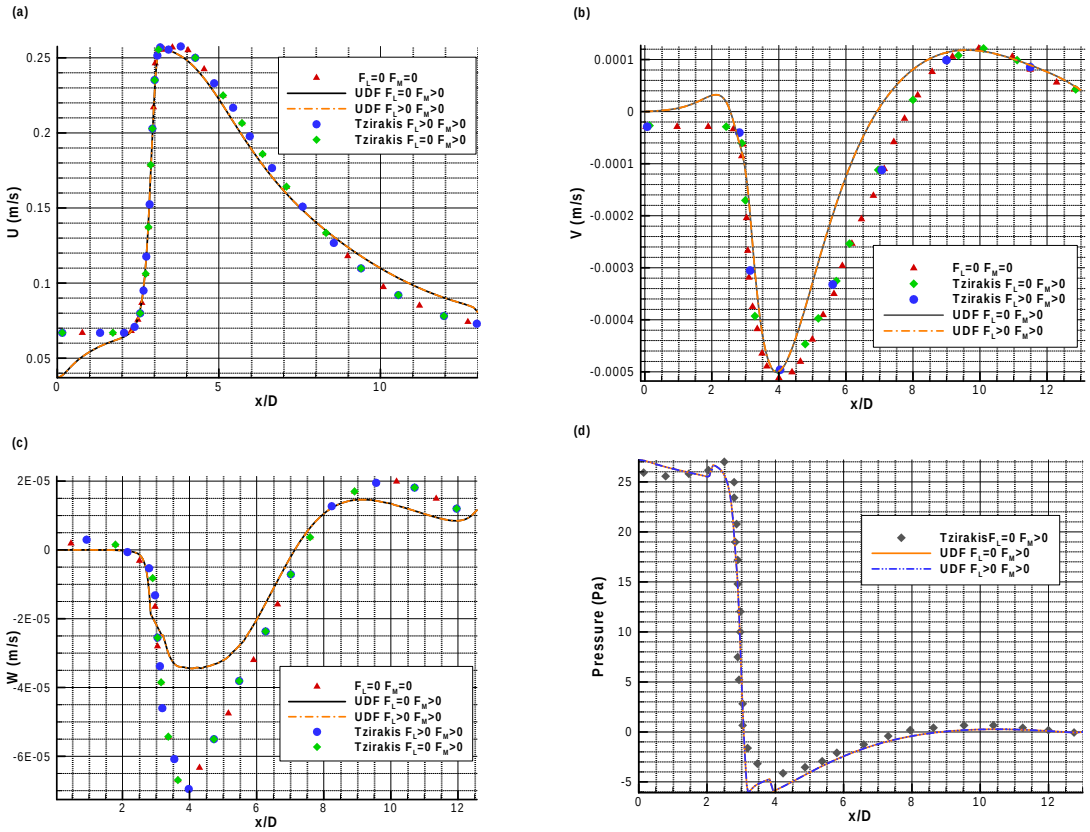

Figure 4.9: Pressure (d), and velocity profiles (a-b-c) comparisons along the symmetry axis for the irrotational magnetic field case.

Additionally, Figure 4.9 on page 61 confirms the fact that the irrotational magnetic field does not affect significantly the velocity field on the symmetry axis, in full agreement with what Tzirakis et al. have observed and what is grasped looking at Figure 4.6 on page 58.

Finally, the throat constriction effect can be highlighted again through velocity and pressure profiles. At x = 3D, where the throat is located, the flow acceleration becomes evident, in particular observing x-velocity and pressure which have opposite behaviours.

In conclusion, the FLUENT solver combined with the UDF, has successfully modelled all the tendencies and expected flow behaviours, and has provided results in high agreement

with the [1] ones. Therefore, the validity of the UDF, for this irrotational case, can be considered assessed.

4.2.2.3 The Rotational Magnetic Field ([1] Case 3)

The third step in the validation process involves the rotational magnetic field (3.49). Similarly to the previous section, here the validity and the effectiveness of the UDF to properly modify the flow equations, adding the rotational magnetic field source terms, is proven: results are provided again both in terms of velocity and pressure profiles along the symmetry axis and contours on xy-plane at z = 0. Comparisons have been performed with Tzirakis et al. numerical results [1].
The set-up presented in 3.4.2.1 is followed, and similarly to the irrotational case, the magnetic field is located at $x_i = 3.0D$ and $y_i = -0.5D$ in order to obtain approximately $|B(x_0, y_0)| = 4T$ where $x_0 = 2.8D$ and $y_0 = -0.3D$, as Figure 4.10 on page 62 clearly shows. In this case the field magnitude is expressed by:

$$|B(x,y)| = \frac{C}{r^4}. \tag{4.2}$$

where $r = \sqrt{(x-x_i)^2 + (y-y_i)^2 + (z-z_i)^2}$; the magnetic field is initialized and stored through the UDM.

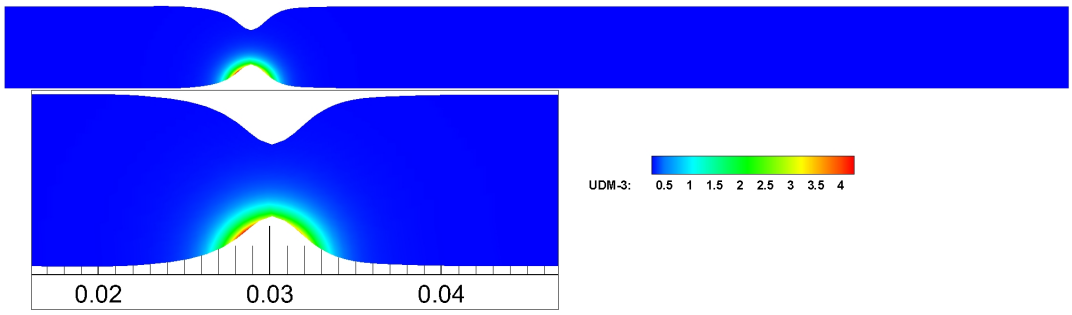

Figure 4.10: The rotational magnetic field contours at z = 0 tube cross section.

According to what has been found by Tzirakis et al. in their studies [1], this kind of magnetic field should largely perturb the blood flow in the tube: as it can be noticed from (3.31), (3.32), (3.33) and (3.49), the magnetization force turns to have not only a rotational character, but it is also characterized by strong spatial gradients that act on the flow, altering its path Figure 4.11 on page 63 (left-b).

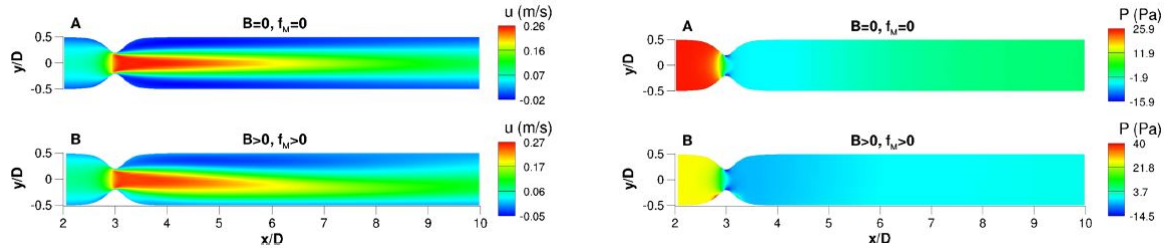

Figure 4.11: Stream-wise velocity (left) and pressure (right) results obtained by Tzirakis et al. [1] simulations for the rotational magnetic field case. The contours are displayed one diameter upstream to four downstream the throat.

As it can be appreciated from Figure 4.11 on page 63, the rotational magnetic field affects also the magnitude of the flow variables: differently from the irritational case, here the streamwise velocity increases as well as the pressure which grows significantly around the throat zone. This behaviour can be explained considering that the magnetic field has virtually narrowed the tube downstream the stenosis, causing a strong deflection and simultaneously, decreasing the pressure.

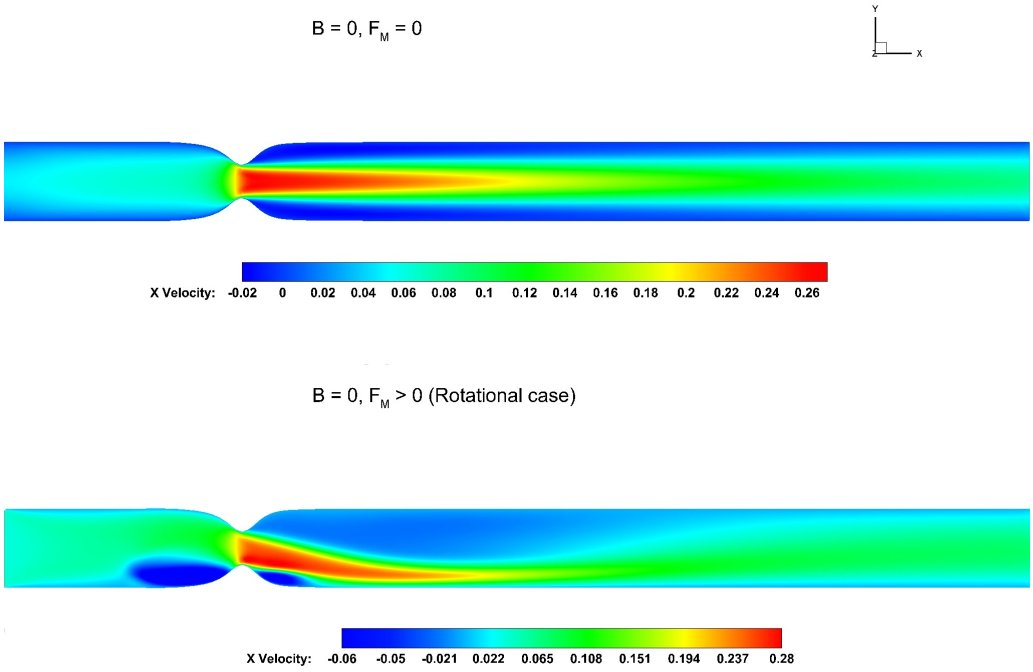

Figure 4.12: Stream-wise velocity field at z = 0. no forces (a), magnetization force (b). Results provided by the UDF.

Results obtained with the FLUENT and the UDF, are found not in a complete agreement with Tzirakis et al. ones. In fact, as it is possible to appreciate from Figure 4.12 on page 63, the magnetic field effect appears to be stronger if compared with Tzirakis et al. findings: the flow is strongly deflected and the recirculation zone located above the symmetry line is clearly wider and deeper than the one visible in Figure 4.11 on page 63. Moreover, exactly where the magnetic field reaches its maximum, a reverse flow zone has arisen, as well as another smaller one, immediately downstream the throat. These two recirculation areas are not present in [1].
Despite the differences from Tzirakis et al., the results obtained seemed to have a physical meaning and not to be wrong: they could be explained by the fact that, as previously mentioned, the rotational magnetic field is characterized by strong gradients, then, these gradients have a greater impact where the field reaches its maximum, bending the jet flow downstream the stenosis Figure 4.13 on page 64.

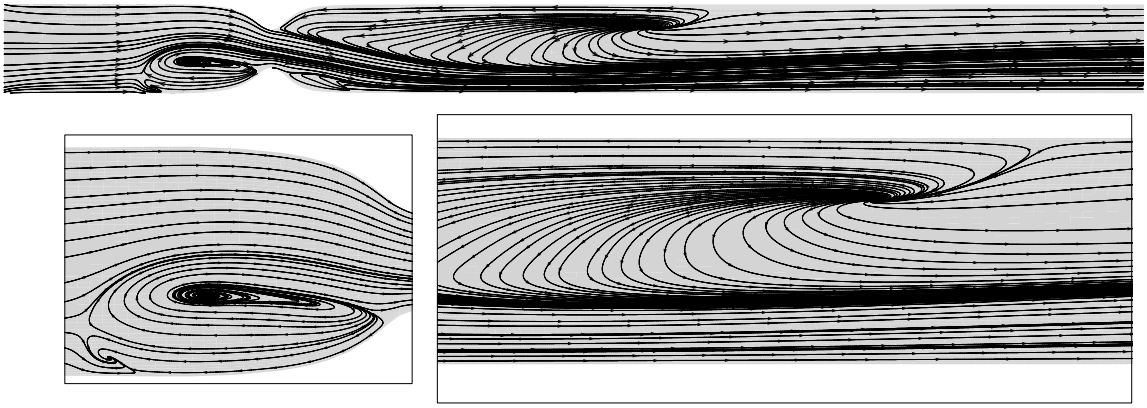

Figure 4.13: Stream-traces at z = 0 for the rotational magnetic field case obtained with the UDF.

If now the pressure field is considered, a better agreement with [1] can be found in terms of pattern: due to the strong recirculation upstream the stenosis, where the magnetic field magnitude is maximum, a localised pressure increase can be detected; however, this value turn to be 22.5% higher than what can be observed from Figure 4.11 on page 63 for Tzirakis et al. results.
On the other hand, immediately downstream the throat, pressure field has been found to behave similarly to Tzirakis et al. one: the high flow velocity causes a decrease in pressure larger than if the magnetic field is absent.

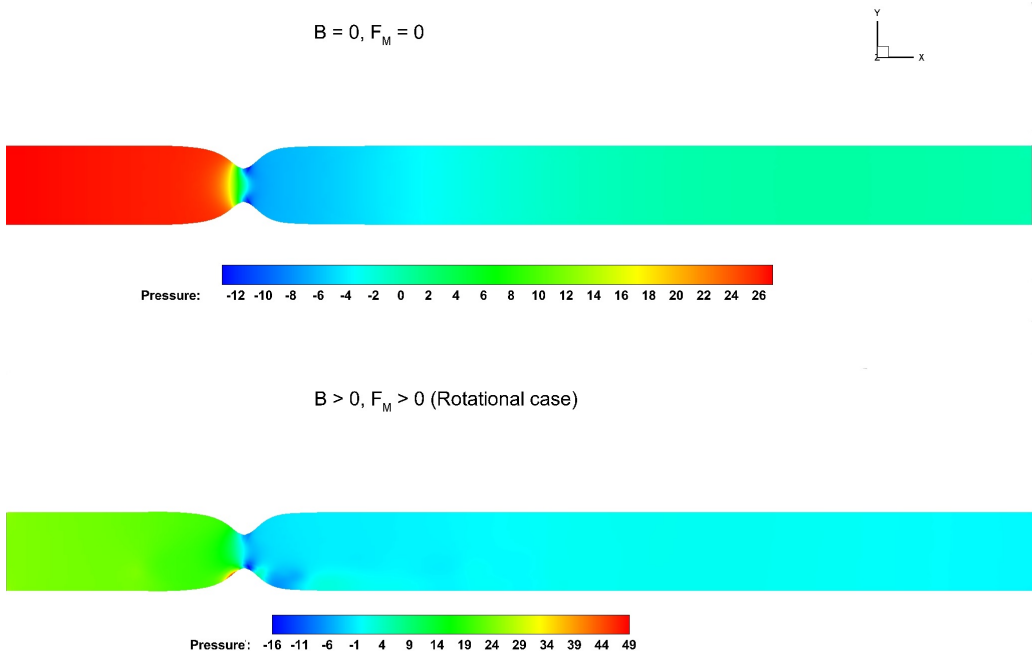

Figure 4.14: Pressure field at z = 0; no forces (a), magnetization force (b). Results provided by the UDF.

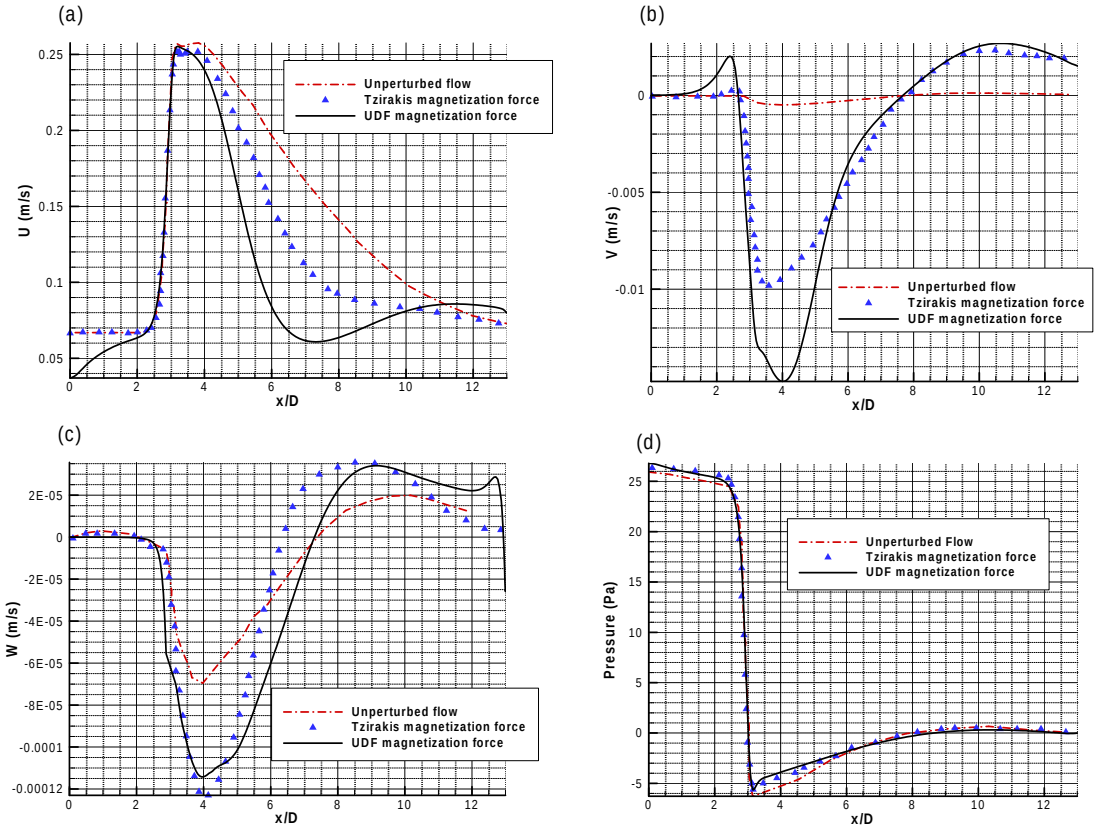

Figure 4.15: Pressure (d), and velocity profiles (a-b-c): comparisons along the symmetry axis for the rotational magnetic field case.

Finally, in order to completely assess the validity and the effectiveness of the UDF, the velocity and pressure profiles should be considered. Figure 4.15 on page 66 shows the comparisons between the unperturbed flow, the flow influenced by the rotational magnetic field computed by Tzirakis et al. and the one computed by FLUENT with the UDF features activated. As can be seen from Figure 4.15 on page 66 (a), the FLUENT results for the x-velocity show a slight discrepancy from Tzirakis et al. one: in the latter case, the velocity decrease after the throat appears to be smoother, while in the former, velocity decreases steeper. Nevertheless, the trend is well captured. Considering the y-velocity component Figure 4.15 on page 66 (b), the FLUENT result matches with an acceptable accuracy the [1] one, with the exception of the local minimum value, where a maximum deviation can be found to be around 33%.
From a physical point of view, it is interesting to observe how the rotational field acts on the flow, causing a huge increase in y-velocity (more than two orders of magnitude) compared with the unperturbed flow and confirming the fully three-dimensional character of the magnetic effects. The highest agreement between Tzirakis et al. results and the

FLUENT ones can be identified in the z-velocity Figure 4.15 on page 66 (c) and pressure Figure 4.15 on page 66 (d) profiles, where both the trends and the magnitudes match, especially for the latter one.

Summarizing the results obtained and taking into account the comparisons preformed, the UDF performance for the rotational magnetic field case turned out to be satisfactory despite some discrepancies in terms of flow physics, which, however are considered as errors but seems to have a reliable and physical explanation. As concluding remark, the UDF validation process seems to be successfully accoplished and the source codes can be used hereafter for different purposes and problems.

4.2.2.4 The Comparison between Slip and non-Slip Boundary Conditions

As introduced in 3.2.3, in order to perform a proper problem analysis and modelling, due to the quasi-micro-scale domains considered, the effect of slip boundary conditions should be studied for the 3-D tube with the stenosis.
The smallest dimension of the domain is reached at the throat, where the diameter is narrowed to $4 \cdot 10^{-3}\,m$. Computing the Knudsen number using (2.2) and the mean free path as defined in 3.2.3, a value of $Kn = 7.485 \cdot 10^{-8}$ is obtained: it should indicate that the flow regime belongs to the continuum hypotesis, where the N-S equations are fully valid and the non-slip boundary condition can be accepted [26].
Nevertheless, investigate numerically the flow behaviour in presence of the slip boundary condition and compare the results with the no-slip case, is considered necessary and useful. The rotational magnetic field case is investigated for this purpose.

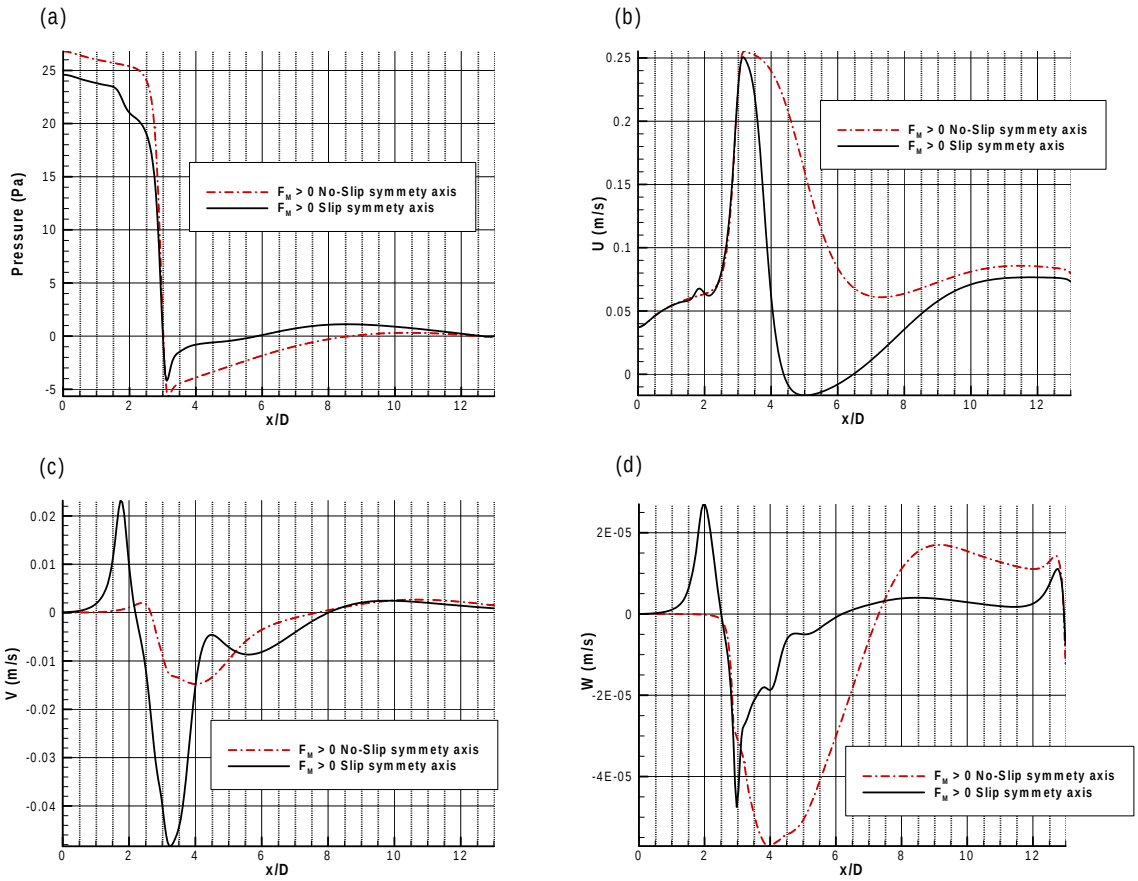

Figure 4.16: Comparisons between pressure (a) and velocity components (b-c-d) along the symmetry axis, obtained with and without the slip boundary condition in presence of the rotational magnetic field.

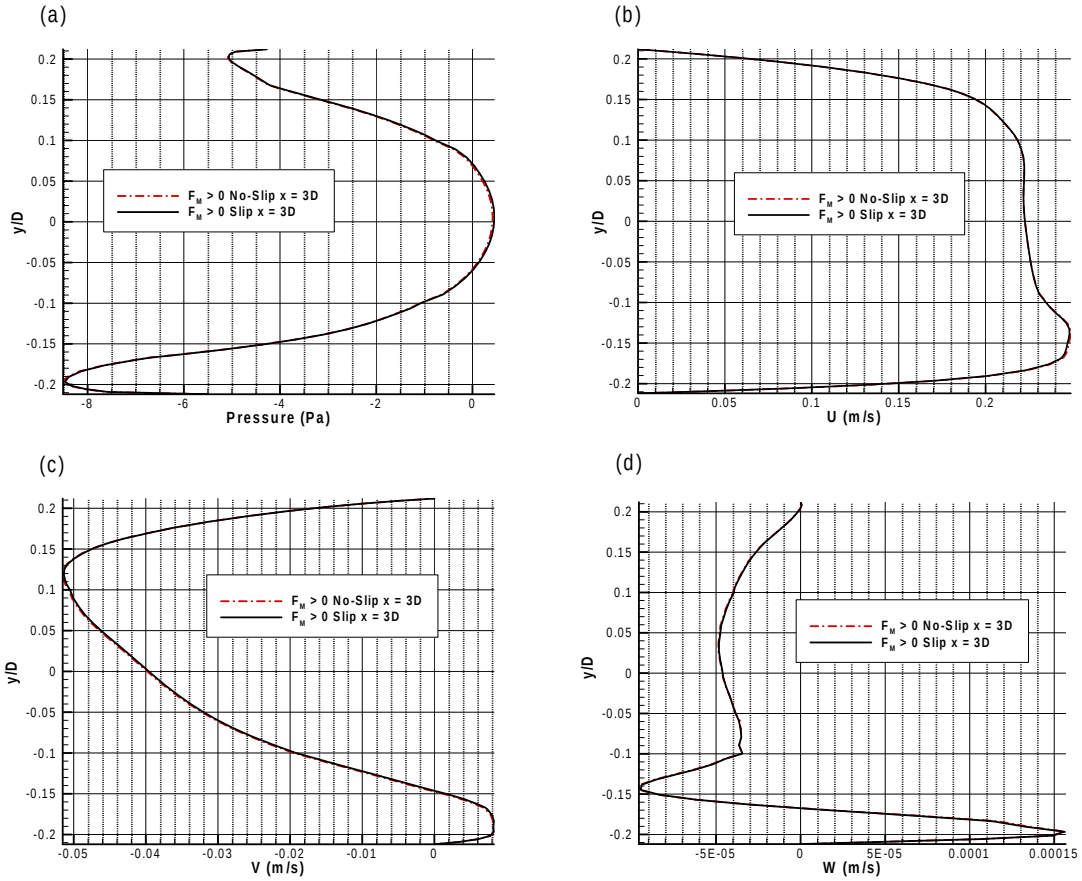

Figure 4.17: Comparisons between pressure (a) and velocity components (b-c-d) at x = 0.03 (3D), obtained with and without the slip boundary condition in presence of the rotational magnetic field.

Interesting and unexpected results have been obtained from the simulations and the comparisons with the non-slip case, how Figure 4.16 on page 68 shows. The presence of slip boundary condition (3.69) significantly affects the flow along the symmetry axis for whom, all the variables are perturbed and shows a slightly oscillatory behaviour although a convergence of 10^{-9} has been reached. The pressure jump on Figure 4.16 on page 68 (a) is reduced, while the x-velocity component faces a steeper decrease than in the non-slip case.

The major differences between slip and non-slip can be appreciated for y- and z-velocity profiles in Figure 4.16 on page 68 (c-d). Both profiles are largely perturbed: the y-velocity grows in magnitude and shows considerable overshoots, whereas z-velocity profile exhibits a pronounced oscillatory behaviour, with a large difference form the non-slip condition in correspondence of the throat, where the local minimum of magnitude is higher and the trend downstream the throat is steeper.

If now pressure and velocity profiles are analysed and compared with the non-slip case in correspondence of the throat (x = 0.03 m (3D)), the slip condition seems not to have any effects on the flow, as it possible to notice from Figure 4.17 on page 69. All the profiles for the slip conditions perfectly match the ones obtained with the non-slip. This results turn to be in agreement with what has been stated at the beginning of this section: the very low Knudsen number characterizes the continuum regime where the slip condition is ineffective.
Results obtained for the symmetry axis appear to be in contrast to ones obtained at station x = 3D: these discrepancies could be caused by the UDF implementation, where strong approximations have been done considering for example water parameters instead of blood ones as simplification, or using a constant spacing for the slip velocity discretization. All of these small approximations could have combined and caused large perturbations. Moreover, some strange interaction between the magnetic field source terms and the slip conditions could had arisen within the solver. Due to these uncertainties and contradictory results, the slip condition effects need to be further studied in more detail. Due to these uncertainties they have been neglected for the following simulations and analyses, which is, by the way not an unacceptable apporximation.

4.3 The non-Newtonian Blood Flow through a 3-D Stenosed Circular Duct under the action of Rotational Localised Magnetic Field

Within the present section, results obtained for the non-Newtonian blood flow in the 3-D stenosed tube under the action of the rotational magnetic field are presented. The problem investigated by Tzirakis et al. [1] is, indeed, enhanced in terms of flow physics, considering the non-Newtonian rheology of blood; the wall, as well, are modelled with the same properties of human vessel tissue. Finally, the energy equation and the temperature, are also considered.
The flow is subject to the same rotational magnetic field presented in 3.1.3 and the magnetization force is taken into account through the UDF that has been validated in the previous sections. This particular problem deals with a quite complex flow physics in a fairly simple domain and can be considered as an intermediate step between a flow characterized by a simplified fluid model in the same relatively simple domain (Tzirakis et al. stenosed cylinder), and a complex scenario, where a more realistic fluid model is taken into account in a definitely more complex geometry (Aorta).

The differences between the Newtonian and the non-Newtonian blood flows, both perturbed by the magnetic field, are considered first: in both cases the flow regime is char-

acterized by a Re = 100, however, due to the different formulation of the non-Newtonian Reynolds number, the inlet flow velocity turned out to be higher than in the Newtonian case. Therefore, greater values for the velocity field are expected.

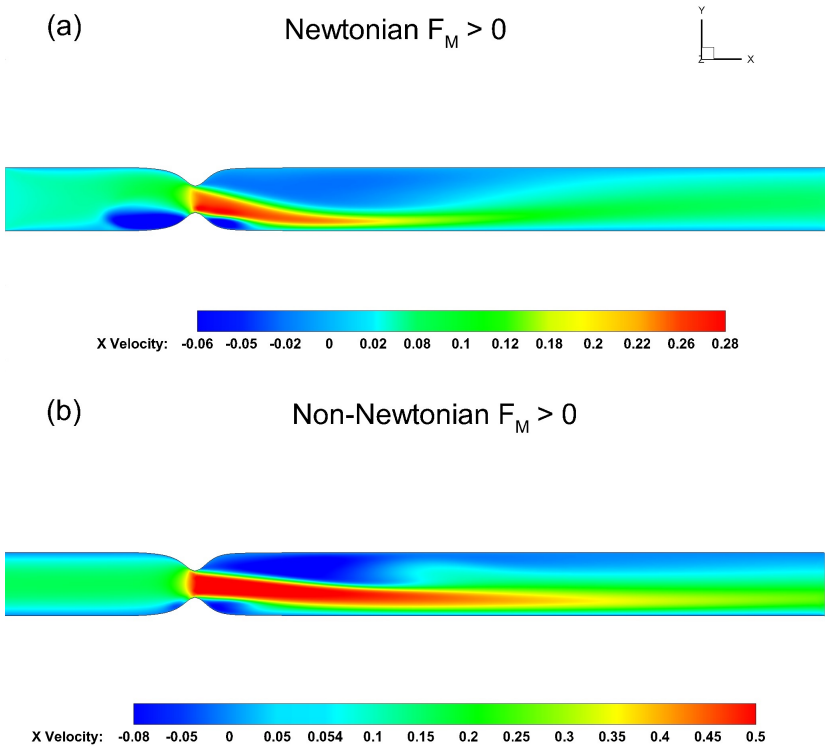

Figure 4.18: Stream-wise velocity (z = 0 plane) comparison between the Newtonian (a) and the non-Newtonian (b) blood flow perturbed by the rotational magnetic field.

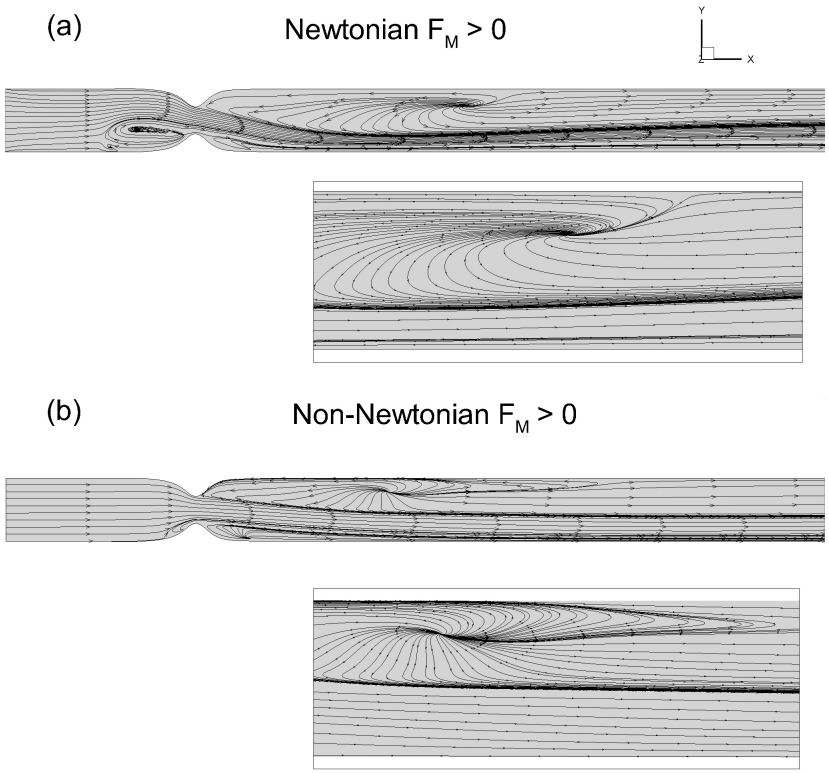

Figure 4.19: Stream-traces (z = 0 plane) comparison between the Newtonian (a) and the non-Newtonian (b) blood flow perturbed by the rotational magnetic field.

As it can be noticed from Figure 4.18 on page 71, the two flow fields are considerably different: except for the clear discrepancy in terms of maximum velocity magnitude (almost two times the Newtonian case), the recirculation structures appear sensibly different. In the non-Newtonian case, the flow is less deflected than in the Newtonian one, and also the upper recirculation region has a peculiar shape: while for the Newtonian blood flow it is smooth and well defined, for the non-Newtonian one, it has higher intensity with a vortex rising at the middle. Additionally, while in the Newtonian case the developed flow is quickly recovered after the reversed flow region, for the non-Newtonian case the recirculation extends far downstream, breaking down the flow symmetry even at the outlet. What has been just described, can be clearly appreciated from Figure 4.19 on page 72: the flow stream-traces are compared in the two cases and, zooming where the main recirculation arises, the differences in flow behaviour can be highlighted.
Moreover, observing the stenosis region, dissimilarities can be found also for the other two recirculation regions upstream: the recirculating flow, which in the Newtonian case fills a considerably wide zone before the throat where the magnetic field acts, is almost completely disappeared in the non-Newtonian one; whereas, the reversed flow zone on

the lower wall, downstream the throat remains almost unaltered.

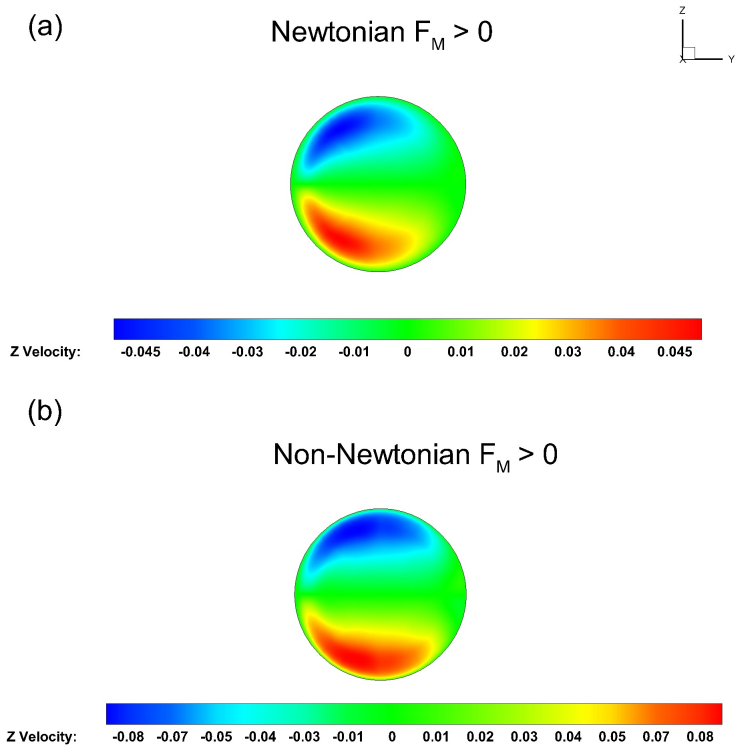

Figure 4.20: z-velocity (x = 0.03 plane) comparison between the Newtonian (a) and the non-Newtonian (b) blood flow perturbed by the the rotational magnetic field.

Slight differences can be also found investigating the z-velocity component in the centre of the stenosis, where the diameter reaches the smallest value. As it possible to appreciate from Figure 4.20 on page 73, both the reversed and the jet flow magnitudes are higher considering the non-Newtonian case; additionally, the two zones assume a more symmetric position with respect to the y-axis, than in the Newtonian case.

Proceeding in the analysis, in order to fully understand and investigate the differences between the Newtonian and the non-Newtonian flow subject to the rotational magnetic field, pressure, velocity and wall shear stresses profiles should be studied and compared.

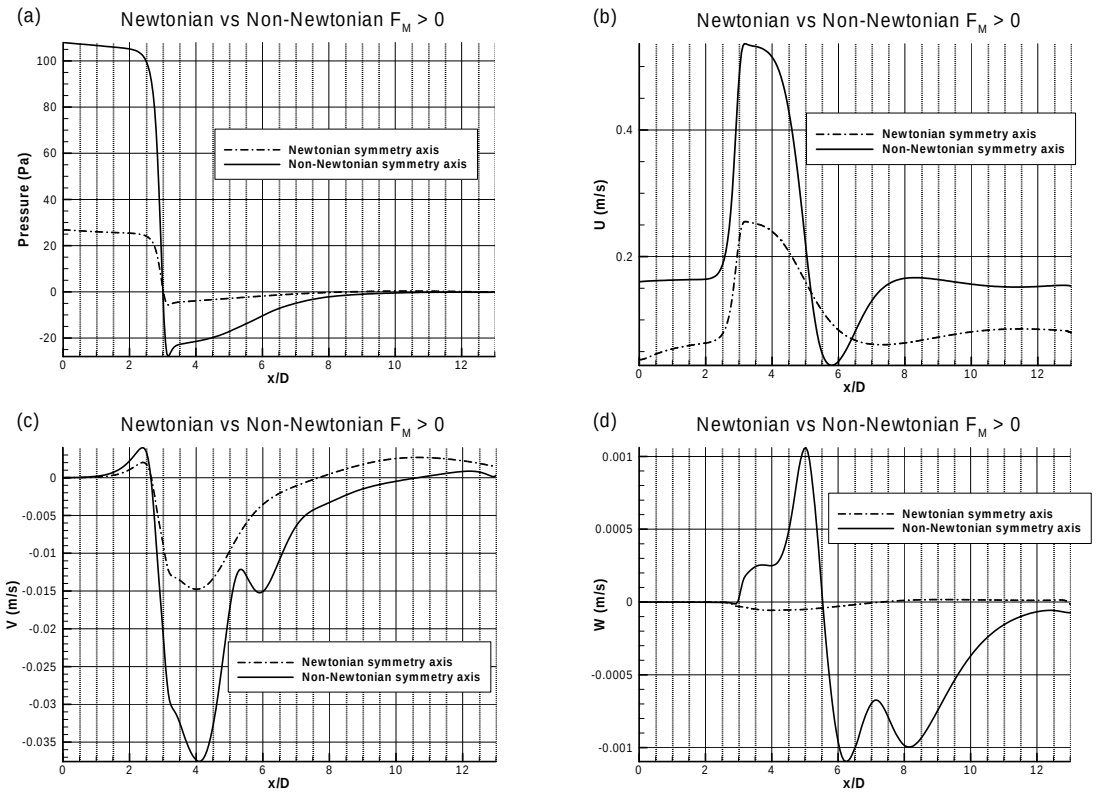

Figure 4.21: Comparison between pressure (a), x-velocity (b), y-velocity (c), z-velocity (d) for the Newtonian and the non-Newtonian blood flow along the symmetry axis under the action of the rotational magnetic field.

From Figure 4.21 on page 74, the discrepancy between the Newtonian and the non-Newtonian case can be appreciated: all the profiles are plotted along the symmetry axis where the tube length is normalized with respect to the inlet cylinder diameter. The difference in magnitude immediately appears evident in all the graphs: the higher flow velocity can be detected both looking at the x-velocity Figure 4.21 on page 74 (b) and at the huge pressure jump Figure 4.21 on page 74 (a) that occurs at x = 0.03 m (3D).
From the x-velocities comparison Figure 4.21 on page 74 (b), the recirculation region, located at x = 0.06 m (6D) and previously highlighted with the contours, can be identified: the flow is not reversed but the velocity is decreased to zero, similarly to a stagnation point; physically speaking, in both cases the magnetic field has completely broken down the flow symmetry.
If the y- and z-velocity components (Figure 4.21 on page 74 c-d) are considered, great gaps can be appreciated in terms of absolute magnitude: while the y-velocity trends for both the Newtonian and the non-Newtonian blood flow are similar, and there is only a big difference in terms of magnitude (133%), for the z-velocity huge discrepancies

are clearly visible both in terms of trend and magnitude. Moreover, differently from the Newtonian case, where the loss of velocity in z-direction occurs approximately at the throat location, in the non-Newtonian case, the faster and less perturbed flow causes a positive jump also in z-velocity, which follows the x-velocity tendency downstream, decreasing in correspondence of the stagnation point.

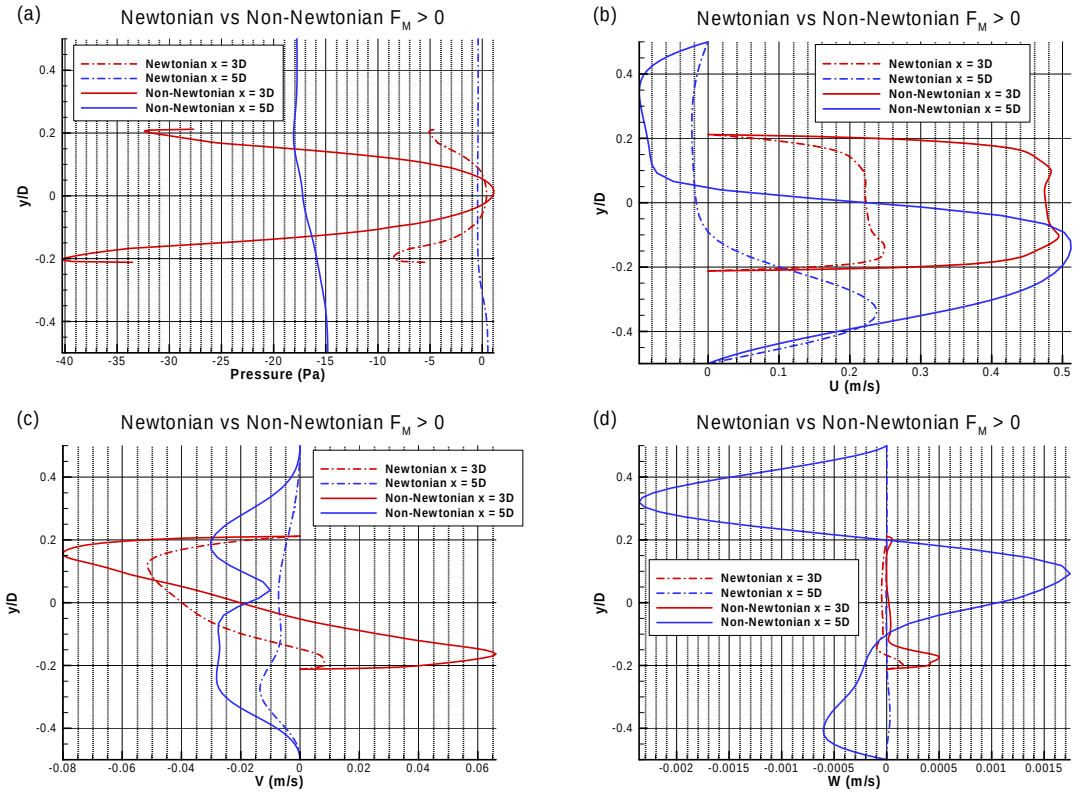

Figure 4.22: Comparison between pressure (a), x-velocity (b), y-velocity (c), z-velocity (d) for the Newtonian and the non-Newtonian blood flow at sections x = 0.03 m (3D) and x = 0.05 m (5D), under the action of the rotational magnetic field.

From Figure 4.22 on page 75 the flow evolution at different locations on the x-axis can be appreciated. The flow variables are extracted at x = 0.03 m (red, 3D) and x = 0.05 m (blue, 5D), for both cases.

First of all, the magnitude differences can be clearly noticed for all the profiles, especially considering the x-velocity Figure 4.22 on page 75 (b) where the recirculation region is evident: it appears wider and weaker in the Newtonian case than in the non-Newtonian one. The other two velocity components Figure 4.22 on page 75 (c-d) for the non-Newtonian case show highly perturbed profiles, completely different from the Newtonian biofluid flow.

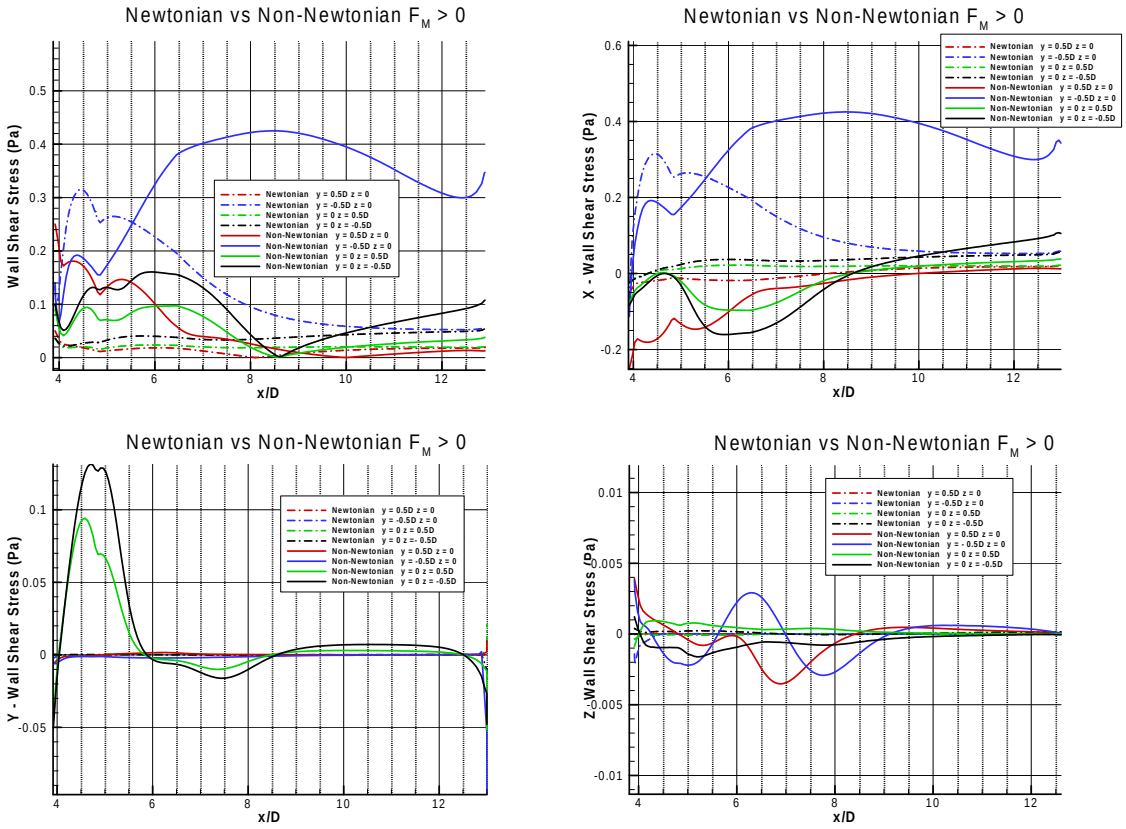

Figure 4.23: Comparison between Wall Shear Stresses (a), x-component (b), y-component (c), z-component (d) for the Newtonian blood flow and the Non-Newtonain blood flow, under the action of rotational magnetic field.

A final comparison between the Newtonian and the non-Newtonian flow considers the Wall Shear Stresses (WSS) and their components along the spatial directions, as it is shown by Figure 4.23 on page 76.

The WSS are evaluated along the x-axis, from x = 4D to the outlet, at four wall locations: y = 0.005 m - z = 0 m, y = -0.005 m - z = 0 m, y = 0 m - z = 0.005 and y = 0 m - z = -0.005. Dash-dotted lines are used for the Newtonian results, while solid ones identifies the non-Newtonian.

The most evident conclusion than can be drawn studying all the plots in Figure 4.23 on page 76, is that the magnetic field dramatically brakes the flow symmetry: profiles at y = 0.005 m - z = 0 m and y = -0.005 m - z = 0 m appear to be clearly different and without any symmetric behaviour, as well as the ones at y = 0 m - z = 0.005 and y = 0 m - z = -0.005. Analysing the global WSS Figure 4.23 on page 76 (a), the jet deflection can be identified where the WSS at y = -0.005 m - z = 0 m reaches its local maximum (blue solid line): the flow, indeed, is pushed on the lower part of the tube causing a rise of shear stress at the

wall; conversely, at y = 0.005 m - z = 0 m, WSS (red solid line) decrease. It is interesting to observe how the Newtonian fluid flow behaves differently: the WSS (red dash-dotted line) peak at y = 0.005 m - z = 0 m is reached very early downstream the stenosis, due to the jet greater deflection, and it is followed by a rapid decrease.
The X-WSS Figure 4.23 on page 76 (b) component, at y = -0.005 m - z = 0 m, confirms what has been observed for the global WSS. Studying its trend at y = 0.005 m - z = 0 m (red solid line), indeed, the upper reversed flow zone can be detected and the magnitude discrepancy between the Newtonian and the non-Newtonian case is also evident. The Y-WSS component Figure 4.23 on page 76 (c) shows high peaks at y = 0 m - z = 0.005 and y = 0 m - z = -0.005 m, which means that the flow expands at both sides on the ZX-symmetry plane, however, the profiles appear to be slightly different to each other, which means that the symmetry is broken even on that plane. Finally, the Z-WSS component Figure 4.23 on page 76 (d) shows oscillations caused by the flow deflection, again, stronger for the non-Newtonian case than for the Newtonian one; nevertheless, if the order of magnitude is compared with the other WSS components, it can be observed that the Z-WSS has a minor impact and the perturbations along the z-direction are almost negligible.
The effect of the magnetic field on the non-Newtonian blood flow is now investigated.

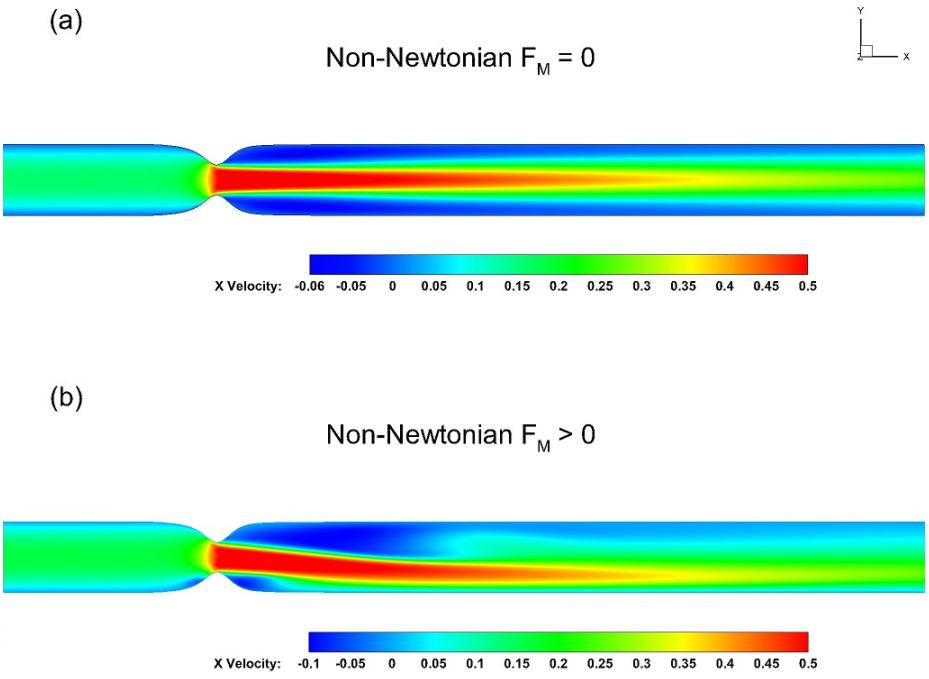

Figure 4.24: Stream-wise velocity (z = 0 plane) comparison for the non-Newtonian blood between the unperturbed flow (a) and the magnetically perturbed flow (b).

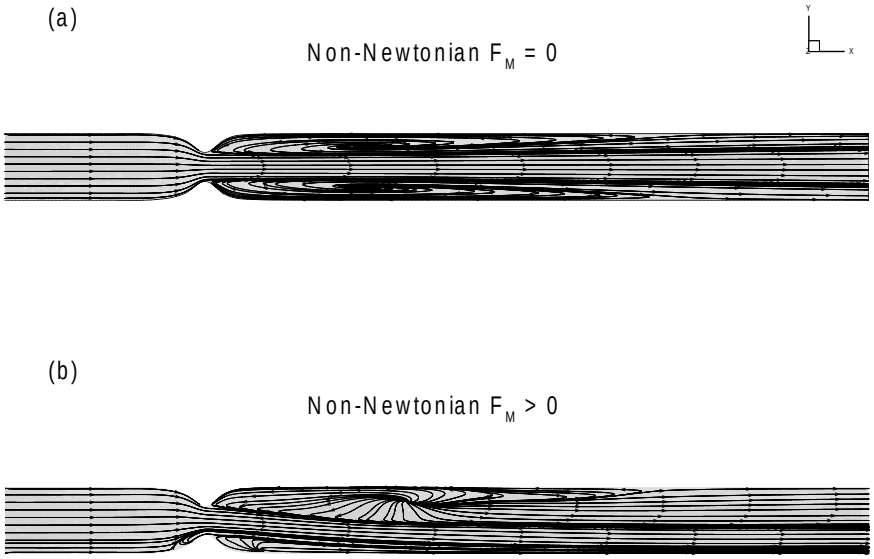

Figure 4.25: Stream-traces (z = 0 plane) comparison for the non-Newtonian blood between the unperturbed flow (a) and the magnetically perturbed flow (b).

From Figure 4.24 on page 77 and Figure 4.25 on page 78, the non-Newtonian flow reaction to the rotational magnetic field can be qualitatively analysed. As previously observed, and similarly to what happened for the Newtonian case, the rotational magnetic field deflects downside the jet flow after the throat, enhancing the reversed flow zone. Figure 4.24 on page 77 gives a clearer idea about the impact of the rotational magnetic field on recirculation zones: the symmetry has been completely destroyed and the upper reverse flow region is extended downstream.

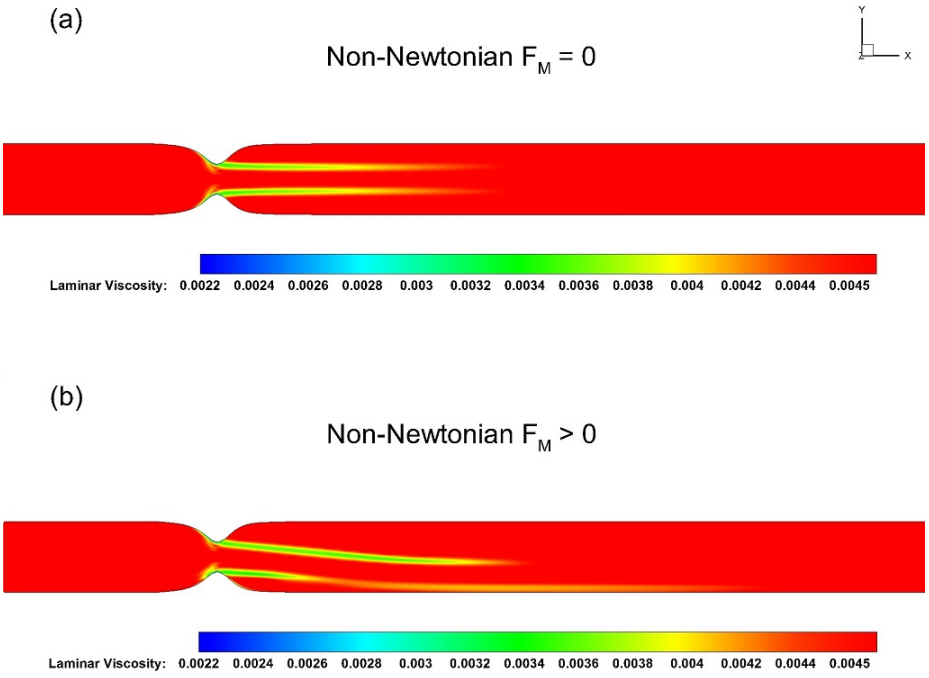

Figure 4.26: Laminar viscosity (z = 0 plane) comparison for the non-Newtonian blood between the unperturbed flow (a) and the magnetically perturbed flow (b).

Figure 4.26 on page 79 shows the laminar viscosity behaviour: unlikely the Newtonian case, here the viscosity changes according to the Power-Law model introduced and explained in 3.1.4. Due to the relationship between the viscosity and the shear rate tensor, the velocity variation perturbs the fluid viscosity field: as it possible to notice in Figure 4.26 on page 79 (b), the rotational magnetic field, deflecting the jet flow downstream the throat, disturbs also the viscosity, which is reduced due to the velocity gradient changing. Indeed, the results obtained, show a slight laminar viscosity reduction that extends closer to the lower wall where the flow is pushed by the magnetic force consequently increasing the strain rate.
Multiple comparisons between pressure, velocity and WSS components for perturbed and unperturbed flows give a quantitative idea about what happens.

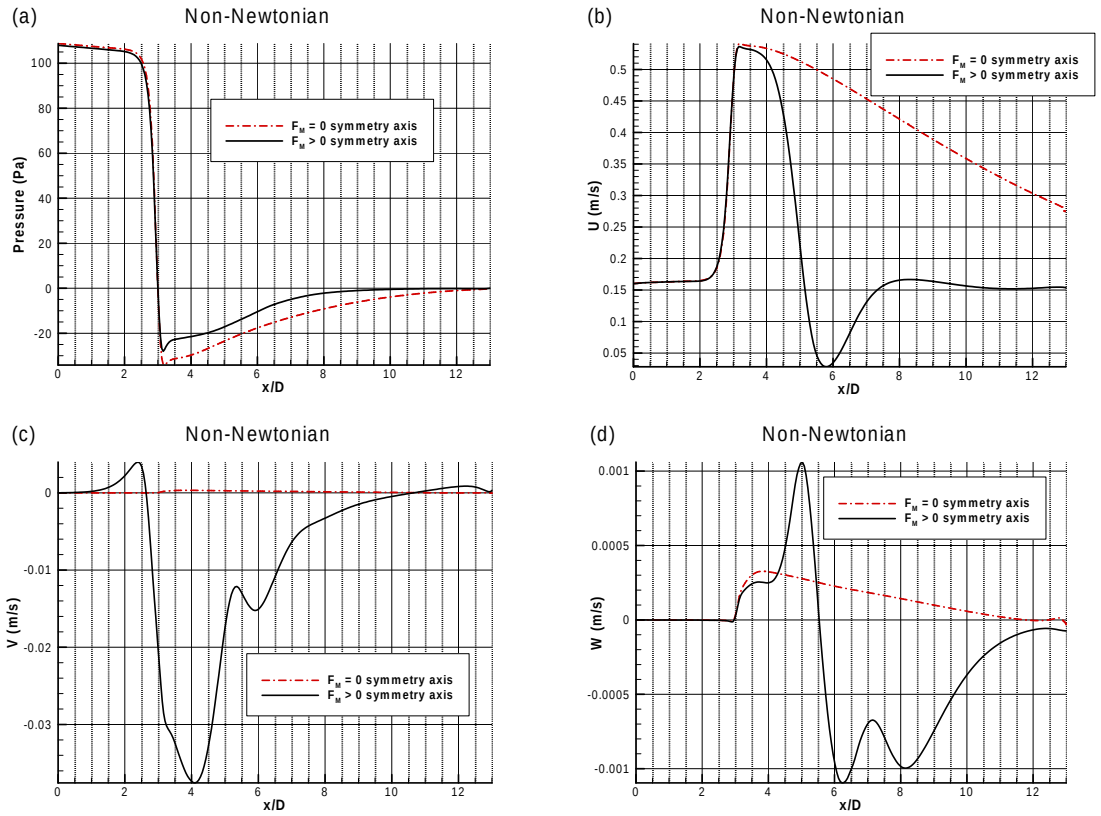

Figure 4.27: Pressure (a), x-velocity (b), y-velocity (c), z-velocity (d) comparison for the non-Newtonian blood between the unperturbed flow and the magnetically perturbed flow along the symmetry axis.

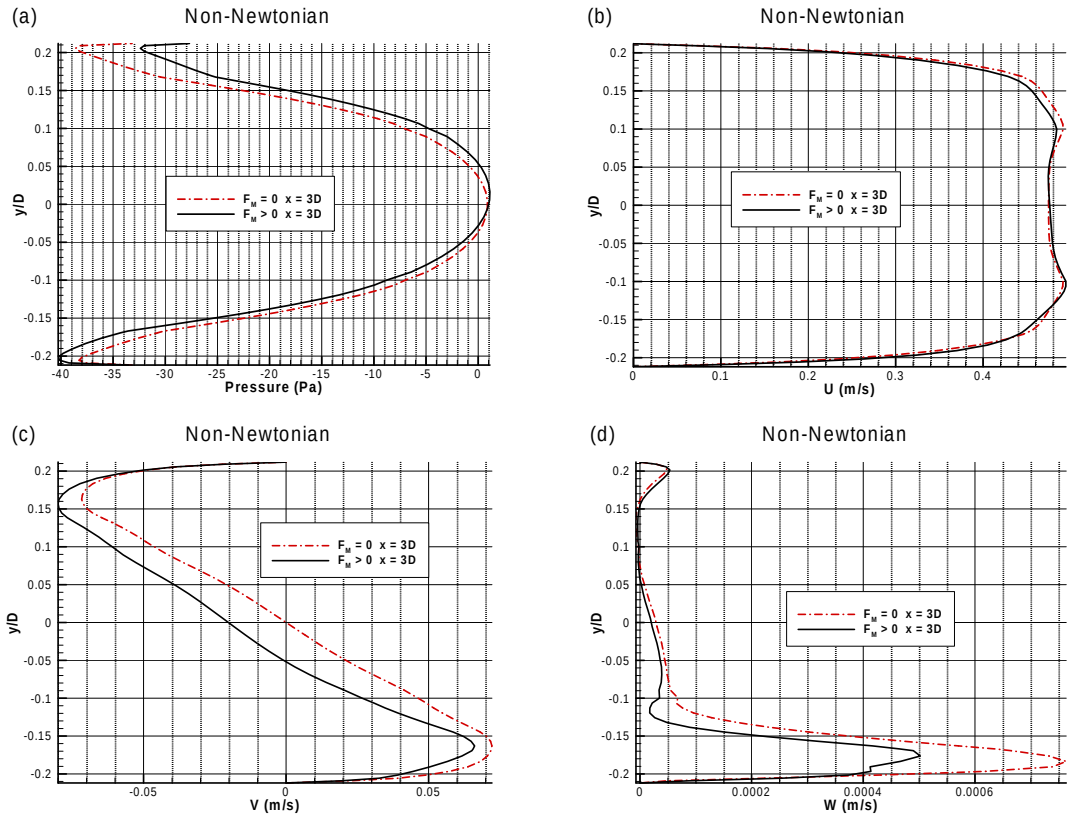

Figure 4.28: Pressure (a), x-velocity (b), y-velocity (c), z-velocity (d) comparison for the non-Newtonian blood between the unperturbed flow and the magnetically perturbed flow at section x = 0.03 m (3D).

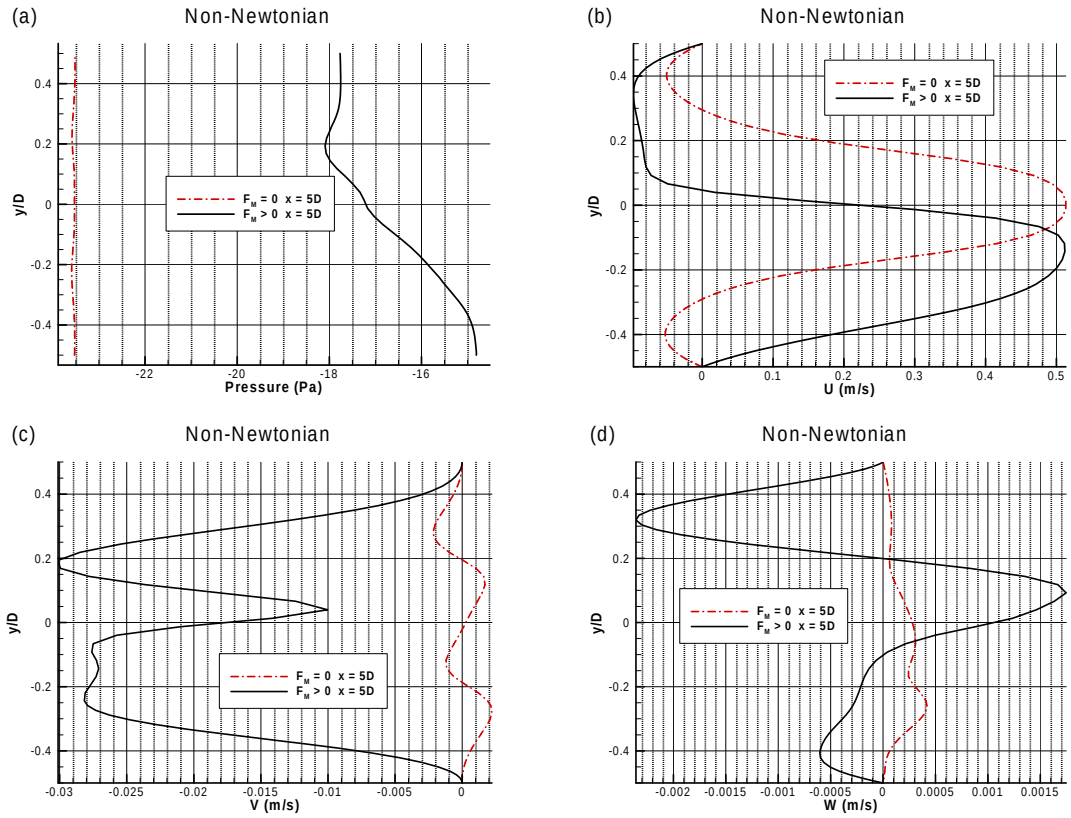

Figure 4.29: Pressure (a), x-velocity (b), y-velocity (c), z-velocity (d) comparison for the non-Newtonian blood between the unperturbed flow and the magnetically perturbed flow at section x = 0.05 m (5D).

Figure 4.27 on page 80 proposes results for pressure (a) and velocity components (b-c-d) along the symmetry axis. Similarly to what has been obtained for the Newtonian case, the rotational magnetization force causes a strong perturbation in the flow: both pressure and velocity are affected. The y- and the z-component face a massive increase, exhibiting considerable jumps at x = 0.06 m (6D), where the recirculation generates a stagnation point.

Figure 4.28 on page 81 and Figure 4.29 on page 82 provide informations about the flow development around the stenosis. In Figure 4.28 on page 81, profiles at the throat are compared: some discrepancies between perturbed and unperturbed flow start to appear; especially for the y- and the z-velocity components (c-d). Further downstream, at x = 0.05 m, in Figure 4.29 on page 82, the symmetry is definitely broken down, and all the variables show increased values: pressure (a) arises more than 25% with respect to the unperturbed condition; x-velocity (b) is affected in terms of maximum magnitude but faces an enhancement of the upper recirculation zone. On the contrary, the y-velocity Figure

4.29 on page 82 (c) experiences a gain of almost two orders of magnitude if compared with unaffected flow.
Last comparisons are made for the global WSS (a), and their components (b-c-d) in Figure 4.30 on page 84. Same layout of Figure 4.23 on page 76 is adopted also in Figure 4.30 on page 84 with the only difference that in the latter case, dash-dotted lines define the unperturbed condition, while the solid ones characterize the magnetized flow.
As one can notice, the WSS and the all components perfectly match each others at y = 0.005 m - z = 0 m, y = 0 m - z = 0.005 m (red and green dash-dotted), and at y = -0.005 m - z = 0 m, y = 0 m - z = -0.005 (blue and black dash-dotted) respectively, in the unperturbed case; however, after the application of the magnetization force, due to the symmetry break down, profiles detached assuming opposite trends, as it is clearly noticeable from Figure 4.30 on page 84 (a) and (b).
The same remarks expressed previously for the Newtonian to non-Newtonian Y- and Z-WSS comparisons, can be drawn also here: the non-Newtonian perturbed flow exhibits peaks at y = 0 m - z = 0.005 and y = 0 m - z = -0.005 m for the Y-WSS, whereas, the Z-WSS shows oscillations. However, the orders of magnitude are considerably lower with respect to the other components.

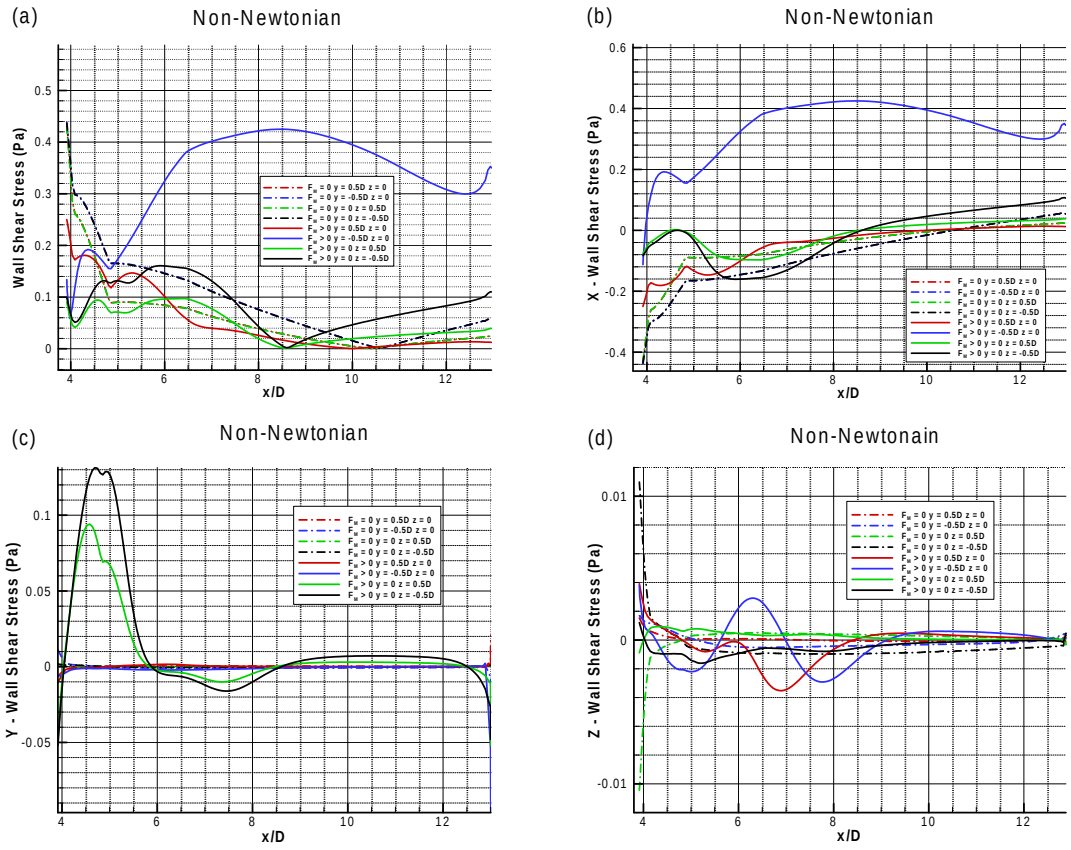

Figure 4.30: Wall Shear Stresses (a), x-component (b), y-component (c), z-component (d) comparison for the non-Newtonian blood between the unperturbed flow and the magnetically perturbed flow.

Summarizing the results obtained it can be inferred that:

1. If the same Reynolds number is considered for both the Newtonian and the non-Newtonian fluid flow, within the same domain, the main discrepancies are generated by the different inlet velocity: the non-Newtonian Re number, indeed, provides an higher value for the free-stream velocity than the Newtonian one. Despite this, comparisons still have meaning and validity;

2. The main differences in the flow physics between the Newtonian and the non-Newtonian case, regard the recirculation zones: in the latter case the jet flow appears to be less deflected than the former downstream the stenosis, but the reverse flow magnitude turns to be higher; a stagnation point also arises;

3. For both the Newtonian and the non-Newtonian flow, the rotational magnetic force breaks down the symmetry, which is no longer restored in the non-Newtonian case.

Finally, some observation of biomedical interest on the rotational magnetic field effects can be outlined considering the non-Newtonian blood flow within the stenosis. A localised rotational magnetic field application on a stenosed vessel, where the blood flows in a realistic regime (Re = $100 \sim U_\infty \approx 0.08\,m/s$), provokes important perturbations, which leads to some not negligible consequences:

- the enhancement of reverse flow regions can represent a dangerous scenario: due to the stagnation and slowing down, the blood is more keen to coagulate, reducing the vessel area and, therefore, increasing the stenosis. This circumstance could cause a vessel block, which must not occur;
- additionally, the perturbation generated considerably increases the wall shear stress, which could be an issue for the vessels sides, in the long term;
- on the other hand, the recirculation region could be positively effective when placed around a cancerous zone that needs to be treated with drug particles: the flow that delivers the particles is captured and deflected by the magnetic field, which is properly located close to the cancer; thus taking advantage of the flow slowing down, the drug can release its effect more efficaciously;
- finally, with the flow deflection, the blood viscosity can be reduced, therefore, a properly set-up magnetic field could have fluidize effects.

Taking into account these considerations, a localised rotational magnetic field application on a human body should be carefully studied in advanced, especially if the stenoses are present inside vessels, veins or arteries.

4.4 The Blood Flow through a Realistic 3-D Aorta Model subjected to a Localised Rotational Magnetic Field

In this section the results for the final simulations on blood flow through a realistic Aorta model are presented and discussed. Considering the structure of the present thesis, these last simulations aim to model the most realistic blood flow conditions.

4.4.1 The Grid Convergence Study

As it has been done for the 3-D stenosis model, preliminary simulations have to be performed in order to assess the grid convergence, and to be aware about the accuracy of the results.

For this particular case, neither experimental nor numerical data are available for a grid convergence study or for the comparisons; therefore, the Richardson extrapolation method is used to investigate the grid convergence.
The Richardson extrapolation allows to reconstruct an "exact solution", interpolating the numerical solutions obtained from two systematically refined meshes with grid spacing h_1 and h_2 respectively:

$$f_{ex} = f_2 + \frac{f_2 - f_1}{r_{12}^2 - 1}, \tag{4.3}$$

where $r_{12} = h_1/h_2$ is the refinement ratio between the coarse (h_1) and the refined (h_2) mesh, and f_1 and f_2, are the solutions for each mesh; then, this "exact" solution can be used to compute the errors and through them, evaluate the observed order of accuracy.
For the present work L_∞-norm and L_2-norm are computed: the first one allows to evaluate the maximum error, while the second norm has a more physical meaning.
Using the errors, the observed order of accuracy can be evaluated in the following way:

$$p = \frac{\ln\left(\frac{E_1}{E_2}\right)}{r_{12}}. \tag{4.4}$$

where E_1 and E_2 can be any type of errors for two consequentially refined meshes. Velocity results at z = 0.0834 m along the main branch are used to compute the errors.

	Coarse	**Medium**	**Fine**
N	516734	714829	964887
h	1.2663e-10	9.1539e-11	6.7918e-11

Table 4.1: Meshes parameters.

$\mathbf{r_{1/2} = 1.383}$	$L{-}\infty_c$	$L{-}\infty_m$	**p**
$L{-}\infty_u$	0.0056	0.0029	2
$L{-}\infty_v$	0.0092	0.048	2
$L{-}\infty_w$	0.0463	0.0242	2

Table 4.2: L_∞-norm errors and the expected order of accuracy for the coarse and the medium meshes.

$\mathbf{r_{2/3} = 1.348}$	$L{-}\infty_m$	$L{-}\infty_f$	**p**
$L{-}\infty_u$	0.0054	0.0030	2.5
$L{-}\infty_v$	0.0276	0.0152	2.5
$L{-}\infty_w$	0.1132	0.0623	2.5

Table 4.3: L_∞-norm errors and the expected order of accuracy for the medium and the fine meshes.

$\mathbf{r_{1/2} = 1.383}$	$L{-}2_c$	$L{-}2_m$	**p**
$L{-}2_u$	2.948e-7	1.31e-7	2
$L{-}2_v$	3.2e-7	1.42e-7	2
$L{-}2_w$	1.95e-6	8.68e-7	2

Table 4.4: L_2-norm errors and the expected order of accuracy for the coarse and the medium meshes.

$\mathbf{r_{2/3} = 1.348}$	$L{-}2_m$	$L{-}2_f$	**p**
$L{-}2_u$	2.77e-7	1.31e-7	2.5
$L{-}2_v$	1.15e-6	5.5e-7	2.5
$L{-}2_w$	5.31e-6	2.52e-6	2.5

Table 4.5: L_2-norm errors and the expected order of accuracy for the medium and the fine meshes.

With three meshes, as Table 4.1 on page 86 shows, only two observed order of accuracy can be computed.
Table 4.2 on page 86 to Table 4.5 on page 87 highlight how both the L_∞ and the L_2 errors between the coarse and the medium, and the medium and the fine meshes are similar for all the velocity components; despite this, with the fine mesh, 0.5 order of accuracy is gained if compared with the coarse-medium order. From this results one can infer that the grid convergence has not been reached, however for this final part of the thesis the medium mesh is considered due to the dramatically high computational time required by the fine mesh and the limited computational resources available. It is also believed that the 0.5 difference, in terms of observed orders of accuracy, would not provide too different results. Moreover, it should be remarked that this grid convergence study could be made more robust and reliable by considering more variables at different locations and not only velocity components at one location.

4.4.2 The Aorta Final Results

The main findings are organized in the following way:

- First of all, the Newtonian and the non-Newtonian models are compared in absence of any magnetic field in order to catch the differences and to evaluate the actual impact of the fluid viscosity models;
- Secondly, the effect of the rotational magnetic field on the non-Newtonian blood flow is investigated: the field is applied in three different locations, therefore different scenarios are analysed.

Pressure and velocity variables are considered at different sections for the comparisons and the evaluations:

1. along the z-axis on zy-plane;
2. at y = 0.18 m from the axis origin, on xz-plane;
3. at z = 0.023 m and z = 0.24 m from the origin, on xy-plane;

Additionally, along the z-axis at x = 0.19 m from the origin, values at three stations are evaluated and compared. Finally, outlet profiles of secondary capillaries are also considered.

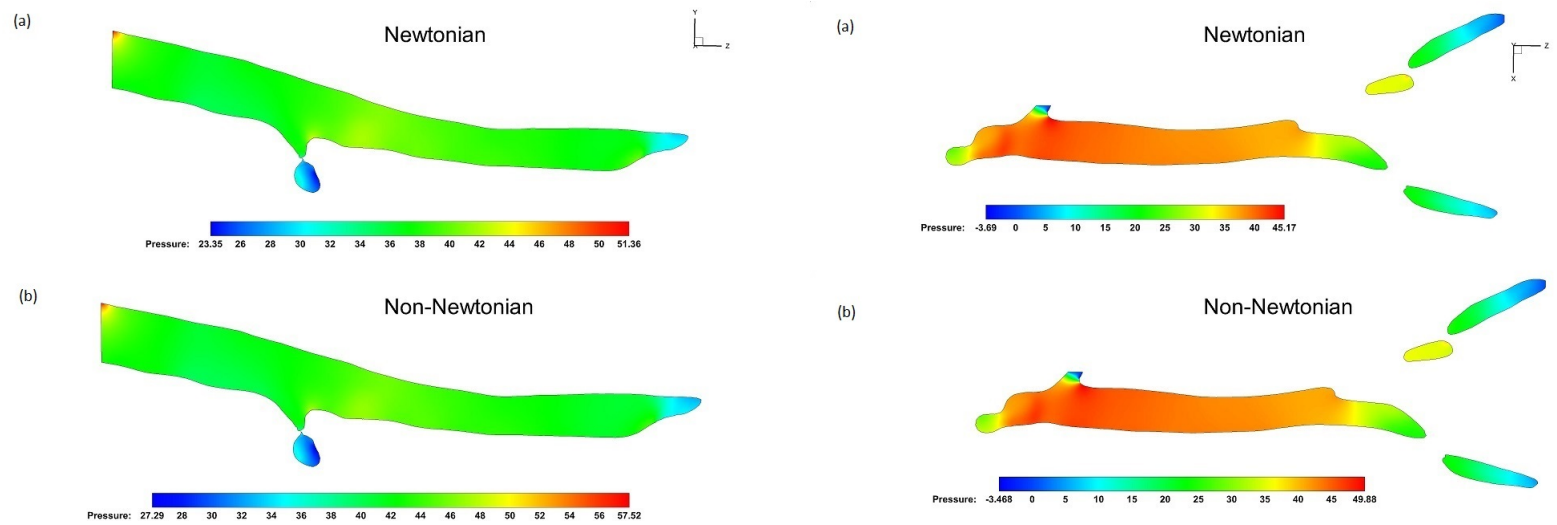

Figure 4.31: Comparisons between the Newtonian and the non-Newtonian pressure contours on yz-plane at x = 0.19 m (left), and on xz-plane at y = 0.18 m (right).

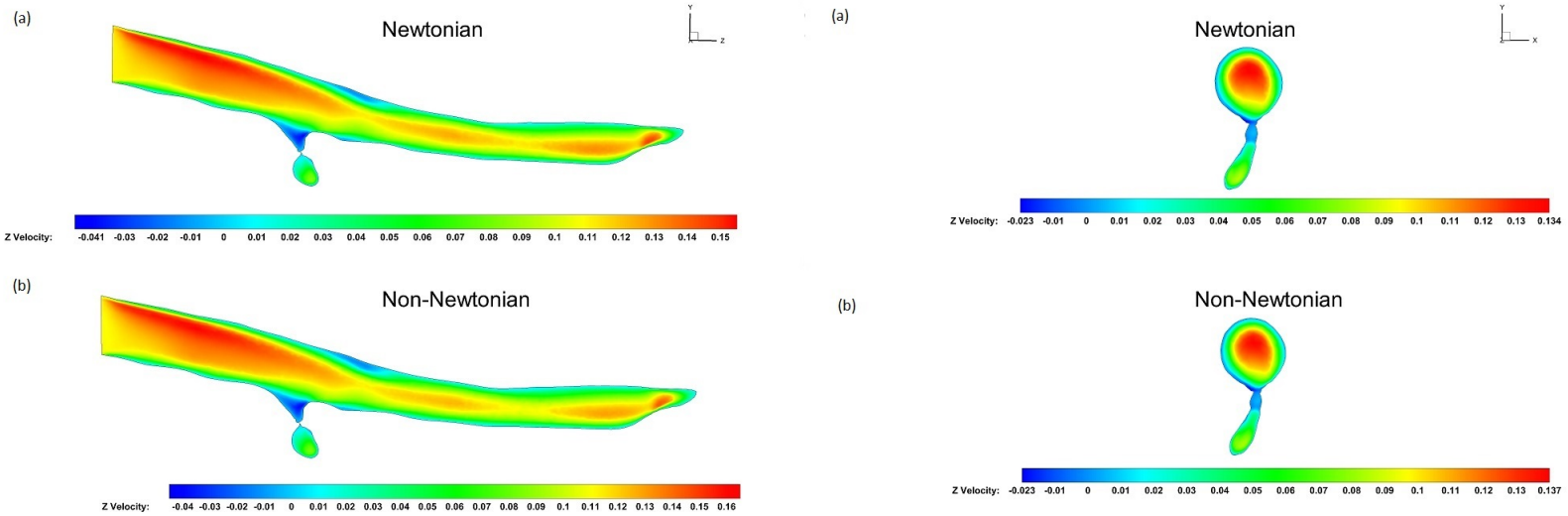

Figure 4.32: Comparisons between the Newtonian and the non-Newtonian z-velocity contours on yz-plane at x = 0.19 m (left), and on xy-plane at z = 0.119 m (right).

Considering in the first instance, the comparisons between the Newtonian and the non-Newtonian models effects on the flow, from Figure 4.31 on page 89 and Figure 4.32 on page 90 it can be noticed how the change between the two fluid models does not affect the flow pattern but only slightly the magnitude of the flow variables: the pressure for the non-Newtonian blood faces a maximum increase of barely 15% if compared with the Newtonian one, while the velocity increase is only around 1%.

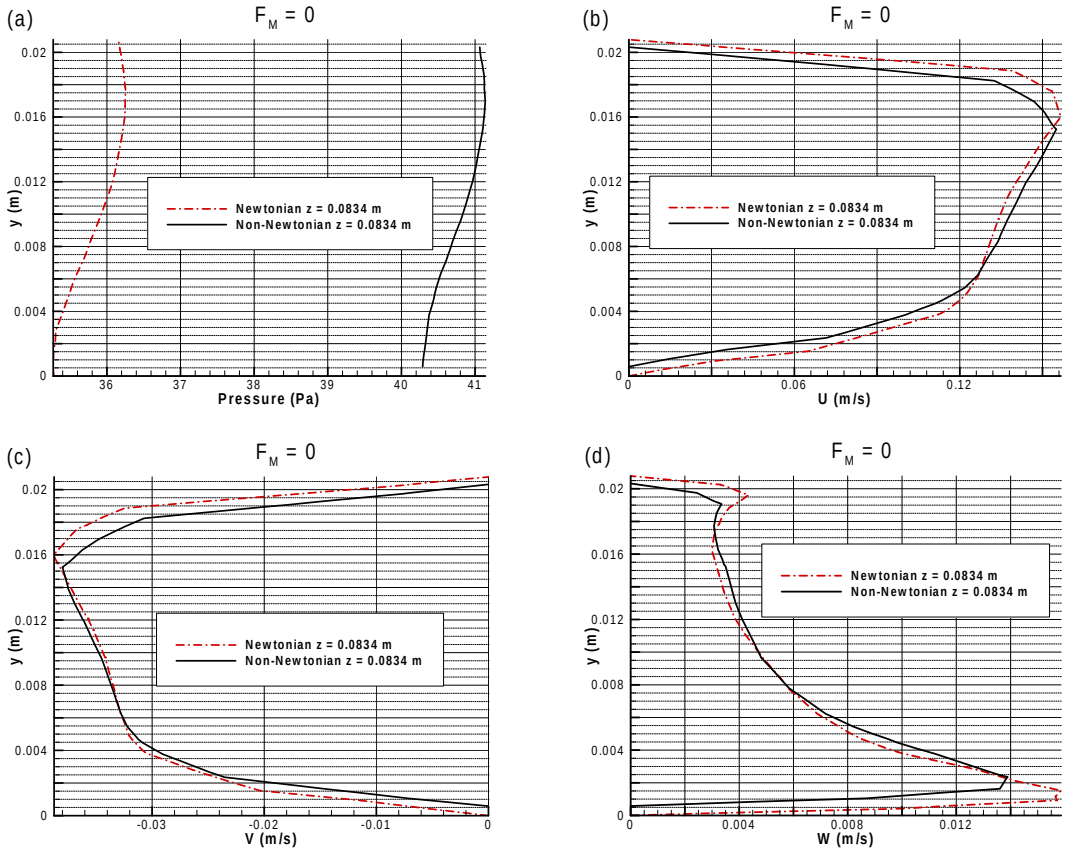

Figure 4.33: Comparisons between the Newtonian and the non-Newtonian effects on the pressure (a), x-velocity (b), y-velocity (c) and z-velocity (d) at z = 0.0834 m from the inlet and x = 0.19 m from the origin.

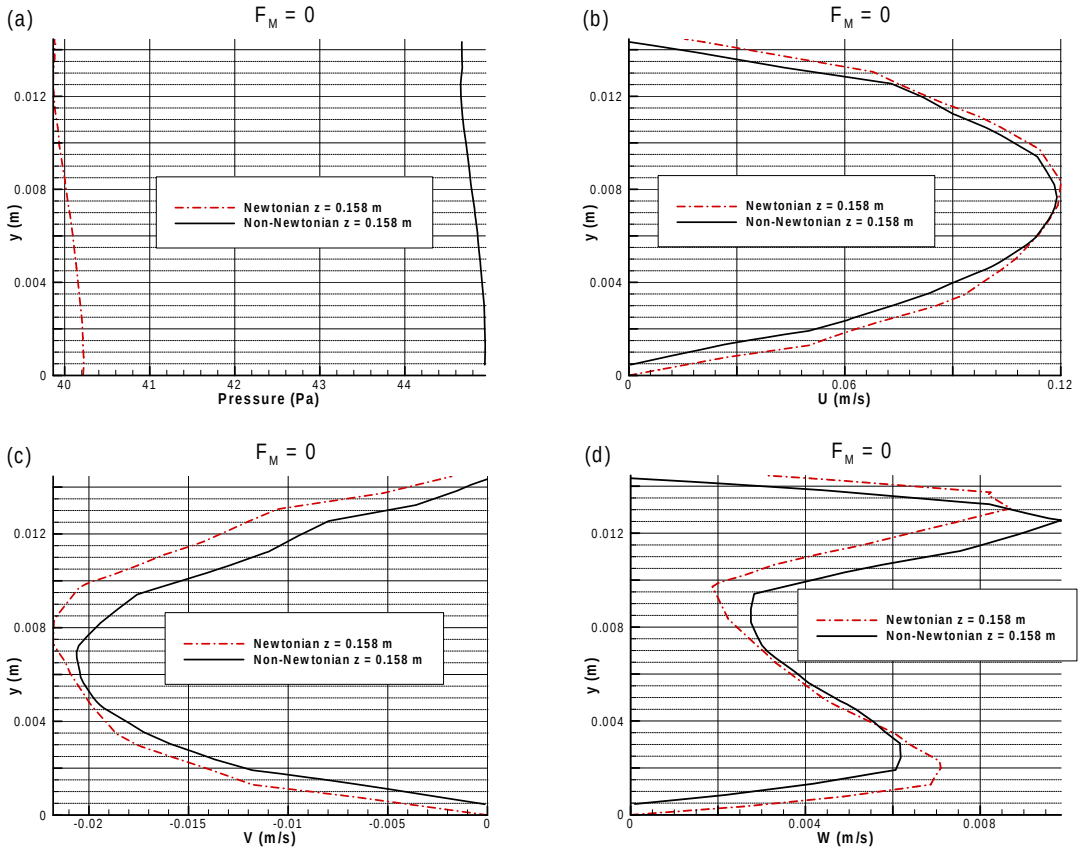

Figure 4.34: Comparisons between the Newtonian and the non-Newtonian effects on the pressure (a), x-velocity (b), y-velocity (c) and z-velocity (d) at z = 0.158 m from the inlet and x = 0.19 m from the origin.

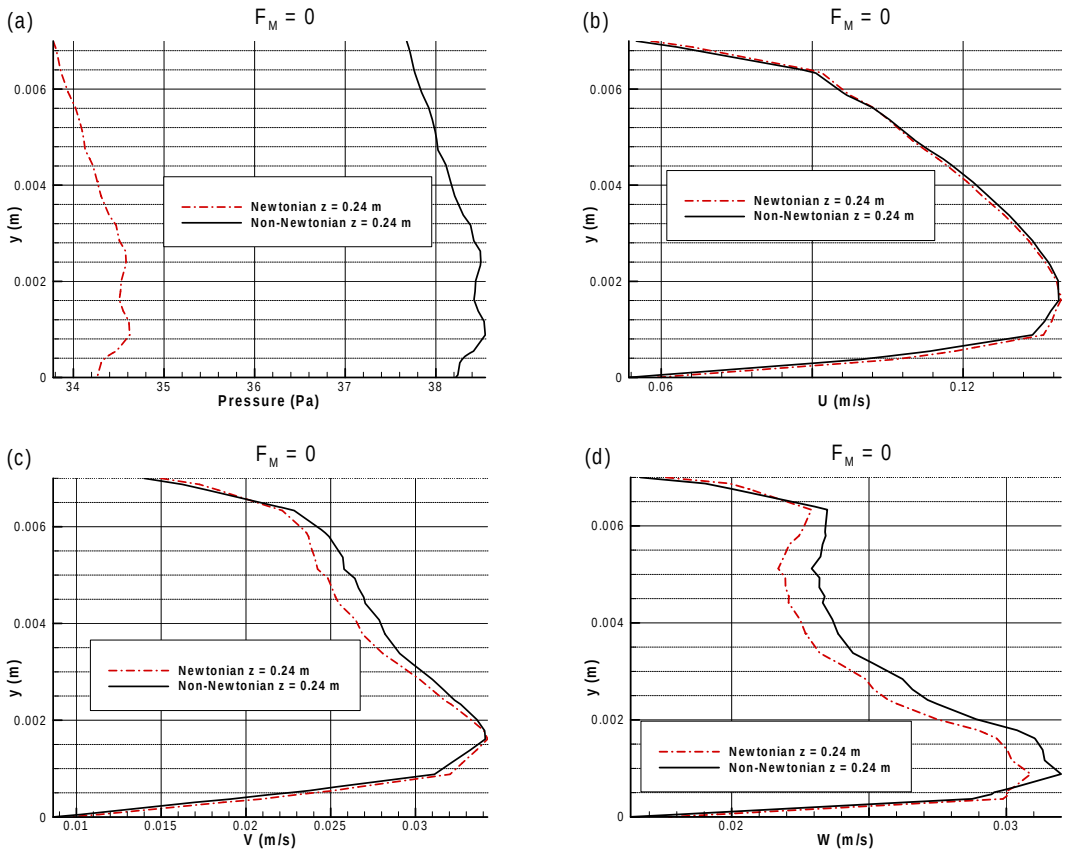

Figure 4.35: Comparisons between the Newtonian and the non-Newtonian effects on the pressure (a), x-velocity (b), y-velocity (c) and z-velocity (d) at z = 0.24 m from the inlet and x = 0.19 m from the origin.

Similarly, studying and comparing Figure 4.33 on page 91, Figure 4.34 on page 92 and Figure 4.35 on page 93, the actual non-Newtonian effect can be clearer caught: the pressure confirms to be the most affected variable by the fluid viscosity model; the velocity components, by the way, are less affected.
From a physical point of view, it is interesting to see how the flow develops along the z-directions, flowing from the inlet to the different outlets: profiles are asymmetric for all the components, reflecting the asymmetry of the domain. Additionally, from Figure 4.33 on page 91 and Figure 4.34 on page 92, negative values can be seen for y-velocity components, probably because the presence of the outlets 2 and 5, from where the blood flows out on the opposite direction of the positive y-axis. Should also be noted that the z-velocity is one order of magnitude greater than the other two. Focusing, indeed, on the outlet flows, the differences between Newtonian and non-Newtonian cases become more evident.

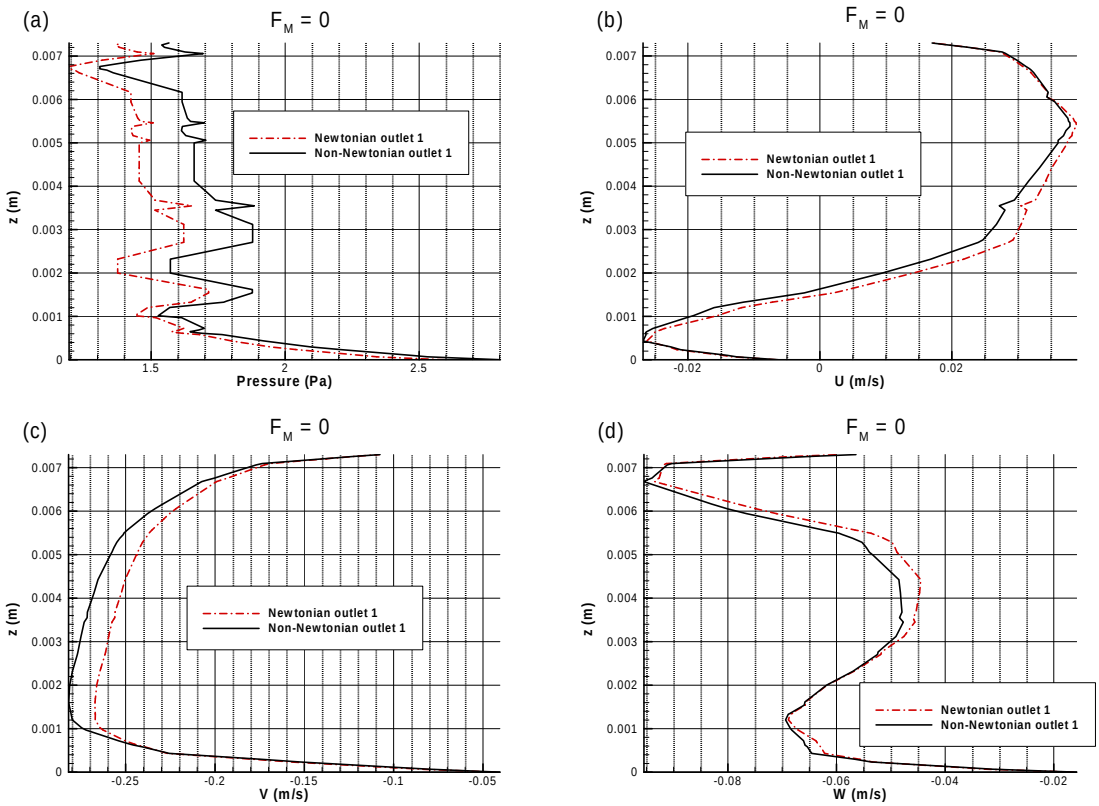

Figure 4.36: Comparisons between the Newtonian and the non-Newtonian effects on the pressure (a), x-velocity (b), y-velocity (c) and z-velocity (d) at the outlet 1.

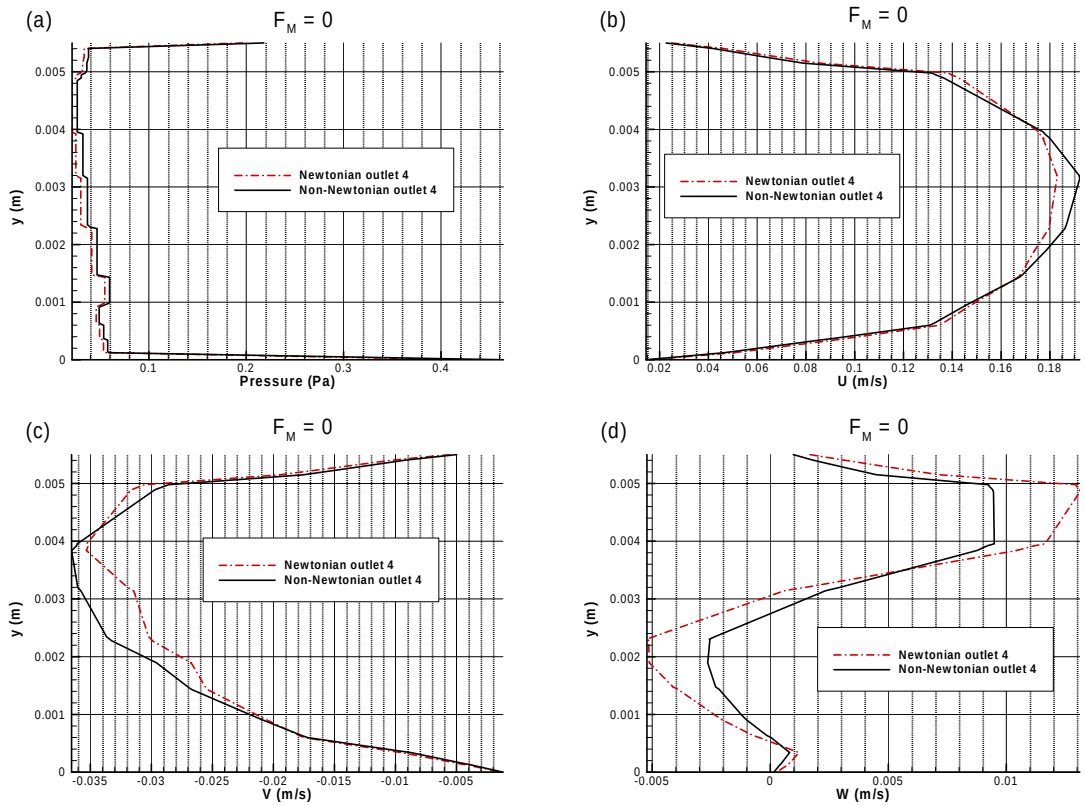

Figure 4.37: Comparisons between the Newtonian and the non-Newtonian effects on the pressure (a), x-velocity (b), y-velocity (c) and z-velocity (d) at the outlet 4.

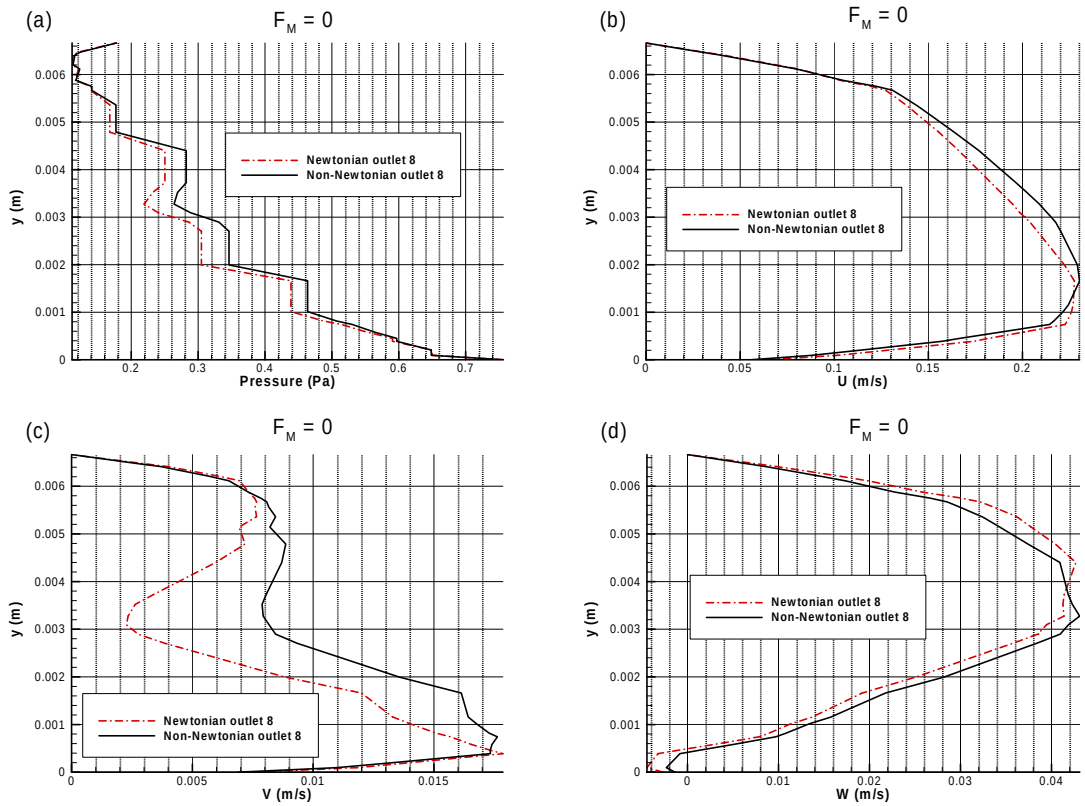

Figure 4.38: Comparisons between the Newtonian and the non-Newtonian effects on the pressure (a), x-velocity (b), y-velocity (c) and z-velocity (d) at the outlet 8.

Figure 4.36 on page 94, Figure 4.37 on page 95 and Figure 4.38 on page 96 illustrate the three outlets where the largest differences between the two blood models have been found. Comparing the range of the velocity components, it is possible to confirm that the discrepancy between the Newtonian and the non-Newtonian model grows when the flow is slower: comparing, for example, the y-velocity at outlet 1 Figure 4.36 on page 94 and at outlet 4 Figure 4.37 on page 95, it can be noticed that for the former, which reaches higher values, the differences between the two fluid models are smaller than for the latter, where the flow is ten times slower; z-velocity exhibits the same behaviour.
After having highlighted that the fluid viscosity model makes difference especially for slow flows, and the non-Newtonian Power-Law model is chosen to be more appropriate and realistic, the rotational magnetic field is introduced. Figure 4.39 on page 97 displays the three different locations where the field is placed.

	Location 1	Location 2	Location 3
X (m)	0.18	0.18	0.198
Y (m)	0.17	0.15	0.1508
Z (m)	0.08	0.18	0.24

Table 4.6: Spatial coordinates of the three magnetic field locations.

Coordinates provided in Table 4.6 on page 97 are chosen in order to obtain a maximum magnetic field magnitude of 4 Tesla, which is still tolerable by the human body.

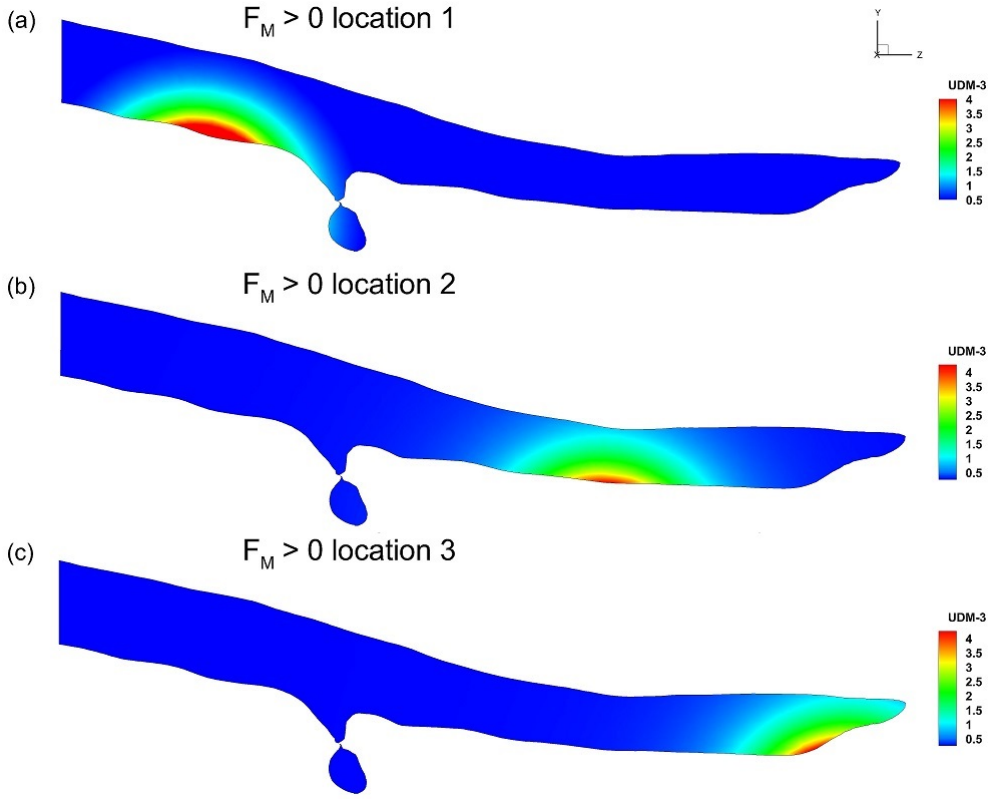

Figure 4.39: The three different location for the rotational magnetic field on yz-plane at x = 0.19 m from the origin.

Figure 4.40 on page 98, shows how the flow subjected to a rotational magnetic field located at different stations behaves: pressure field is altered in terms of magnitude more when the field is located closer to the inlet (location 1); only small differences can be noticed for the minimum, which slightly grows.

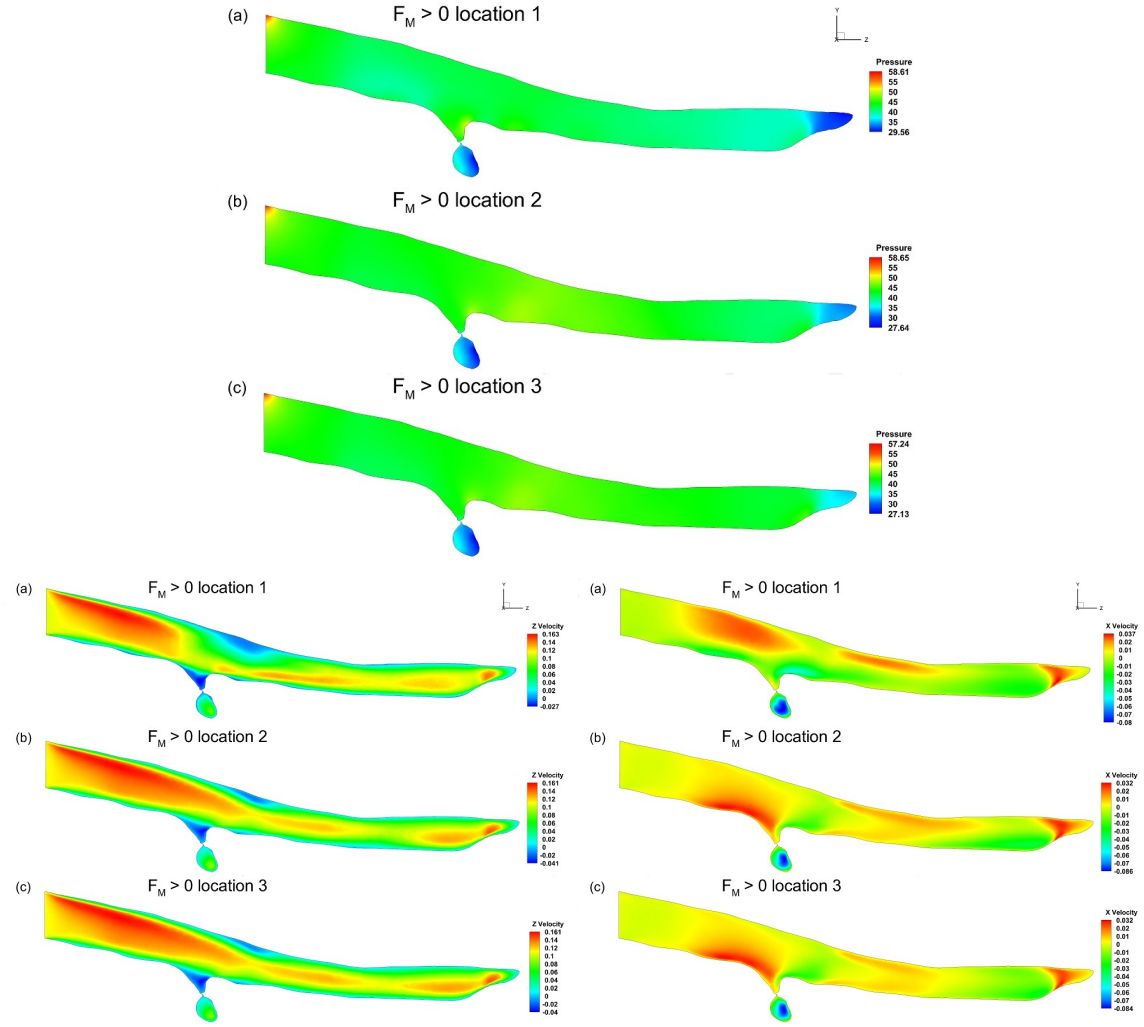

Figure 4.40: Comparisons between the effect of magnetic field on the non-Newtonian blood flow at three different locations for pressure (top) z-velocity (bottom left) and x-velocity (bottom right) contours on yz-plane at x = 0.19 m.

More pronounced perturbations arise for velocity components: Figure 4.40 on page 98 left, highlights how the field at location 1 alters the flow: z-velocity decreases significantly approaching the zone where the magnetic field acts, and the upper slightly recirculating region enhances; the flow turns out to be deflected downstream.
The magnetization force at location 2 has got less effect on the z-velocity, but still slows down the flow. Finally, the field located at the bifurcation (location 3) does not influence the velocity components as the magnetization at location 1 does. The same trend, highlighted for the z-component can be pointed out also for the x-component, where magnetic field at location 1 highly deflects the flow changing pattern and direction, whereas, at the other two locations the effect is weaker.

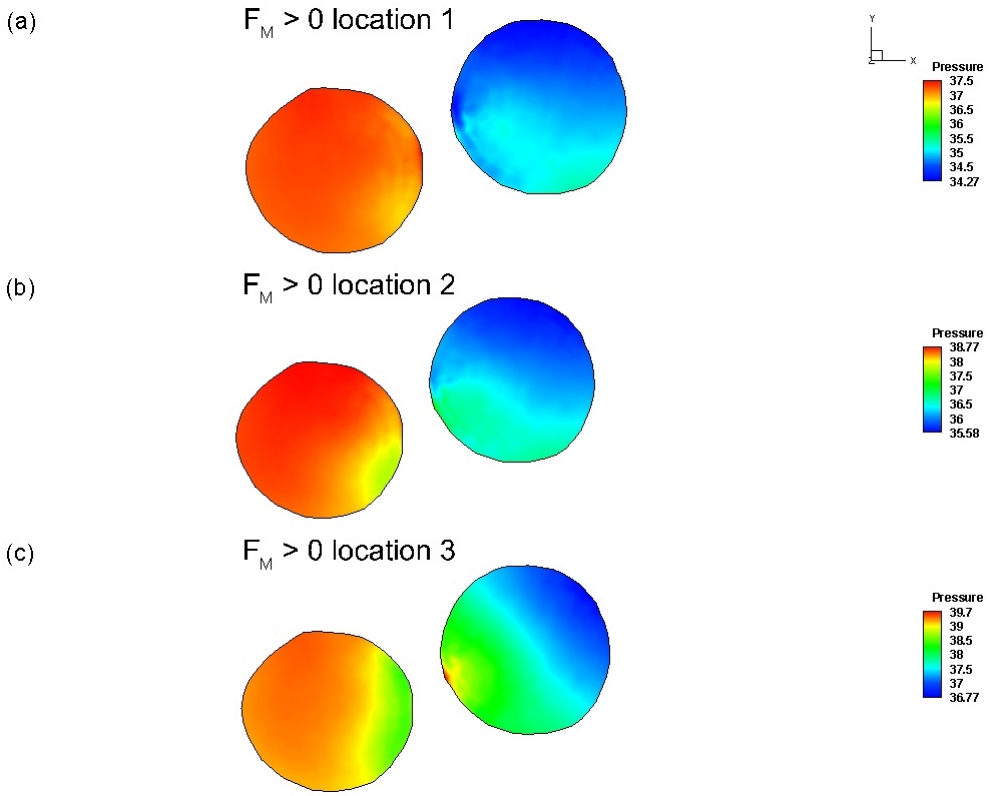

Figure 4.41: Comparisons between the effect of magnetic field on the non-Newtonian blood flow at three different locations for pressure on xy-plane at z = 0.24 m.

If the magnetic field at location 3 does not affect the flow upstream, it strongly perturbs the flow when the Aorta bifurcates, as Figure 4.41 on page 99 shows: the flow is massively pushed on the right side by the magnetization force. From the pressure contours, it can be pointed out that it is also strongly slowed down.

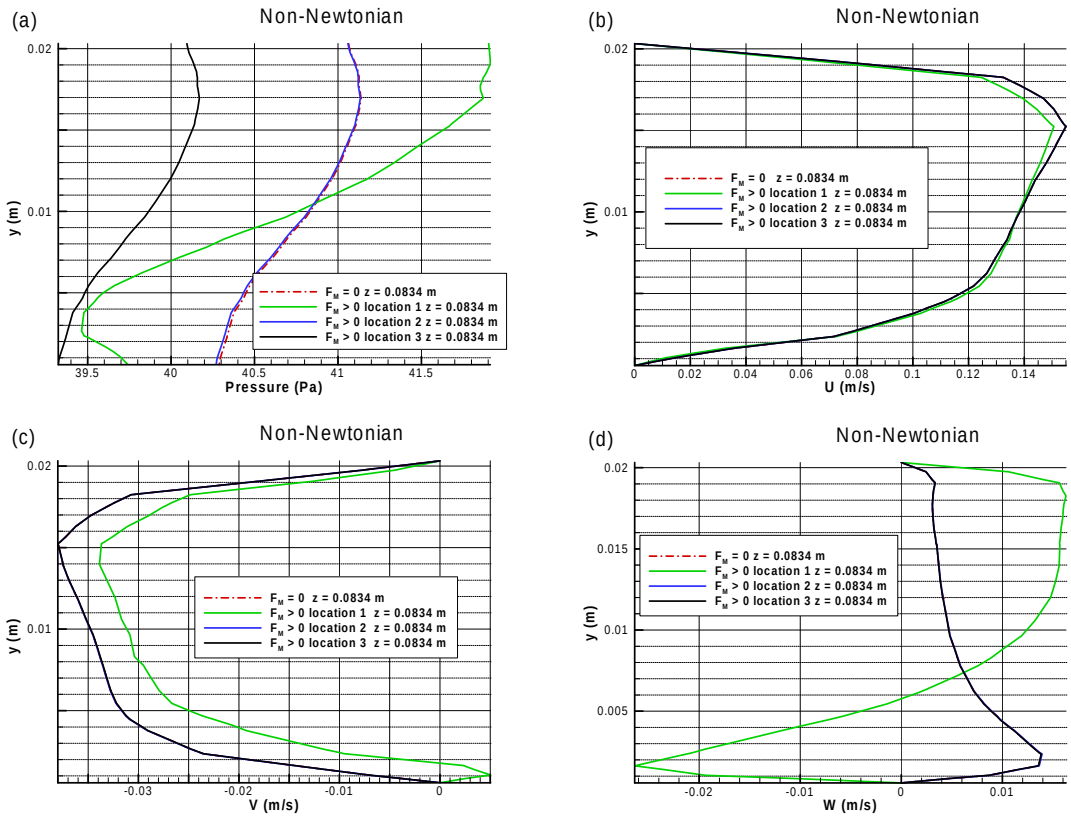

Figure 4.42: Comparisons between the magnetic field location effects on the pressure (a), z-velocity (b), y-velocity (c) and x-velocity (d) at z = 0.0834 m from the inlet and x = 0.19 m from the origin.

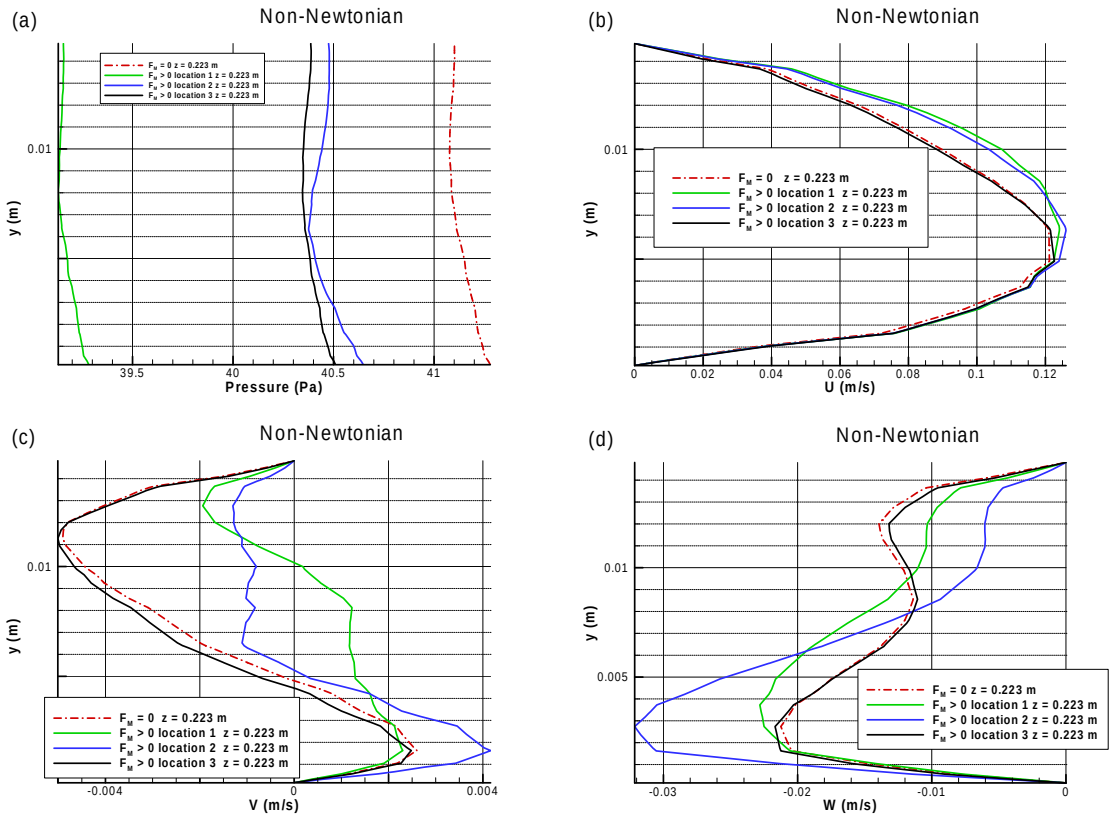

Figure 4.43: Comparisons between the magnetic field location effects on the pressure (a), z-velocity (b), y-velocity (c) and x-velocity (d) at z = 0.223 m from the inlet and x = 0.19 m from the origin.

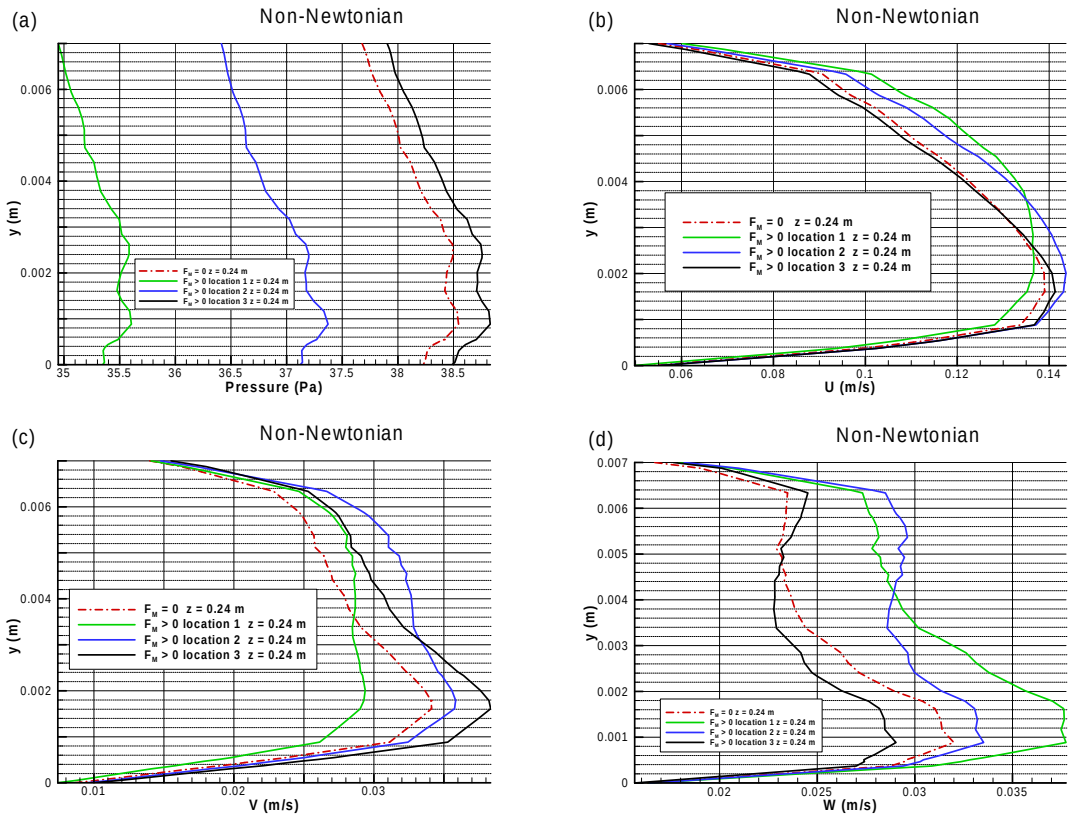

Figure 4.44: Comparisons between the magnetic field location effects on the pressure (a), z-velocity (b), y-velocity (c) and x-velocity (d) at z = 0.24 m from the inlet and x = 0.19 m from the origin.

What has been previously highlighted with the contour plots, can be further detailed through Figure 4.42 on page 100, Figure 4.43 on page 101 and Figure 4.44 on page 102, where profiles at different sections are considered. Interestingly, the pressure betrays the magnetic field influence, acting at location 3, even further upstream. In addition, similarly to what has been discussed earlier, should be stressed that, after the magnetic field has slowed down the flow and the effect is over and flow gains speed, the profile remains permanently changed and the unperturbed condition is not recovered. Should be also noticed that the magnetic field effects are weaker on the z-velocity component than on the y- and x-components due to the fact that the last two are smaller in magnitude than the first one, thus the perturbations are more evident.

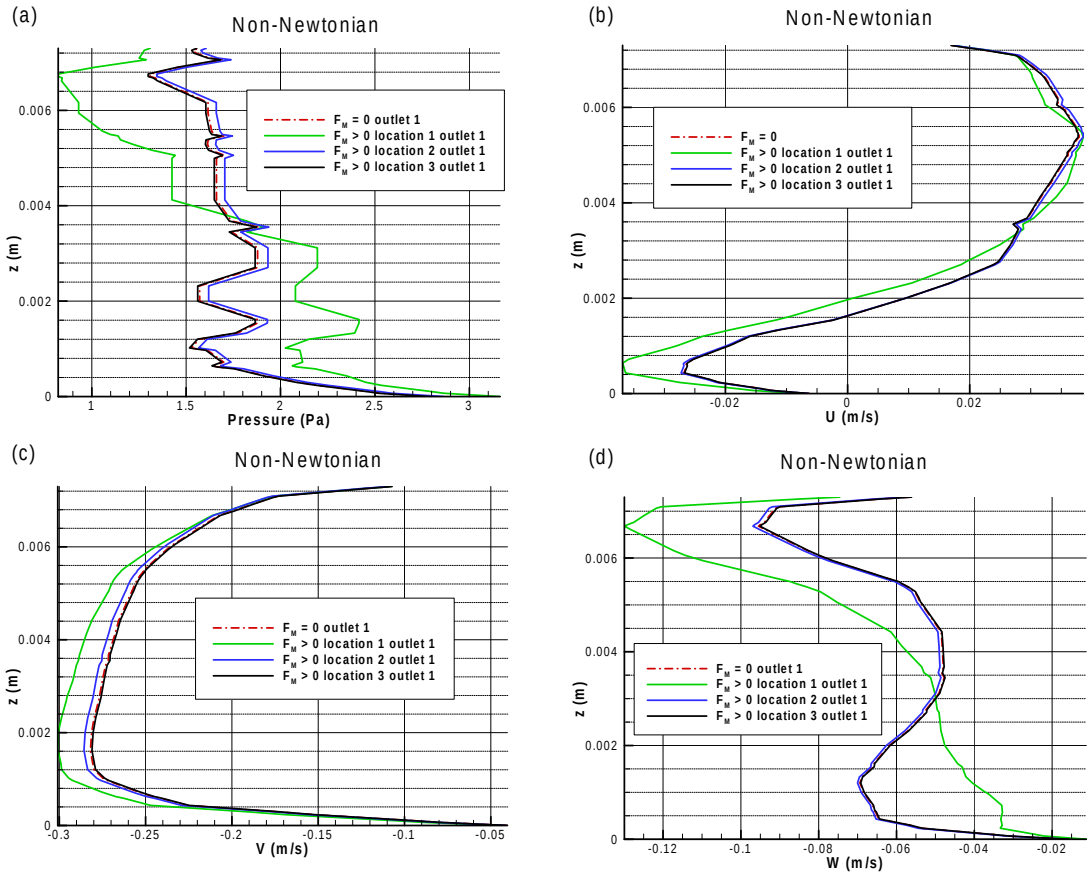

Figure 4.45: Comparisons between the magnetic field location effects on the pressure (a), z-velocity (b), y-velocity (c) and x-velocity (d) at the outlet 1.

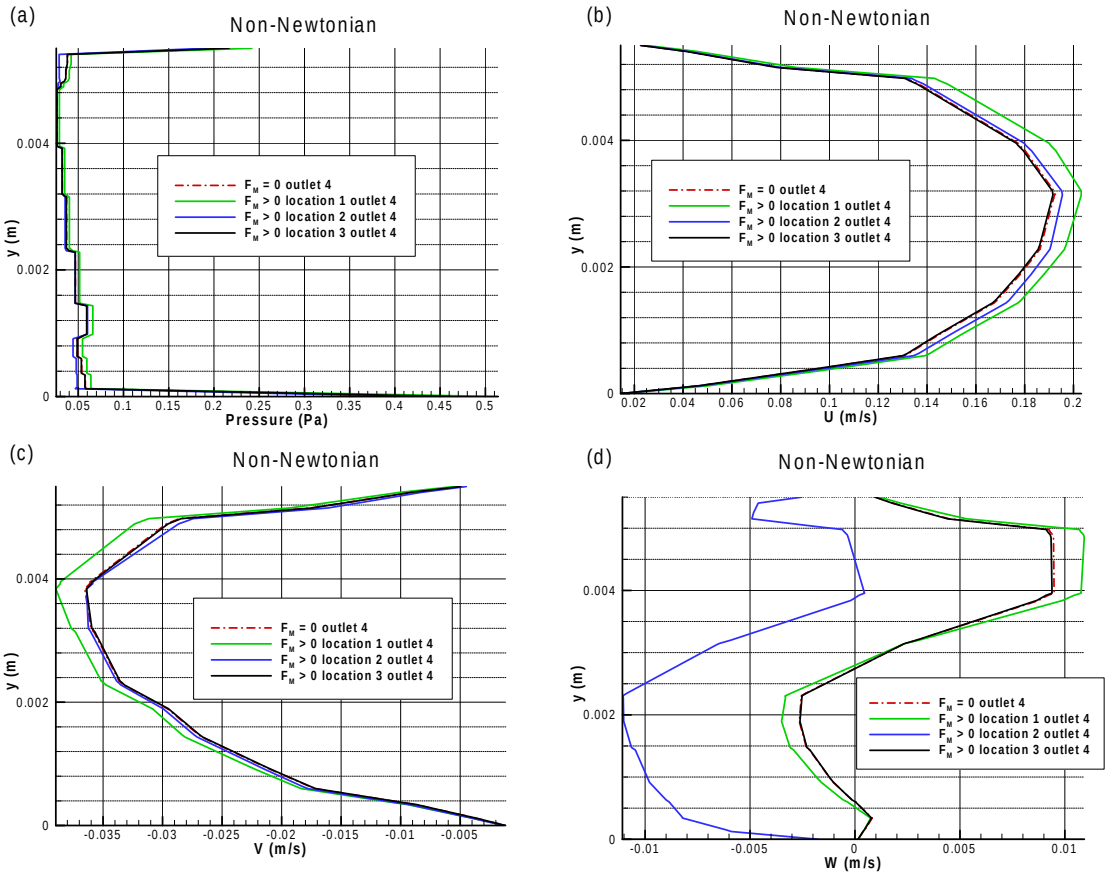

Figure 4.46: Comparisons between the magnetic field location effects on the pressure (a), z-velocity (b), y-velocity (c) and x-velocity (d) at the outlet 4.

The influence of the magnetic field location can be appreciated also from Figure 4.45 on page 103 and Figure 4.46 on page 104: the flow that passes through outlet 1 is clearly disrupted by the presence of the magnetic force, which slows down the fluid and consequently enhances the reversed flow zones, as it possible to observed. Again, when the magnetic field effect fades away, the flow speeds up, and at outlet 4 the magnetization effects placed in location 1 are weaker, while the ones generated by location 2 start to act, especially on the x-velocity component which is smaller in magnitude than the others (Figure 4.46 on page 104 b).

In conclusion, some final remarks can be drown from these results:

- It has been proven that the non-Newtonian rheology of blood affects the flow behaviour and differences can be found if compared with the Newtonian one, especially when the blood flows slowly; therefore, this difference should be taken into account when realistic blood flows are modelled;
- Secondly, it has been turned out that a localised rotational magnetic field considerably influences the blood flow: as it has been found for the 3-D stenosed tube, the flow is deflected and slowed down in proximity the magnetic location. Downstream, the effect becomes weaker, the flow recovers speed, but remains altered. Slower the flow stronger the magnetic field effect is. Additionally, the perturbations, which are highly three-dimensional, propagate even in the secondary branches but with less intensity.

Similar considerations to the ones outlined for the stenosis, on the worthiness of the magnetic field, can be made also for the real Aorta case. A coagulation problem could arise near the magnetized location due to the flow slowing down; the pressure increase has also to be monitored. However, differently from the stenosis case, large recirculation regions have not been generated in this branch of Aorta: this can both avoid formations of blocks but also can make more difficult the drug particle treatment processes: the particle residence time is, indeed, shorter than within a recirculation region, thus, the drug effect could be weaker.

Chapter 5

Conclusions

This thesis project has been focused on numerically studying a novel multi-physic problem, considering the effects of the magnetic field on both the Newtonian and the non-Newtonian blood flow within different domains. The ANSYS FLUENT commercial solver has been used to perform all the simulations, in conjunction with User-Defined Functions that have been coded in order to include the effects of magnetic field and to model the MHD-FHD governing equations.
The UDFs behaviour has been validated comparing the results with the ones found in [1]: it has been found that the FLUENT is able to interpret satisfactorily the additional MHD-FHD source terms and to provide results close to what has been obtained numerically by Tzirakis et al., both for an irrotational and a rotational magnetic field. However, some discrepancies has been found for the rotational case. Nevertheless, the UDFs effectiveness has been proven. The effects of the slip boundary conditions have been also tested, however, results appeared to be strange and not fully trustable, therefore, the slip conditions has been neglected for the other simulations.
In a second stage, using the same geometry of [1], a 3-D cylindrical tube with a 60% in diameter stenosis, the blood physics has been enhanced introducing and studying the non-Newtonian Power-Law model, which has been found to give different results from the Newtonian one at the same flow regime of Re=100; the walls has also been modelled with realistic human vessel properties.. The flow is accelerated due to the different free-stream velocity obtained form the P-L Reynolds number.
The effect of rotational magnetic field has been investigated also for this case, finding out that it definitely breaks down the flow symmetry and enhances the upper recirculation region originating also a stagnation point. The flow behaviour can have both a positive and a negative effect: the negative regards the possibility of coagulation and intolerable wall shear stresses and pressure due to the stream deflection and recirculation. On the other hand, if wisely controlled, it can be effective for drug particle targeting and treatments:

particles can act for longer if injected within the circulatory regions.
Final simulations have been performed on a real Aorta model in order to simulate a scenario with high level of reality and test the solver in realistic scenario. In an early stage, the grid convergence has been studied for the Aorta model reconstructed from MRI sequence of images. Secondly, the differences between the Newtonian and the non-Newtonian Power-Law model have been investigated, assessing that the rheology of blood affects the flow behaviour. This effect is more pronounced when the fluid is slow.
Finally, the rotational magnetic field effects have been tested, applying a 4 Tesla localised rotational magnetic field systematically at three different locations: the flow turned out to be strongly influenced by the magnetic force, which deflects it and slows it down. Magnetization acts both upstream and downstream the application region and, while the effects weaken quickly for the U-velocity, they remain even further downstream in the pressure field and in the other velocity components.
Similar conclusions to the stenosis ones, can be drown also for the Aorta, however the more realistic model allows to better understand how the flow behaves in a realistic scenario, where the symmetry is not present.

In conclusion, from a physical point of view:

- Viscosity models have a remarkable impact on this kind of flows; thus they should be properly studied;
- A simplified model (3-D straight tube with a stenosis) can provide interesting results, but it neglects some important features, such as the several outlet effects, duct narrowing and absence of large reversed flow regions, only visible in a more realistic model;
- The localised magnetic field has turned out to be a powerful tool to influence the blood flow: it can be used for slowing down the flow, enhancing reversed flow regions in order to increase the residence time for drug particles , increasing the pressure or changing the viscosity; however it could be also harmful if not properly located or set-up.

5.1 Future Works

Despite the both physically and numerically interesting results, that have been obtained, some recommendations should be made.
First of all, despite the validation procedure has been conducted in the most meticulous and robust way possible, however, results used for the comparisons are only numerical, therefore, in order to fully trust the outcomes, a comparison with experiments is needed. Secondly, the effect of the wall slip boundary condition should be further studied, considering a less approximate model: it is important to investigate and understand its effects in order to properly simulate the flow within very narrow capillaries,which should be the next step. As previously indicated for the the UDF validation, experimental results should be used also to assess the Aorta model grid convergence, which should be studied deeper anyway. Moreover, unsteady simulations should be performed in order to take into account the pulsate nature of the blood flow.
Finally, although ANSYS FLUENT has been able to perform all the simulations quite satisfactorily, providing also a high order of convergence (1e-9 for the stenosis and 1e-5 for the Aorta), form this work, the solver turned out to be poorly flexible and, despite the UDFs have been created to enhance its capabilities, they never fit and integrate perfectly to the main solver. Therefore, for these multi-physic problems an in-house code, should be programmed, so more features can be implemented and the equations can be solved in a more efficient, correct and complete way; additionally, all the parts can be accessible and an optimizing process can be performed.

Bibliography

[1] K. Tzirakis, Y. Papaharilaou, D. Giordano, and J. Ekaterinaris. Numerical investigation of biomagnetic fluids in circular ducts. *International Journal for Numerical Methods in Biomedical Engineering*, 30(3):297–317, 2013.

[2] R.P. Chhabra. Non-newtonian fluids: An introduction. *Department of Chemical Engineering, Indian Institute of Technology Kanpur*, pages 1–33.

[3] C. Rinaldi, A. Chaves, S. Elborai, X. He, and M. Zahn. Magnetic fluid rheology and flows. *Current Opinion in Colloid & Interface Science*, 10(3-4):141–157, 2005.

[4] S. Kenjeres and D. Cohen C. Stuart. Computational simulations of magnetic particle capture in simplified and realistic arterial flows: Towards optimized magnetic drug targeting. *World Congress on Medical Physics and Biomedical Engineering, September 7 - 12, 2009, Munich, Germany*, 01 2010.

[5] M. G. Giridharan, Soumya Krishnamoorthy, and Anantha Krishnan. Computational simulation of microfluidics, electrokinetics, and particle transport in biological mems devices. *Design, Test, and Microfabrication of MEMS and MOEMS*, 1999.

[6] R. Shetty A. Puri. 3d modeling of flows in intracranical bifurcating arteries with saccular aneurysms. *BME*, (598):1–18, 2012.

[7] Dorothea I. Hollnagel, Paul E. Summers, Dimos Poulikakos, and Spyros S. Kollias. *NMR in Biomedicine*, (8):795–808.

[8] J. Peiro B. Sanghera Y. Papaharilaou, S. J. Sherwin. combined mr imaging and numerical simulation of flow in realistic arterial bypass graft models. *Article in Biorheology*, (39):525–531, 2002.

[9] K. Madlener, B. Frey, and H. K. Ciezki. Generalized reynolds number for non-newtonian fluids. *Progress in Propulsion Physics*, 2009.

[10] C. Fetecau. Analytical solutions for non-newtonian fluid flows in pipe-like domains. *International Juournal of Non-Linear Mechanics*, 39:225–231, 2002.

[11] F. T. Pinho and P. M. Coelho. Non-newtonian heat transfer. *Rheology, UNESCO-EOLSS*, 2010.

[12] Anuj Kumar, Amit Dhiman, and László Baranyi. Cfd analysis of power-law fluid flow and heat transfer around a confined semi-circular cylinder. *International Journal of Heat and Mass Transfer*, 82:159–169, 2015.

[13] E.E. Tzirtzilakis, V.D. Sakalis, N.G. Kafoussias, and P.M. Hatzikonstantinou. Biomagnetic fluid flow in a 3d rectangular duct. *International Journal for Numerical Methods in Fluids*, 44(12):1279–1298, 2004.

[14] V.C. Loukopoulos and E.E. Tzirtzilakis. Biomagnetic channel flow in spatially varying magnetic field. *International Journal of Engineering Science*, 42(5-6):571–590, 2004.

[15] E. E. Tzirtzilakis and V. C. Loukopoulos. Biofluid flow in a channel under the action of a uniform localized magnetic field. *Computational Mechanics*, 36(5):360–374, 10 2005.

[16] E.E. Tzirtzilakis, M. Xenos, V.C. Loukopoulos, and N.G. Kafoussias. Turbulent biomagnetic fluid flow in a rectangular channel under the action of a localized magnetic field. *International Journal of Engineering Science*, 44(18-19):1205–1224, 2006.

[17] G. C. Shit, M. Roy, and A. Sinha. Mathematical modelling of blood flow through a tapered overlapping stenosed artery with variable viscosity. *Applied Bionics and Biomechanics*, 11(4):185–195, 2014.

[18] Dinesh Kumar Verma, B V Ratish Kumar, and Prawal Sinha. Generalized reynolds equation for non-newtonian ferrofluids. *Indian Journal of Engineering I& Materials Sciences*, 10:41–49, 2003.

[19] Hazem A. Attia. Unsteady mhd flow of a dusty non-newtonian bingham fluid through a circular pipe. *Journal of the Brazilian Society of Mechanical Sciences and Engineering*, 28, 2006.

[20] J.C. Misra, G.C. Shit, and H.J. Rath. Flow and heat transfer of a mhd viscoelastic fluid in a channel with stretching walls: Some applications to haemodynamics. *Computers & Fluids*, 37(1):1–11, 2008.

[21] Erica M. Cherry and John K. Eaton. Simulation of magnetic particles in the bloodstream for magnetic drug targeting applications, 05 2013.

[22] Takuji Ishikawa, Luis F R Guimaraes, Shuzo Oshima, and Ryuichiro Yamane. Effect of non-newtonian property of blood on flow through a stenosed tube. *Fluid Dynamics Research*, 22(5):251–264, 1998.

[23] Nicole Pamme. Magnetism and microfluidics. *Lab Chip*, 6(1):24–38, 2006.

[24] H. Ben Hadid, D. Henry, and S. Kaddeche. Numerical study of convection in the horizontal bridgman configuration under the action of a constant magnetic field. part 1. two-dimensional flow. *Journal of Fluid Mechanics*, 333:23–56, 1997.

[25] Noreen Sher Akbar, Abdelhalim Ebaid, and Z.H. Khan. Numerical analysis of magnetic field effects on eyring-powell fluid flow towards a stretching sheet. *Journal of Magnetism and Magnetic Materials*, 382:355–358, 2015.

[26] Satish Kandlikar, Michael R. King, Dongqing Li, Stephane Colin, and Srinivas Garimella. *Heat Transfer and Fluid Flow in Minichannels and Microchannels*. Elsevier Science, Amsterdam, Netherlands, 10 2005.

[27] Prashanta Kumar Mandal. An unsteady analysis of non-newtonian blood flow through tapered arteries with a stenosis. *International Journal of Non-Linear Mechanics*, 40(1):151–164, 2005.

[28] R. Ponalagusamy. Blood flow through an artery with mild stenosis: A two-layered model, different shapes of stenoses and slip velocity at the wall. *Journal of Applied Sciences*, 7(7):1071–1077, 2007.

[29] Tiegang Fang, Ji Zhang, and Shanshan Yao. Slip mhd viscous flow over a stretching sheet; an exact solution. *Communications in Nonlinear Science and Numerical Simulation*, 14:3731–3737, 01 2011.

[30] Narendra Kumar Verma, Shailesh Mishra, Shafi Ullah Siddiqui, and Ram Saran Gupta. Effect of slip velocity on blood flow through a catheterized artery. *Applied Mathematics*, 02(06):764–770, 2011.

[31] R.E. Rosenweig. An introduction to ferrohidrodynamics. *Chemical Engineering Communications*, 67(1):1–18, 1988.

[32] Mark I. Shliomis. Ferrohydrodynamics: Retrospective and issues. *Lecture Notes in Physics*, pages 85–111, 2002.

[33] László Könözsy. *Multiphysics CFD Modelling of Incompressible Flow at Low and Moderate Reynolds Numbers*. PhD thesis, Cranfield University, 2012.

[34] F.J. Walburn and D.J. Schneck. A constitutive equation for whole human blood. *Biorheology*, (13):201–210, 1976.

[35] D. Quemada. Rheology of concentrated disperse systems iii. general features of the proposed non-newtonian model. comparison with experimental data. *Rheologica Acta*, 17(6):643–653, 1978.

[36] N.A. Casson. A flow equation for pigment-oil suspensions of the printing ink type. *Rheology of Disperse Systems*, pages 84–102, 1959.

[37] Inc. ANSYS. *ANSYS FLUENT 12.0 UDF Manual*. ANSYS, Inc., 2009.

[38] ITIS Foundation. ITIS Foundation tissue properties database, 2010.

Appendix A

The non-Newtonian Power-Law viscous terms

Within this Appendix equations for non-Newtonian viscous terms are detailed.
As mentioned in 3.1.4, the Power-Law shear thinning model can be expressed as:

$$\tau = k_0 \dot{\gamma}^n, \tag{A.1}$$

with n < 1.
The viscous terms that appear within the Navier-Stokes momentum equations:

$$\nabla \cdot \underset{=}{\tau}, \tag{A.2}$$

For the non-Newtonian Power-Law model assume the following form:

$$\nabla \cdot \underset{=}{\tau} = \nabla \cdot \left(k_0 \left| \underset{=}{\dot{\gamma}} \right|^{n-1} \left| \underset{=}{\dot{\gamma}} \right| \right), \tag{A.3}$$

The shear strain rate $\underset{=}{\dot{\gamma}}$ can be computed as:

$$\underset{=}{\dot{\gamma}} = \mathbf{u} \otimes \nabla + \nabla \otimes \mathbf{u} = \begin{bmatrix} 2\frac{\partial u}{\partial x} & \left(\frac{\partial u}{\partial y} + \frac{\partial v}{\partial x}\right) & \left(\frac{\partial u}{\partial z} + \frac{\partial w}{\partial x}\right) \\ \left(\frac{\partial v}{\partial x} + \frac{\partial u}{\partial y}\right) & 2\frac{\partial v}{\partial y} & \left(\frac{\partial w}{\partial y} + \frac{\partial v}{\partial z}\right) \\ \left(\frac{\partial w}{\partial x} + \frac{\partial u}{\partial z}\right) & \left(\frac{\partial v}{\partial z} + \frac{\partial w}{\partial y}\right) & 2\frac{\partial w}{\partial z} \end{bmatrix}, \tag{A.4}$$

A. The non-Newtonian Power-Law viscous terms

In order to simplify and make the derivation shorter the 2-D case is considered:

$$\underset{=}{\dot{\gamma}} = \begin{bmatrix} 2\frac{\partial u}{\partial x} & \left(\frac{\partial u}{\partial y} + \frac{\partial v}{\partial x}\right) \\ \left(\frac{\partial v}{\partial x} + \frac{\partial u}{\partial y}\right) & 2\frac{\partial v}{\partial y} \end{bmatrix}, \tag{A.5}$$

The Cartesian shear stress components for the 2-D case can then be derived:

$$\tau_{xx} = 2k_0 \left|\underset{=}{\dot{\gamma}}\right|^{n-1} \frac{\partial u}{\partial x}, \tag{A.6}$$

$$\tau_{xy} = \tau_{yx} = k_0 \left|\underset{=}{\dot{\gamma}}\right|^{n-1} \left(\frac{\partial u}{\partial y} + \frac{\partial v}{\partial x}\right), \tag{A.7}$$

$$\tau_{yy} = 2k_0 \left|\underset{=}{\dot{\gamma}}\right|^{n-1} \frac{\partial v}{\partial y}, \tag{A.8}$$

At this point $\left|\underset{=}{\dot{\gamma}}\right|^{n-1}$ should be expanded. Knowing that:

$$\left|\underset{=}{\dot{\gamma}}\right| = \left(\sqrt{\frac{1}{2}\underset{==}{\dot{\gamma}}\underset{==}{\dot{\gamma}}}\right), \tag{A.9}$$

Then:

$$\begin{aligned} \left|\underset{=}{\dot{\gamma}}\right|^{n-1} = \left(\sqrt{\frac{1}{2}\underset{==}{\dot{\gamma}}\underset{==}{\dot{\gamma}}}\right)^{n-1} &= \left(\sqrt{2\left(\frac{\partial u}{\partial x}\right)^2 + 2\left(\frac{\partial v}{\partial y}\right)^2 + 2\left(\frac{\partial u}{\partial y} + \frac{\partial v}{\partial x}\right)^2}\right)^{n-1} \\ &= \left[2\left(\frac{\partial u}{\partial x}\right)^2 + 2\left(\frac{\partial v}{\partial y}\right)^2 + 2\left(\frac{\partial u}{\partial y} + \frac{\partial v}{\partial x}\right)^2\right]^{\frac{n-1}{2}}, \end{aligned} \tag{A.10}$$

Finally, the shear stress components can be recovered:

$$\tau_{xx} = 2k_0 \left[2\left(\frac{\partial u}{\partial x}\right)^2 + 2\left(\frac{\partial v}{\partial y}\right)^2 + 2\left(\frac{\partial u}{\partial y} + \frac{\partial v}{\partial x}\right)^2 \right]^{\frac{n-1}{2}} \frac{\partial u}{\partial x}, \tag{A.11}$$

$$\tau_{xy} = \tau_{yx} = k_0 \left[2\left(\frac{\partial u}{\partial x}\right)^2 + 2\left(\frac{\partial v}{\partial y}\right)^2 + 2\left(\frac{\partial u}{\partial y} + \frac{\partial v}{\partial x}\right)^2 \right]^{\frac{n-1}{2}} \left(\frac{\partial u}{\partial y} + \frac{\partial v}{\partial x}\right), \tag{A.12}$$

$$\tau_{yy} = 2k_0 \left[2\left(\frac{\partial u}{\partial x}\right)^2 + 2\left(\frac{\partial v}{\partial y}\right)^2 + 2\left(\frac{\partial u}{\partial y} + \frac{\partial v}{\partial x}\right)^2 \right]^{\frac{n-1}{2}} \frac{\partial v}{\partial y}. \tag{A.13}$$

The strong non-linearity of the non-Newtonian viscous terms are then clearly highlighted.